AFOSR-TR- 83-0144

MSU/SWT TR 82-05

AFOSR TR NO. _____

AD-A126 458

# EXPERIMENTAL STUDY OF TRANSITION IN A COMPRESSIBLE FREE SHEAR LAYER

Prepared by

Anthony Demetriades and Timothy L. Brower
Supersonic Wind-Tunnel Laboratory
Mechanical Engineering Department
Montana State University
Bozeman, Montana 59717

Prepared for

Air Force Office of Scientific Research
Building 410, Bolling AFB
Washington, D.C. 20332

AFOSR
Under AFOSR Grant No. 80-0267

December 1982

AIR FORCE OFFICE OF SCIENTIFIC RESEARCH (AFSC)
NOTICE OF TRANSMITTAL TO DTIC
This technical report has been reviewed and is
approved for public release IAW AFR 190-12.
Distribution is unlimited.
MATTHEW J. KERPER
Chief, Technical Information Division

Approved for public release;
distribution unlimited.

UNCLASSIFIED

ECURITY CLASSIFICATION OF THIS PAGE *(When Data Entered)*

| REPORT DOCUMENTATION PAGE | | READ INSTRUCTIONS BEFORE COMPLETING FORM |
|---|---|---|
| 1. REPORT NUMBER<br>AFOSR-TR- 83-0144 | 2. GOVT ACCESSION NO.<br>AD-A126458 | 3. RECIPIENT'S CATALOG NUMBER |
| 4. TITLE *(and Subtitle)*<br>EXPERIMENTAL STUDY OF TRANSITION IN A COMPRESSIBLE FREE SHEAR LAYER | | 5. TYPE OF REPORT & PERIOD COVERED<br>ANNUAL<br>1 Oct 81 - 30 Sep 82 |
| | | 6. PERFORMING ORG. REPORT NUMBER |
| 7. AUTHOR(s)<br>A DEMETRIADES<br>T L BROWNER | | 8. CONTRACT OR GRANT NUMBER(s)<br>AFOSR-80-0267 |
| 9. PERFORMING ORGANIZATION NAME AND ADDRESS<br>MONTANA STATE UNIVERSITY<br>DEPT OF MECHANICAL ENGINEERING<br>BOZEMAN, MT 59717 | | 10. PROGRAM ELEMENT, PROJECT, TASK AREA & WORK UNIT NUMBERS<br>61102F<br>2307/A2 |
| 11. CONTROLLING OFFICE NAME AND ADDRESS<br>AIR FORCE OFFICE OF SCIENTIFIC RESEARCH/NA<br>BOLLING AFB, DC 20332 | | 12. REPORT DATE<br>December 1982 |
| | | 13. NUMBER OF PAGES<br>95 |
| 14. MONITORING AGENCY NAME & ADDRESS*(if different from Controlling Office)* | | 15. SECURITY CLASS. *(of this report)*<br>Unclassified |
| | | 15a. DECLASSIFICATION/DOWNGRADING SCHEDULE |

16. DISTRIBUTION STATEMENT *(of this Report)*

Approved for Public Release; Distribution Unlimited.

17. DISTRIBUTION STATEMENT *(of the abstract entered in Block 20, if different from Report)*

18. SUPPLEMENTARY NOTES

19. KEY WORDS *(Continue on reverse side if necessary and identify by block number)*

LASER
LAMINAR
SUPERSONIC
MIXING
SHEAR LAYER
TRANSITION

20. ABSTRACT *(Continue on reverse side if necessary and identify by block number)*

The object of this work is the experimental determination of laminar-turbulent transition in shear layers separating adjacent compressible streams. An earlier theoretical determination of transition, based on a minimum Reynolds number condition, is reviewed as a possible asymptotic transition limit when the flow is either an equilibrium shear layer or an equilibrium wake. A theory for the laminar flow development in the non-equilibrium regime downstream of the trailing edge is also presented for the first time, and is found to agree very

DD FORM 1 JAN 73 1473 EDITION OF 1 NOV 65 IS OBSOLETE

UNCLASSIFIED

SECURITY CLASSIFICATION OF THIS PAGE *(When Data Entered)*

well with numerical methods. The transition and laminar flow theories are then joined to design an experiment aimed at producing non-equilibrium flows in a supersonic wind-tunnel, and at detecting the transition zone in such a flow. Flow and transition measurements done in this layer show that the shear-layer transition Reynolds number, based on the layer thickness and the fast-side unit Reynolds number, agrees with the corresponding number found by the equilibrium transition theory within 25%. It is concluded that the asymptotic transition theory utilized gives reasonable estimates even close to the trailing edge.

| Accession For | |
|---|---|
| NTIS GRA&I | X |
| DTIC TAB | ☐ |
| Unannounced | ☐ |
| Justification | |
| By | |
| Distribution/ | |
| Availability Codes | |
| Dist | Avail and/or Special |
| A | |

DTIC COPY INSPECTED 3

AFOSR-TR- 83-0144

MSU/SWT TR 82-05

AFOSR TR NO. _____

# EXPERIMENTAL STUDY OF TRANSITION IN A COMPRESSIBLE FREE SHEAR LAYER

Prepared by

Anthony Demetriades and Timothy L. Brower
Supersonic Wind-Tunnel Laboratory
Mechanical Engineering Department
Montana State University
Bozeman, Montana 59717

Prepared for

Air Force Office of Scientific Research
Building 410, Bolling AFB
Washington, D.C. 20332

AFOSR
Under AFOSR Grant No. 80-0267

December 1982

AIR FORCE [illegible] SCIENTIFIC RESEARCH (AFSC)
NOTICE [illegible]
This [illegible] and is
ap[illegible] 190-12.
D[illegible]
MA[illegible]
Chief, Technical Information Division

Approved for public release;
distribution unlimited.

## ABSTRACT

The object of this work is the experimental determination of laminar-turbulent transition in shear layers separating adjacent compressible streams. An earlier theoretical determination of transition, based on a minimum Reynolds number condition, is reviewed as a possible asymptotic transition limit when the flow is either an equilibrium shear layer or an equilibrium wake. A theory for the laminar flow development in the non-equilibrium regime downstream of the trailing edge is also presented for the first time, and is found to agree very well with numerical methods. The transition and laminar flow theories are then joined to design an experiment aimed at producing non-equilibrium flows in a supersonic wind-tunnel, and at detecting the transition zone in such a flow. Flow and transition measurements done in this layer show that the shear-layer transition Reynolds number, based on the layer thickness and the fast-side unit Reynolds number, agrees with the corresponding number found by the equilibrium transition theory within 25%. It is concluded that the asymptotic transition theory utilized gives reasonable estimates even close to the trailing edge.

# FOREWORD

This report describes research conducted at Montana State University's Supersonic Wind-Tunnel Laboratory under U.S. Air Force Office of Scientific Research Grant No. 80-0267. The program consisted of a series of experiments done to determine laminar-turbulent transition behavior in a two-dimensional shear layer separating two adjacent supersonic streams, with emphasis in the non-equilibrium zone immediately downstream of the dividing partition. Responsible for this program was A. Demetriades, Professor of Mechanical Engineering. Timothy Brower, graduate student in mechanical engineering, performed most of the design work and carried out most of the measurements.

The authors are indebted to MSU's John Rompel, Gordon Williamson, and Glen McCullough for expert assistance with the laboratory models and equipment, and to Professor Harry Townes for his participation in the nozzle design. Paul J. Ortwerth of USAF/AFWL and Captain Mike Francis of AFOSR provided encouragement throughout this work. Theoretical work contained in the Appendix of this report had its inception during earlier work of the senior author for TETRA Corp. of Albuquerque, New Mexico.

TABLE OF CONTENTS


| | | |
|---|---|---|
| i. | Abstract | i |
| ii. | Foreword | ii |
| iii. | Table of Contents | iii |
| iv. | List of Symbols | v |
| v. | List of Illustrations | viii |
| 1. | Introduction | 1 |
| 2. | Predictive Method for Transition in Shear Flows. | 3 |
| | 2.1 General Description of Method | 3 |
| | 2.2 Application to Wake Flows | 4 |
| | 2.3 Application To Free Shear Layers | 5 |
| | 2.4 Transition in a FSL Shed by a Partition | 7 |
| 3. | The Experiment: Motivation and Design | 10 |
| 4. | Matrix of Experimental Conditions | 13 |
| 5. | Facilities and Equipment | 14 |
| | 5.1 Wind-Tunnel | 14 |
| | 5.2 Modification of the SWT for the Present Measurements | 14 |
| | 5.3 Instrumentation | 17 |
| | 5.3.1 Schlieren Optical System | 17 |
| | 5.3.2 Hot-Film Anemometer | 17 |
| | 5.3.3 Static Pressure Probe | 18 |
| | 5.3.4 Pitot Probe | 18 |
| | 5.3.5 Total Temperature Probe | 19 |
| | 5.3.6 Electromechanical Positioning and Actuating | 19 |
| 6. | Results | 22 |
| | 6.1 Preliminary Results with Modes I and II | 22 |
| | 6.2 Instability and Transition Results for Modes I and II | 24 |
| | 6.3 Results with Mode III | 26 |
| | 6.3.1 General | 26 |
| | 6.3.2 Mode III Nozzle Flow | 27 |
| | 6.3.3 Edge Properties and FSL Thickness | 28 |
| | 6.3.4 Flow Properties Across the Shear Layer | 29 |
| | 6.3.5 Transition to Turbulence | 30 |

TABLE OF CONTENTS

Continued


| | | |
|---|---|---|
| 7. | Discussion of the Transition Observations | 34 |
| 8. | Conclusions | 36 |
| References | | 37 |
| Figures | | 39 |
| Appendix | | 70 |

## LIST OF SYMBOLS

C: Constant in Chapman's FSL expression (see Appendix)

C': Constant in transition Reynolds number (C' ≈ 234)

C": Constant in transition Reynolds number = $C'^2$

$C_D h$: Wake momentum deficit

DSL: Dividing streamline

f: Frequency

FSL: Free shear layer

G: Laminar FSL thickness, eq. (6)

h: FSL thickness

$h_T$: FSL thickness at transition

k: Viscosity-temperature exponent

M: Mach number

P: $\theta_1/\theta_2$

p: pressure

Q: non-dimensional heat transfer rate (wakes)

r: speed ratio $u_1/u_2$

Re: Reynolds number

Re': unit Reynolds number

$Re_x$: Reynolds number based on distance from T.E.

$Re_{xT}$: $Re_x$ at transition

$Re_{hT}$: Reynolds number based on FSL thickness at transition

$Re_\Lambda$: turbulence Reynolds number

$Re_{\Lambda o}$: critical turbulence Reynolds number

$Re_o$: minimum Reynolds number for transition at M = 0

Re': $(Re_1' + Re_2')/2$

$Re_w$: wake Reynolds number

LIST OF SYMBOLS

continued

SWT: Supersonic wind-tunnel

T: temperature

$T_0$: stagnation temperature

T.E.: Trailing edge

u: velocity

u': velocity fluctuation (wideband r.m.s.)

x: distance from T.E. (streamwise)

x*: same as x (Appendix)

x': non-dimensional x* (Appendix)

$x_T$: x at transition

$\bar{x}_T$: non-dimensional $x_T$

y: distance normal to the FSL

y*: same as y (Appendix)

$\tilde{y}$*: compressible-transformed y* (Appendix)

y': non-dimensional y (Appendix)

$\alpha$: deflection angle of FSL

$\gamma$: ratio of specific heats

$\Gamma(M_1)$: magnitude of maximum u'

$\delta$: boundary-layer thickness at T.E.

$\eta$: non-dimensional variable (Appendix)

$\theta$: momentum thickness at the T.E.

$\Theta$: $\theta_1 + \theta_2$

$\lambda$: non-dimensional speed ratio $(u_1 - u_2)/(u_1 + u_2)$

$\Lambda$: longitudinal integral scale of u'

$\nu$: kinematic viscosity

LIST OF SYMBOLS

continued

$\rho$: density

$\sigma$: Prandtl number

$( )_o$: stagnation conditions

$( )_e$: properties at FSL edge; nozzle-exit properties

$( )_{TE}$: Trailing-edge properties

$( )\ (0)$: Properties at $y^* = 0$

$( )_1$: Fast-stream properties

$( )_2$: Slow-stream properties

$( )\ D_{SL}$: properties on dividing streamline

LIST OF ILLUSTRATIONS


1. Wake transition distance vs. wake Reynolds number.
2. FSL transition Reynolds number based on FSL thickness.
3. Original conception of FSL width (from Ref. 3).
4. FSL transition Reynolds number based on distance from T.F.
5. Thickness-based transition Re behavior for FSL's shed by partitions.
6. Wake transition Re based on thickness of wake.
7. Transition on FSL's shed from partitions at $M_1 = 3$.
8. Conceptual statement of present problem.
9. Original experiment design using wetted-length Reynolds numbers.
10. Overall view of the wind-tunnel showing major components.
11. SWT modification for parallel-stream mixing.
12. The Mode I configuration
13. The Mode III configuration. Note probe installation.
14. FSL flows obtained with the Mode I, II set-up.
15. Comparison of preliminary FSL data with expectations.
16. Boundary-layer growth in the SWT Mach 3 nozzle.
17. Working diagram for Mode I, II test design.
18. Nomenclature for FSL deflecting due to unmatched $p_o$'s.
19. Working diagram for Mode IIa test design.
20. Wideband signals (typical) for Mode I, II FSL.
21. Power spectra on high-speed side of Mode I, II FSL.
22. Power spectra on low-speed side of Mode I, II FSL.
23. Working diagram for Mode III test design.
24. Continuous (top) and spark (middle and bottom) Schlieren photos of the Mode III flow.

LIST OF ILLUSTRATIONS

continued

25. Hot-film anemometer signals at the T.E. of both nozzles.

26. Velocity distribution in the exit plane of both nozzles.

27. Pressure distribution in the nozzle exit region.

28. Boundary layer thicknesses on either side of the T.E.

29. Momentum thicknesses on either side of the T.E.

30. FSL thickness growth for Mode III experiments.

31. Mach number variations along FSL edges.

32. Pressure (top) and unit Reynolds number (bottom) along the FSL.

33. Velocity variation along the edge of the FSL.

34. Center-plane velocity and temperature changes, Mode III.

35. Typical pressure, pitot and $T_0$ profiles across the Mode III FSL.

36. Velocity profiles across the Mode III FSL.

37. Continuous-exposure Schlieren photos of the FSL.

38. Spark Schlieren photos of the FSL.

39. The Mode III FSL under continuous (top) and spark (bottom) Schlieren photography.

40. Wideband hot-film output in the Mode III FSL.

41. Spectra of the hot-film output in the Mode III FSL.

42. The hot-film output at f = 175 khz across the FSL.

43. Streamwise variation of the hot-film signals.

44. Measured transition point in the Mode III FSL.

## 1. Introduction

It is well known that the mixing of two different but parallel, adjacent streams increases drastically when the shear layer separating them becomes turbulent. In fluid lasers where rapid mixing of flowing chemicals is desired, the prediction of laminar-turbulent transition onset is therefore of great importance. Mathematical approaches leading to such predictions are currently unavailable. Traditional analytic methods center about hydrodynamic stability theory, which however deals with destabilization of flow disturbances rather than with turbulence onset. Furthermore, progress with stability theory can be made only in inverse proportion to the complexities bestowed on the flow by design features such as compressibility, heat transfer etc. A third obstacle to the utility of stability theory is that the shear layer profile is not self-similar in the region of interest because of distortions caused to it by the merging boundary layers.

Apparently, mixing can be accelerated by mechanisms other than turbulence. The observations of Roshko and his co-worker (Reference 1) have motivated researchers at Caltech and elsewhere to seek inhomogeneous mixing models based on vortex structures generated by Kelvin-Helmholtz instabilities. The role of these instabilities, however, is not presently clear when density differences are also generated by compressibility, as is the case of the supersonic mixing flows in laser cavities. While supersonic free shear layer experiments should allow for observation and assessment of such large-scale mixing mechanisms, they should still aim at disposing of the transition question as the latter has been understood in the past.

A theory based on minimum conditions to be satisfied before transition appears in the layer, first proposed by the senior author of this report (Reference 2), has been fairly successful when it was compared with transition data for "equilibrium" free shear layers, i.e. for layers with an asymptotic self-similar profile (Section 2, below). There is no reason, however, to expect this approach to be valid near the trailing edge of the

partition separating the two streams, where the shear layer is in "non-equilibrium" caused by the presence of the boundary-layer "wake". Experiments were thus performed in this non-equilibrium region to provide a link to the asymptotic theory. The description of these measurements is the purpose of this report.

## 2. Predictive Method for Transition in Shear Flows

### 2.1 General Description of the Method

A method for predicting transition to turbulence in free shear layers was proposed by the senior author in 1979 (References 3 and 4). A brief description of the principles behind this method is most important in comprehending the approach, results and conclusions of the present experiments.

Briefly, the method consists of establishing a minimum condition for the maintainance of turbulence in the shear layer, and involves the following steps. First, a parameter is sought whose value in the turbulence must lie above a certain threshold for turbulence to exist; this parameter is the turbulence Reynolds number

$$Re_{\Lambda} = \frac{u'\Lambda}{\nu} \qquad (1)$$

based on the r.m.s. longitudinal velocity fluctuation $u'$, the integral scale $\Lambda$ and the molecular kinematic viscosity $\nu$. Second, it is claimed that if self-preserving turbulence is to follow transition, the quantities $u'$ and $\Lambda$ must scale with characteristic velocities and lengths found in the turbulent zone, such as the velocity defect in a wake or the velocity "jump" in a FSL, and the width of the turbulent zone. Finally, the viscosity is expressed in terms of the static temperature, changing eq. (1) into one containing only mean (time-averaged) flow quantities such as the critical flow width, edge properties, integral properties (e.g. the momentum Reynolds number) and the appropriate empirical constants. For any specific type of flow these constants are known from experiments, so that a set of initial and edge conditions yield a flow width value below which the turbulence cannot sustain itself.

It is seen from the above that the procedure gives, at best, a necessary condition for turbulence onset; no condition of sufficiency exists. Threshold-type transition criteria are not new; for example Liepmann proposed, long ago, an analogous criterion based on turbulent stress thresholds (Reference 5). The attraction of such simple criteria is their simplicity of application, so long as they contain enough of the physics of the transition process and/or

the turbulent state. The physical notion contained in the present method is that viscosity damps the turbulence; in this respect the method is closely related to hydrodynamic stability theory. In fact the proposed threshold of a minimum necessary $Re_\Lambda$ is analogous to the minimum critical $Re_\theta$ of stability theory, which is used successfully to predict transition trends in the presence, for example, of pressure gradients, cooling or mass blowing (Reference 6). One application of the present method which comes to mind immediately, for instance, is the minimum transition distance possible in the presence of artificial disturbances. A catalog of the "classic" flows such as pipes, jets etc. presented by the senior author in Reference 4 shows that the observed effect of geometry, compressibility and heat transfer on these flows matches exactly the predictions of the present method.

## 2.2 Application to Wake Flows

This qualitative coincidence in trends induced this author to see if the condition of necessity was also capable of matching quantitatively the transition observation for various flows. An attempt was first made with two-dimensional wakes. In Reference 7 a search of the experimental literature was made for the appropriate constants, the chief finding being that the minimum possible value of $Re_\Lambda$ was

$$Re_{\Lambda o} = 15 \tag{2}$$

Other pertinent observations were that in the "far" wake $\Lambda \simeq 0.2h$, and that $u'$ scaled with the velocity defect multiplied by appropriate compressibility (density) factors. With these inputs eq. (2) gave

$$\bar{X}_T = \frac{X_T}{C_D h} = \frac{\sigma(\gamma-1)^2\, Me^4 (1+Q)^2\, Re_w}{16\P} \left[ \left( \frac{Re_w}{Re_o} \right)^{\frac{1}{k+1/2}} - 1 \right]^{-2} \tag{3}$$

where $\sigma$ and $\gamma$ are the Prandtl no. and specific heat ratio respectively, Me the edge Mach number, Q the non-dimensional heating or cooling of the wake, $C_D h$ the momentum defect (drag) of the wake and $Re_w$ the Reynolds number based on it, k the temperature-viscosity exponent and $Re_o$ is proportional to $Re_{\Lambda o}$. Comparison of eq. (3) with the available data showed satisfactory agreement (Reference 7). A plot of eq. (3) appears on Figure 1.

Quantitative predictions for pipe flows and boundary layers, although unpublished, had also been made. The transition Reynolds number for pipes was found to be of order of a few thousand, which agrees with observations. For the boundary layer the transition $Re_\theta$ for a smooth flat plate was found to be of order 500 at low speeds and to increase with Me beyond Me = 4, to increase with surface cooling, and to "reverse" for certain combinations of Me and temperature ratio. These trends agree with the concensus of observations (and stability theory predictions) of boundary-layer transition, although quantitatively there is desagreement with a fraction of existing data.

## 2.3 Application to Free Shear Layers

Quantitative estimates of FSL transition were made in References 2, 3 and 4, following the same procedure which led to eq. (3). As before, it was assumed that the velocity fluctuations scale with the velocity jump, and the scale with the FSL width (thickness); and it was also assumed that $\nu$ should be computed on the dividing streamline (DSL). Using subscripts 1 and 2 to denote the "fast" and "slow" sides of the FSL respectively, the following transition Reynolds number based on FSL thickness (rather than distance) was found:

$$Re_{h_T} = \frac{u_1 h_T}{\nu_1} = \frac{C'}{\Gamma(M_1)} \left(\frac{T_{DSL}}{T_1}\right)^{k+1} \frac{\lambda+1}{\lambda} = f\left(M_1, \lambda, \frac{T_{o_2}}{T_{o_1}}\right) \qquad (4)$$

where $\Gamma(M_1)$ expresses the dependence of the fluctuations on $M_1$ and

$$\lambda \equiv \frac{u_1 - u_2}{u_1 + u_2} \qquad (5)$$

The constant $C'$ includes the magnitude of $Re_{\Lambda o}$, the proportionality constant between $\Lambda$ and the FSL thickness $h$, and the corresponding constant connecting $u'$ with $u_1 - u_2$. Since these functional connections are in principle universal for each self-preserving flow, the dependence of $h_T$ on $M_1$, $\lambda$ and $T_{o_2}/T_{o_1}$ can be then found from eq. (4), while its precise numerical value can be updated as more information on the ingredients of $C'$ becomes available ($C' \simeq 230$ according to the current state of knowledge). A plot of eq. (4) appears on Figure 2.

Reference 4 went a step further in re-casting eq. (4) in a way replacing $h_T$ by the "transition distance" $X_T$ from the origin of the laminar FSL. To do this, it was necessary to find a relation between h and X, that is to utilize a formula for the FSL growth as a function of distance from its origin. The growth formula utilized (in Reference 4) is plotted on Figure 3 and was due to Moeny (Reference 3):

$$\frac{h}{x} = G(M_1, \lambda, T_{o_2}/T_{o_1}) \frac{1}{\sqrt{Re_x}} \tag{6}$$

where Re was again based on the fast side properties. Thus eq. (4) gave

$$Re_{xT} = \frac{u_1 X_T}{\nu_1} = C'' \frac{1}{\Gamma^4 G^2} \left(\frac{T_{DSL}}{T_1}\right)^{2(k+1)} \left(\frac{\lambda+1}{\lambda}\right)^2 \tag{7}$$

where C'' is another "universal" constant analogous to C' and simply related to it (Reference 4). If C' = 234, C'' = 54,800. Since all other quantities on the r.h.s. of (7) are only functions of $M_1$, $\lambda$ and $T_{o_2}/T_{o_1}$, the transition distance $X_T$ from the origin of the laminar FSL can be found once these three parameters of the flow are given. Comparison of eq. (7) with data, made in Reference 3, was satisfactory. However, there are important precautions for the use of eq. (7) with trailing-edge flows, which will be explained in Section 2.4. Eq. (7) is plotted on Figure 4.

Before the plans for further verifying eq. (4) or eq. (7), which led to the present experiments, are described, it is necessary to summarize the reservations which a fluid dynamicist should have in using the present theory, and especially equations (4) and (7):

a. The nature of these formulas as estimates of <u>minimum</u> transition Reynolds numbers (or lengths) should be kept in mind, and the lack of a sufficient condition noted.

b. The algebraic forms shown, and the values of C' and C'', presuppose <u>fully</u> developed turbulent flows following transition.

c. The data available for establishing relations between $\Lambda$ and h, $u'$ and $u_e - u(0)$ etc. are extremely meagre.

d. The values of C′ and C′′ are flexible, as noted.

e. No provision is made for lateral variations of $u'$, $\Lambda$ and the fluid temperature across the layer height or width.

f. In predicting transition events or comparing the equations with data, note that transition to turbulence in a shear flow is an event protracted over several, often many, shear layer thicknesses, usually preceded by instabilities and followed by a period of turbulence non-equilibrium. In the present method this zone is contracted to a point.

Within the above reservations equations (3), (4) and (7) represent transition predictions for wakes and free shear layers. In the next section we will argue that the mixing flow downstream of a T.E. is actually a combination of these two flows, and that some combination of the equations will be needed to handle such a geometry.

## 2.4 Transition in a FSL Shed From a Partition

In the preceding we derived formulas for FSL transition according to which, if $M_1$ and $T_{o_2}/T_{o_1}$ are fixed, advance knowledge of the fast-side unit Reynolds number and the speed ratio $\lambda = (u_1-u_2)/(u_1+u_2)$ (or $r = u_2/u_1$) will determine the FSL thickness h at which the flow will become turbulent. Still within the framework of this theory, however, it is clear that this situation cannot persist when $\lambda$ approaches zero, if the FSL is shed from a partition. Here the latter term signifies the non-equilibrium shear layer which carries along the wake component. Specifically, the theory (cf. Figures 2, 3 etc.) indicates that at $\lambda = 0$ the $Re_{hT}$ becomes infinite, as appropriate when the only mechanism for shear production is the usual asymptotic FSL profile. In reality, a finite $Re_{hT}$ limit is reached at $\lambda = 0$ because shear is produced by the wake component.

This limit is illustrated on Figure 5. When $\lambda$ is decreased $u_2$ approaches $u_1$, so that the flow profile changes fundamentally to one of a wake. Thus

at $\lambda = 0$ the profile instability becomes wake instability, and transition guidelines must be drawn from eq. (3) rather than eq. (4). The former equation translates into a straight line at constant $Re_{hT}$ as shown on the Figure, whose position depends on the wake Reynolds number $Re_w$ and which, in turn, depends on $Re_1$ and h; the dependence of $Re_{hT}$ on $Re_w$ is actually quite complex as will be seen shortly. In the meantime the solid line of Figure 5, joining the two limiting cases becomes the complete estimate for transition in the FSL beyond the trailing edge.

To calculate specific applications of Figure 5, one can transform eq. (3) (especially using Reference 7 in conjunction) from the transition distance $X_T$ into a transition Reynolds number $Re_{hT}$:

$$Re_{hT} = (\text{constant})\, M_e^2 \, \frac{Re_w^{1.5}}{\left(\left[\frac{Re_w}{Re_o}\right]^{0.8} - 1\right)} \tag{8}$$

*where*

$$Re_{hT} \equiv \frac{u_1 h_T}{\nu_1} \quad , \quad Re_w = \frac{u_1 C_D h}{\nu_1} \tag{9}$$

as already indicated. The "wake drag" is defined as

$$\begin{aligned} C_D h &= 2 \times (\text{sum of T.E. momentum thicknesses}) \\ &= 2(\theta_1 + \theta_2) = 2\,H \end{aligned} \tag{10}$$

The "wake Reynolds number" $Re_w$ is thus a parameter of the problem while $Re_o = 335$ (Reference 7). The constant appearing in eq. (8) has the value of 0.0912 if in eq. (3) we put $\gamma = 1.4$, $\sigma = 0.85$, $Q = 0$, and $k = 0.75$ for adiabatic air wakes. With these values $Re_{hT}/Me^2$ plots as in Figure 6.

We shall return to this figure momentarily; first we shall observe its consequences on FSL transition. As an example, $Re_{hT}$ vs. $\lambda$ is replotted from Figure 2 on Figure 7 for the case $M_1 = 3$, using $C' = 234$. At $\lambda = 1$, $Re_{hT}$ is about 7500 and decreases as $\lambda$ decreases. When $\lambda$ is very small the FSL profile progressively approaches the wake profile, and the transition Reynolds number thus approaches a finite limit given by eq. (3) or its

equivalent eq. (8) (and Figure 1). This limit depends on $Re_w$, and its lowest possible value is about $2000M_e^2 \approx 18{,}000$ according to Figure 6. For a smaller $Re_w$, say 400, the limit increases to about 45,000. These two examples are drawn in Figure 7 as straight lines parallel to the $\lambda$ axis. Thus at very small $\lambda$ the FSL transition behavior commences at this "wake-controlled limit", and as $\lambda$ increases toward unity the behavior changes to conform to the "FSL-controlled" curve originating in eq. (3). Clearly, these two extremes must be joined smoothly by a path such as shown by dashed lines on Figure 7.

Further insight (and agreement with intuition) comes from further study of Figures 6 and 7. To begin with, since $Re_w = 4Re_{\theta TE}$ (where $Re_{\theta TE}$ is the momentum Reynolds number of the boundary layer at the T.E.) one notes that $Re_w > 2000$ or so on Figure 6 corresponds to $Re_{\theta TE} > 500$. In most laboratory and practical applications this $Re_\theta$ level marks the onset of turbulence in the boundary layer itself. Thus $Re_w > 2000$, approximately, has no corresponding laminar wake flow, and that portion of the curve on Figure 6 is of no physical significance. In the portion $Re_w \lesssim 2000$ one can divide the flow roughly into three categories:

--For $Re_w \lesssim 300$ no turbulent wake flow is possible (Reference 7). Thus no limit to the FSL-controlled transition behavior will appear on Figure 7, at any Me. Here the wake component is so feeble that it has no opportunity to destabilize and trip the flow.

--For intermediate $Re_w$, say $400 < Re_w < 800$, a typical limit is shown on Figure 7. The crossing occurs at $\lambda = 0.02$.

--For large allowed $Re_w$, we say $1000 < Re_w < 2000$, the $Re_{hT}$ attains a minimum depending on Mach number. For Me = 3 Figure 7 shows this minimum (at 18,000) to be still quite larger than the $\lambda = 1$ limit of the FSL-controlled transition curve. The crossing occurs at $\lambda = 0.07$.

The present purpose is to create conditions in the laboratory by which the predictions detailed above, especially those in this section, can be tested. The planning of experiments for this purpose is explained in the next section.

## 3. The Experiments: Motivation and Design

The purpose of the experimental work described here was to detect and correlate laminar-turbulent transition events in the FSL separating two parallel streams issuing from adjacent nozzles. In order to reduce the scope of the program to a manageable size the flows chosen were steady, isothermal and homogeneous; to provide data relevant to fluid laser design the flows were supersonic; and to enable comparison with the transition predictions noted above (and the laminar FSL theory shown in the Appendix) the trailing edge of the partition separating the streams was made sharp.

Despite its shortcomings listed in the previous Section, sufficient resemblance between the few previous available data and the "transition" theory warranted the use of the latter as a design tool for the experiments. Figures 8 and 9, reproduced from the original proposal for this work, can be used to illustrate the following discussion. Figure 8 is a qualitative picture of the events expected to occur when two streams of Mach numbers $M_1$ and $M_2$ ($M_2 < M_1$) are made to flow parallel to each other after issuing from the adjacent nozzles. To simplify the picture it is first assumed that the transition movement in the boundary layer of the top surface of the partition coincides with the corresponding movement of the layer on the bottom surface; thus there exists a unit Reynolds number $Re_1'$ below which the entire flow coming off the T.E. is laminar. Changes in $Re'$ should then affect transition as follows: at very large $Re'$ the nozzle wall boundary layers are turbulent, and as $Re'$ is lowered transition moves downstream along the nozzle surfaces till it reaches the T.E. The particular shape of this variation (curve "A" in Figure 8) is not a problem addressed here, although it should be of interest for applications. Curve "A" can be assumed known for a specific nozzle geometry and flow conditions.

When on the other extreme $Re'$ is very low eq.(7) implies that the FSL remains laminar at far distances downstream of the T.E. In this case the FSL reaches the equilibrium laminar profile discussed in Section 2 and the Appendix; the "memory" of the wake component is lost both in the

pre-transitional laminar and the post-transitional turbulent flow. In this case eq. (7) is supposed to apply and its $Re_i' - X_T$ prediction is shown as curve "C" in Figure 8.

The problem lies in connecting curves A and C. If eq. (7) was valid near the T.E. (ruled as unlikely by the preceding comments) a decrease in $Re_i'$ would cause transition to "jump" from the T.E. to curve C and then follow the latter as $Re_i'$ is further decreased. The invalidity of eq. (7) near the T.E. implies, instead, that a more gradual joining of A and C would occur, hypothesized by curve "B" on Figure 8. The precise track of this curve was the objective of this work.

The path of curve B was of course unknown other than that it should start at the T.E. and asymptotically approach curve C if eq. (7) was valid. The design of the experiment required fixing $M_2$ so that the curve B was most easily detectable. Adopting for the moment the predicted transition distance $X_T$ of eq. (7) as valid, computations were made of the transition occurence in the MSU Supersonic Wind-Tunnel (SWT) taking one stream to be at $M_1 = 3$ and the other at a series of lower Mach numbers $M_2 < M_1$. The results consist of curves in the $Re_i' - X$ plane, each of which separates the turbulent flow above it from laminar flow below it, as shown on Figure 9. The same figure shows observability "window" (or "test aperture") for the FSL, i.e. it sets limits on the upper and lower possible $Re_i'$ (because of $P_0$ limitations) and on the maximum downstream distance X because of the tunnel size.

A serious design difficulty arose in establishing the virtual origin of the laminar FSL, on which $X_T$ of eq. (7) is based. Since no characteristic scale length appears in the formulation of the equilibrium, self-similar FSL this issue was not important in earlier comparisons of the theory with data (cf. Reference 3, Figure 1) because the latter involved mainly FSL's generated by crossing shock waves (References 8 and 9). In planning tests with actual FSL's beginning with finite thickness at some T.E., one can at most assume that the flow began at some fictitious (virtual) origin upstream of the T.E. As a last resort, this unsatisfactory process was used in the design (Reference 10). The estimated

virtual origin location is shown on Figure 9, marking the location $X_T = 0$. The method of computing the virtual origin, explained in Reference 10, will be contested by the data presented later in this report. In the meantime, since meaningful measurements could be made only for $M_2$ curves near the center of the test aperture, Figure 9 indicated the choice of $M_2 = 1.5$.

## 4. Matrix of Experimental Conditions

As a result of the transition expectations of Section 2 and the design considerations expressed in Section 3, the following initial experiment conditions were set:

$M_1 = 3$

$M_2 = 1.5$

$p_{o_1}/p_{o_2} = 10$

$T_o = 100°F = T_{o_1} = T_{o_2}$

$p_{o_1} = 300 - 600$ mm Hg. abs.

At these conditions the expected $\lambda$ was 0.18, the expected $Re_{XT}/C'' = 24$ ($Re_{XT} = 1{,}300{,}000$) according to Figure 4 and $Re_{hT}/C' = 45$ ($Re_{hT} = 10{,}500$) according to Figure 2. Furthermore, Figure 9 indicated, at $\lambda = 0.18$, that transition would be controlled by the FSL character (profile) of the flow rather than by its wake character. Finally, according to the expectations of Figure 7, by changing $p_{o_1}$ *from 600 to 300 mm. Hg., the transition* point should be observed to move from the T.E. to about 12" (30 cm.) downstream.

*The fixed ratio* $p_{o_1}/p_{o_2} = 10$ *indicated that the static pressures at* the exit of the two nozzles would be equal, so that the FSL was expected to progress down the middle of the tunnel undeflected.

We shall see further below that a variety of reasons combined to change the matrix, especially the levels of $M_2$, $p_{o_1}/p_{o_2}$ and $\lambda$.

## 5. Facilities and Equipment

### 5.1 Wind-Tunnel

These experiments were conducted in the Supersonic Wind-Tunnel at Montana State University (MSU/SWT). The facility is described in detail in Reference 11. A summary of its salient features is given below.

The wind-tunnel has been in almost uninterrupted use since the 1960's. It consists of a continuous, open-circuit flow facility with the components upstream of the test section consisting of the atmospheric inlet, a silica-gel air dryer with a dewpoint capability of -35°F doubling as an air heater, a throttling valve controlling the supply (stagnation) pressure and a large stilling tank. Downstream of the test section the air passes through supersonic and subsonic diffusers and the pumping plant driving the tunnel and is thence discharged to the atmosphere. A schematic of the tunnel circuit is shown on Figure 10.

In its normal configuration the test section is composed of a two-dimensional DeLaval nozzle designed for exit M = 3.0, terminating in a 3.1" x 3.2" (7.87 x 8.13 cm.) rectangular test section. The removable sidewalls are made of single pieces of optical-quality glass stretching from upstream of the nozzle throat to the diffuser entrance. Diagnostic probes can be suspended on vertical struts passing through the test-section ceiling and slaved to the electromechanical actuator system (Section 5.3.6). The test section flow is very uniform within ±0.04 of M = 3.

Control of the tunnel is maintained from a console with $p_0$ set point to ±1 mm Hg. abs., $T_0$ set point to ±1°F, and dewpoint readouts for points across the air dryer. Maximum $p_0$ is atmospheric (usually 625 mm Hg.) and maximum $T_0$ of order 150°F. Maximum and minimum unit Reynolds attained depend on configuration but vary from 80,000 $cm^{-1}$ to 20,000 $cm^{-1}$ respectively.

### 5.2 Modification of the SWT for the Present Measurements

In general outline the modification made to the SWT test section for the present measurements is shown on Figure 11, and is also illustrated in

the photographs of Figures 12 and 13. Basically the Mach 3 nozzle is "split in half" by positioning a flat splitter plate with a sharp T.E. along its centerplane. A "lower" channel is thus formed, visible in Figures 11, 12 and 13 of half of the original Mach 3 nozzle, with its floor being the lower block of the latter, and the flat plate forming its ceiling. The characteristics method predicts normal flow for this type of configuration, as already verified in the past for this tunnel (Reference 12). This "lower" channel is here frequently called the "fast" or "Mach 3" channel herein and its flow properties are subscribed by "1".

The upper surface of the flat plate was contoured to produce a Mach number $M_2 < M_1$ in the "upper" channel shown on Figures 11, 12 etc., whose ceiling was formed by another flat plate parallel to the SWT principal axis; this is hereafter called the "slow" channel and its properties are subscribed by "2". Air to provide this channel with flow was diverted from the main stilling tank, with a manually-controlled valve interposed, as shown on Figure 11. This valve controlled $p_{o_2}$, the low-speed channel stagnation pressure, while the main SWT throttling valve mentioned previously controlled $p_{o_1}$ and $p_{o_2}$ together. By means of this arrangement $p_{o_1}$ and $p_{o_2}$ could be set independently; or $p_{o_1}$ and $p_{o_2}$ could be raised or lowered in unison while their ratio remained fixed at a desired value. The stagnation temperature $T_o$ was always the same for both channels. In all cases the splitter plate spanned the test section completely.

The important parameters $M_1$, $M_2$, $\vartheta_1$, $\vartheta_2$, $Re_1'$, $Re_2'$ of the measurements were set by the upper-side contour of the splitter plate and the distance $x_1$ between its T.E. and the $M_1 = 3$ throat. The various configurations (or "modes") resulting from combinations of these are shown on Table I. The progression from mode I to mode III reflects the passage of calendar time and the desire to improve the $M_2$ nozzle contour and to solve the SWT choking problems; details on the flows obtained with each mode will be given below. Contour coordinates for the $M_2$ nozzle were provided by the short-nozzle theory of Shames and Seashore (Reference 13). The nozzle coordinates for modes II and III are shown on Tables II and III. The trailing edges were made as sharp as possible. Figures 11 and 12 show the geometries of the modes listed on Table I.

TABLE II. Coordinates of the M=1.6 Nozzle (Modes I, II)

| x (inch) | y (inch) |
|---|---|
| 0 | .35 |
| .6805 | .2571 |
| .8880 | .2298 |
| 1.0545 | .2081 |
| 1.1526 | .1954 |
| 1.2547 | .1822 |
| 1.4253 | .1607 |
| 1.5865 | .1411 |
| 1.6775 | .1303 |
| 1.8853 | .1069 |
| 2.0942 | .0852 |
| 2.474 | .0512 |
| 2.8414 | .0263 |
| 3.2729 | .0076 |
| 3.7117 | 0 |

TABLE III. Coordinates of the M=2.25 Nozzle (Mode III)

| x (inch) | y (inch) |
|---|---|
| 0 | .87864 |
| .52219 | .72387 |
| .640224 | .68893 |
| .709047 | .668604 |
| .757126 | .65443 |
| .795076 | .64327 |
| .82692 | .63392 |
| .854658 | .62579 |
| .901887 | .61199 |
| .94183 | .60036 |
| .976921 | .59018 |
| 1.02331 | .5768 |
| 1.06443 | .565 |
| 1.1018 | .554345 |
| 1.13635 | .54456 |
| 1.1687 | .53544 |
| 1.19929 | .52688 |
| 1.28917 | .50203 |
| 1.34572 | .48666 |
| 1.45038 | .4588 |
| 1.49977 | .4459 |
| 1.68586 | .39912 |
| 1.86225 | .35739 |
| 2.05676 | .31441 |
| 2.27339 | .2703 |
| 2.49424 | .22934 |
| 2.7219 | .1912 |
| 3.08047 | .13919 |
| 3.59892 | .08014 |
| 4.1743 | .0349 |
| 4.81843 | .0068 |

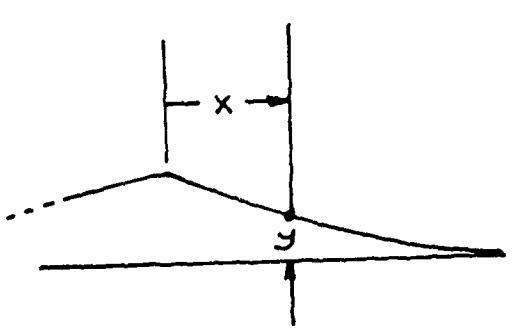

During the tests of the modes I, II, $II_a$, and III, various diffuser combinations were attempted, including a variable one consisting of two plates hinged at their junction, so that a variable wedge geometry could be generated by pulling wires through the test section ceiling.

## 5.3 Instrumentation

### 5.3.1 Schlieren Optical System

The SWT Schlieren system was extensively used to discern the overall flow features including choking phenomena, detect transition and even confirm the existence of vortical instabilities.

The system is based on the light from a tungsten source passing in parallel fashion through the test section windows. Photography of the image was done both in continuous exposure and by spark; the latter has an equivalent exposure time of one microsecond. Schlieren observations, which will be later shown by photographs, were greatly aided by the wide field of view of the flow made possible by the large window area of the test section.

### 5.3.2 Hot-film Anemometer

A hot-film anemometer was used to measure the location of transition and to make qualitative measurements of the turbulent intensity and its spectrum. The film consisted of platinum, approximately 0.002" x 0.02" (0.005 x 0.05 cm) in dimensions, and was deposited on the leading edge of a double wedge ground on the tip of a 0.02" (0.05 cm) diameter kimax glass rod. The probe was connected to either a Transmetrics 6401 or an ADP1213 hot-wire heating circuit and amplifier combinations. These circuits act both as generators of the heating current (usually about 20 ma d.c.) of the probe, and also as amplifiers of its a.c. signal. The upper frequency response of these amplifiers were 320 and 3,000 KHz respectively, with reponse compensation as high as 100 msec and gain to 50,000. For many of the observations the film signals were first recorded at 120 ips. on a 7-channel tape recorder with FM wideband response to 400 KHz.

Only a fraction of this capability was utilized, since no quantitative turbulence measurements were intended. Transition data were taken by judging the frequency extent of the signals and by their intensity within their active frequency band. Oscilloscopes, r.m.s. volt-meters and wave analyzers were used to make this judgement. Especially useful in this respect was the Rockland FFT512/S fast Fourier transform computer which provided smoothed spectra by repeated averaging.

### 5.3.3 Static Pressure Probe

Static pressure measurements were made with a probe consisting of a 0.056 cm-dia. tube with 3 holes drilled around its circumference at a distance of 0.46 cm from its sharpened tip. Signal-processing gear for this probe were identical to that connected to the pitot probe, and will be described below. The minimum lateral resolution of this probe equalled its diameter. No static pressure measurements were taken in the region downstream of the T.E. and for a length of 0.5 cm. from it.

### 5.3.4 Pitot Probe

The pitot probe was the principal instrument for the measurement of mean (average) flow quantities. It consisted of a 0.008" (0.02 cm) diameter tube, flattened and chemically etched at the tip to a lateral (y) dimension of 0.005" (0.013 cm.). Since the shear layer width was of order 0.15" (0.38 cm.) in width, this afforded a lateral resolution of $0.15 \div 0.005 = 30$ which is considered quite adequate. The probe tube was telescoped into tubes of progressively larger diameter, for rigidity, and terminated in a bullet-shaped housing which encapsulated a Kulite XTH-1-190-5A pressure transducer. The transducer housing itself was immersed in the flow, thus shortening the distance between probe tip and transducer and thereby greatly decreasing the response time.

The transducer was energized by 15.7 volts d.c. and had a pre-amplified sensitivity of 22.4 mv/v/mm. During data recording the transducer output was amplified by 100 and dynamically damped to eliminate electronic noise

and drift. The transducer was calibrated at least once every day during the tests.

### 5.3.5 Total Temperature Probe

The total temperature probe consisted of a type K thermocouple bead, 0.013 cm. in diameter, connected to a digital temperature indicator outside the flow. The calibration of this instrument v. Reynolds number will be given during the discussion of the data.

### 5.3.6 Electromechanical Positioning and Actuating

All flow-immersible probes were held with their tip on the vertical mid-span plane of the flow. They were supported in two degrees of freedom by the SWT electromechanical actuator, consisting of a horizontal hollow strut held in place by two vertical struts protruding through the ceiling. The vertical struts are actuated in the vertical (y) direction, while an independent motor drove the hollow strut along the flow (the x direction). The actuator control provided start/stop, speed and direction commands for either of these two motions, as well as digital counter and d.c. voltage position indications.

For the mean flow measurements the data were obtained in the form of "profiles", i.e. traverses along y at constant x. The SWT electromechanical actuator system allowed this traverse to be done fully automatically. The vertical motion is geared to a flywheel with adjustable spokes protruding from its periphery which periodically interrupt a photodetector beam, each interruption transmitting an electric "read" command to the SWT Data System. By adjusting the angular separation of the spokes around the flywheel, a "read" command at each of the vertical steps mentioned above is obtained. In addition, and to ensure adequate response time for the sensor, the system automatically produces a pause between sensor arrival at a new vertical point and the "read" command at that point, the pause being typically 15 seconds in length. The probe signals were acquired and stored by the SWT Data System which basically consists of a Spectral Dynamics Model SD-133

8-channel A/D converter and a Texas Instruments Silent 700 ASR computer terminal with dual cassette storage. This combination allows storage on cassette as well as real-time hard-copy printing of the line prompted by each "read" command. Alternatively an Intertek Superbrain microcomputer with dual 5-inch disk storage was also used in series, to provide CRT display of the data and disk storage.

TABLE I

NOZZLE CONFIGURATION MODES

| | I | II | IIa | III |
|---|---|---|---|---|
| $M_1$ nominal | 3 | 3 | 2.7 | 2.88 |
| $M_1$ actual | 3 | 3 | - | 2.77 |
| Type 1 nozzle | contoured[3] | contoured[3] | contoured[3] | contoured[3] |
| $M_2$ nominal | 1.56 | 1.6 | 1.6 | 2.25 |
| $M_2$ actual | 1.47 | - | 1.74 | 2.18 |
| Type 2 nozzle | straight | contoured[1] | contoured[2] | contoured[3] |
| $x_1$, inch (cm) | 10.4" (26.4) | 10" (25.4) | 5" (12.7) | 6.65 (16.9) |
| $x_2$, inch (cm) | 4.15" (10.5) | 3.71" (9.42) | 3.71" (9.42) | 4.8 (12.2) |
| $\lambda$ nominal | 0.167 | 0.159 | 0.139 | .0537 |
| $\lambda$ actual | 0.187 | | | .0542 |

1 Template

2 Template modified by hand

3 Numerically-controlled mill.

## 6. Results

### 6.1 Preliminary Results With Modes I and II

The initial measurements, as per the planned matrix of Table I, were carried out with Modes I and II for which the lower-speed channel used a Mach 1.6 nozzle. This was primarily a "shakedown" experiment, aimed at judging the overall performance of the modified SWT test section. As such, much effort went into observing design defects, into making modifications and into explaining the overall flow phenomena observed.

Modes I and II aimed at achieving the flow conditions shown on Figure 9, i.e., a long FSL parallel to the tunnel axis, with $M_1 = 3$, $M_2 = 1.6$ and $P_{O_1}/P_{O_2} = 10$. In an overall sense all the hardware performed properly; observations made with Mode I (see Table I) as well as with Mode II, shown in structural outline on Figure 13, produced the type of flow seen on Figure 14. However a number of difficulties were encountered at the outset. First, the desired $P_{O_1}/P_{O_2} = 10$ condition could not be achieved without flow breakdown at the nozzle exits, because of inadequate diffuser performance. Second, while satisfactory flow was achieved at off-design conditions of $P_{O_1}/P_{O_2} < 10$, this meant an increase in $P_{O_2}$ which in turn caused a downward deflection of the splitter plate; in turn, this caused an increase in $M_2$ and a decrease in $M_1$. Third, the contour of the $M_2$ nozzle, fabricated from a template, proved unsatisfactory for uniform exit flow. The combined result of these problems are vividly seen on Figure 14, in the form of a deflected FSL which in addition terminates into a maze of spurious shock waves and separated wall boundary layers before the diffuser entrance.

Original estimates had not indicated any potential problems with the SWT diffuser. This had been encouraging since it indicated no need to modify the entire diffuser section according to most recent "long-diffuser" ideas for dissimilar-stream flows (e.g. Reference 14). Prolonged efforts to improve the diffusion for Modes I and II, including the hinged variable diffuser already mentioned in Section 5.2, produced distinct, but not

drastic, improvements. It should be kept in mind, too, that the immersion of diagnostic probes in the test section (some are visible in Figures 12 and 13) provide additional obstacles to proper diffusion.

Relief to the choking difficulty appeared from an unexpected source, which will be described briefly here. It was found by measurements with the pilot tube, that the trailing-edge (initial) FSL thickness was considerably higher than originally estimated from Reference 4 and included in Reference 10. Specifically, Figure 15 shows the T.E. shear thickness $\delta_1 + \delta_2$ as calculated in the experiment design phase, and as measured for the Mode I-II tests. These measurements show considerable scatter because they were preliminary, but in anyway indicate a T.E. FSL thickness 2-3 times greater than anticipated. Since this finding had important effects on the experimental plan, an attempt to support it by independent theoretical means was sought. It had been previously found that, despite the curvature and pressure gradients present in DeLaval nozzles, reasonable estimates (to less than 15%) of their boundary-layer thickness could be made using standard laminar-flow flat-plate theories such as that due to Low (Reference 15). Figure 16 shows that Low's theory supported data obtained in typical nozzles (in this case the MSU/SWT regular M = 3 nozzle) and verifies that the original FSL estimates were inappropriate.

The reason why these findings were important to the diffuser performance was that they re-directed the search for transition closer to the T.E. (since an originally thicker FSL generally requires a smaller wetted length to transition). This made the requirement for a long FSL unnecessary. Flow breakdown phenomena near the diffuser entrance could be tolerated, therefore, so long as a few inches (or even a few centimeters) of FSL length were obtained downstream of the T.E. Further work on improving diffusion was therefore stopped, and for the remainder of this report we deal with FSL's of the type and extent shown on Figure 14.

The setback caused by the findings of Figure 15, however, was that they negated eqs. (6) and (7); thus although transition predictions on the basis of thickness (eq. (4) and Figures 2 and 7, for example) remained

valid, predictions based on wetted length (eq. (7) and Figure 4) did not. To continue expressing transition expectations on a Re' - x plane, one needed a valid h(x) relation to replace eq. (6). According to the Appendix, such a relation can be obtained from the exact theory, but requires tedious computations for each given parameter group ($M_1$, $M_2$ etc.).

Therefore, it was decided to reconsider the tests underway in terms of the $P_{O_1}$, h plots shown in this report beginning with Figure 17. In this representation it is recognized that $P_{O_1}$ and $P_{O_2}$ may be arranged so that the FSL at the T.E. will deflect up or down by an angle $\alpha$. Thus any set of nozzle-exit $M_{e_1}$, $M_{e_2}$, $P_{O_1}$, $P_{O_2}$ etc. produces a different set of $M_1$, $M_2$ etc. where the latter is now the true properties on either side of the deflected FSL, as is shown on Figure 18. In turn, this allows the computation of $\lambda$ and, from Figure 2, the transition Reynolds number $Re_{hT}$ and also the transition thickness h since Re' is now known. In Figure 17 the transition thickness h is thus plotted as a function of $P_{O_1}$ and $P_{O_2}$ for the Mode I-II nozzles, and the same is done on Figure 19 for the Mode IIa nozzle. One can of course also plot on such graphs the corresponding transition thickness if the flow "acted like a wake" (Section 2.4), as well as the initial (trailing edge) $h = \delta_1 + \delta_2$ for orientation purposes.

## 6.2 Instability and Transition Results for Modes I and II

The conclusions from the work reported in the last section were that the observed FSL's of several inches in length, were suitable for making transition observations; the mechanical difficulties mentioned, however, limited any further experimentation with this mode valuable only in an exploratory sense.

The major flow feature explored was the turbulence content of this FSL at $P_{O_1}$ = 570 mm Hg, $P_{O_2}$ = 296 mm Hg. At these conditions, chosen because of the flow steadiness, the flow deflected toward the fast-flow channel (positive $\alpha$ in Figure 18), thereby decreasing the speed difference between the two channels; it is estimated that $M_1 = 2.8$, $M_2 = 1.8$ and thus $\lambda = 0.11$. It is also estimated that both boundary layers were laminar at the T.E.

Figure 20 shows profiles of the hot-film wideband a.c. output across the shear layer, for progressively increasing distances x from T.E. These exhibit two distinct "peaks" on the sides of the FSL, which grow quickly from the T.E. to a distance of about 2.5 cm. from the T.E. and thereafter decay. Spectra of the probe signals along both the top and the bottom "peaks" are shown on Figures 21 and 22. The first trace on each figure is taken so close to the T.E. that they can be considered to be at x = 0, i.e. in the two T.E. boundary layers. These spectra shed additional light into what causes the wideband signals. It is seen from Figure 21 that an "energy peak" appears within a fraction of an inch past the T.E., which centers at about 75 KHZ. This peak actually appears first on the upper (low-speed) side of the FSL, and is accompanied also by signal increases at the higher frequencies. Note that the frequency of the peak does not change as far from the T.E. as 3.6" (9.1 cm). By that time it is seen from the spectra, that the oscillation has quite well vanished from the upper (low-speed) side of the FSL, while it persists in the lower (high-speed) side.

The following conclusions were drawn from this measurement:

(a) The transition picture is complex and involves asymmetries and non-uniformities both in the spectral and spatial sense.
(b) If turbulence is identified as a spectral activity at high frequencies, it appears that transition sets in quite abruptly within one centimeter or so from the T.E.
(c) An intense periodic phenomenon appears as soon as the two flows meet just beyond the T.E. The periodicity decays quickly on the slow side of the FSL but remains practically intact for long distances on the fast side of the FSL.

These conclusions led to a tentative picture of events in the FSL, which consists of the FSL forming initially as a laminar flow, but almost immediately changing to one which is both turbulent and oscillatory. A very close parallel in low-speed flows can be found in Reference 16.

As for transition, Figure 17 had already predicted that for this mode the FSL forming at the T.E. was already of a thickness which would require it to be turbulent, according to the asymptotic theory. The flow should thus become turbulent as soon as possible beyond the T.E., which is confirmed by the above observations.

## 6.3 Results With Mode III

### 6.3.1 General

This configuration, shown on Figure 13 and Table III, was designed to produce initial boundary layers at the T.E. thinner than would be required for transition. With the latter thus expected some distance downstream of the T.E. it was thought that a clearer picture would be obtained of the $h_T$ (Re′) dependence, for which predictions appear on Figure 23.

Figure 24 shows Schlieren photos of typical flows obtained with this configuration. Absence of shock waves and other disturbances indicates proper nozzle flow.

Study of Mode III began with an effort to see if the boundary layers merging at the T.E. were laminar or turbulent; since the present program requires initially laminar FSL at the T.E., it follows that flow conditions, where either boundary layer was already turbulent, should be avoided. With the hot-film anemometer held within the boundary layer just upstream of the T.E., the film output was observed as the stagnation pressure was changed. This qualitative measurement is frequently used as a rapid means of ascertaining the presence of turbulence (Reference 17). It is based on the ability of this sensor to produce a large a.c. signal if immersed in turbulence, this signal decreasing to zero when the flow is laminar.

Figure 25 shows two such sets of film signal vs. Po data for each nozzle, one at the T.E. as indicated, and another at a corresponding point on the opposite wall directly across from the T.E. For the M = 2.25 nozzle

one sees the signal begin from a high level at $P_{o_2}$ = 500 mm Hg, decreasing to a low level barely visible above the electronic noise when $P_{o_2}$ = 100 mm. The interpretation of these traces is that for the slow-side nozzle turbulence first appears at about 200 at the T.E., but is not fully established until beyond 500 mm. This behavior is matched by the boundary layer on the "ceiling" of the M = 2.25 nozzle, as it should.

Without changing its sensitivity, the probe was next moved into corresponding points in the boundary layer of the Mach 3 nozzle, where the remaining two traces of Figure 25 were obtained. For this case it appears that transition barely begins at $P_{o_1}$ = 600 mm, while below that level the Mach 3 boundary layer is laminar. The conclusion of this measurement was that $P_{o_2}$ should be kept below 200 mm Hg for all subsequent tests, while $P_{o_1}$ could be unrestrictedly set at any level.

Another cause of constraint for $P_{o_1}$ and $P_{o_2}$ were the desire to keep the FSL parallel to the tunnel axis. Considering the actual exit M for the fast nozzle ($M_1$ = 2.8 versus the nominal 3.0) the two exit pressures would be equalized if $p_{o_1} \simeq 2.3 p_{o_1}$.

The result of these preliminary tests was the "design" of the Mode III measurements at $p_{o_2}$ = 170 mm and $p_{o_1}$ = 425 mm. In addition to steadier operation achieved in the tunnel by these two settings, Figure 23 shows the possibility of observing transition some distance downstream of the T.E. as desired. Specifically, Figure 23 says that at the T.E. the laminar FSL thickness would be 0.375 cm, while the expected transition thickness would be about 0.47 cm. That is, the FSL was thus required to first thicken before it became turbulent, and transition was thus not expected for some distance behind the T.E.

### 6.3.2 Mode III Nozzle Flow

All subsequent tests described in this report were done with Mode III at $p_{o_1}$ = 425 mm Hg, $p_{o_2}$ = 170 mm Hg and $T_{o_1} = T_{o_2}$ = 605° R. The quality of the flow emerging from the two nozzles can be seen on Figure 26. The

uniformity of the velocity at the exit plane, which is better than 1%, attests to the care in fabricating the nozzle contour.

Figure 27 shows the static pressure distribution in the flow direction along the ceiling of the "slow" nozzle, along the floor of the fast nozzle, and also along the FSL between the two streams. The only noteworthy feature here is an apparent longitudinal pressure gradient along the FSL, amounting to $(dp/dx)/p \sim 0.04\ cm^{-1}$ (in terms of the FSL thickness h, $(h/p)\ (dp/dx) = 0.01$) due to slight nozzle underexpansion. As we shall see later, however, flow quantities combined to produce much smaller gradients in the other FSL edge properties.

The boundary layer thicknesses at the T.E. are shown on Figure 28. At $p_{o_1} = 425$ mm Hg, $\delta_1 = 0.181$ cm, and at $p_{o_2} = 170$ mm Hg, $\delta_2 = 0.216$. Although these do not compare individually any better than expected with Low's theory (also shown on Figure 28) their sum of 0.397 cm is in almost perfect agreement with the expectation of 0.396 cm shown on the predictions of Figure 23.

The momentum thickness at the T.E. is shown on Figure 29. Some reservations about the measured values of $\theta_1 = 0.0128$ cm and $\theta_2 = 0.0158$ are expressed at this time because of resolution problems with the pitot probe.

### 6.3.3 Edge Properties and FSL Thickness

Figures 30 through 34 show the development of the edge properties on either side of a 3-inch (7.5 cm) length of FSL, including the thickness h, the $M_1$ and $M_2$ and also p, u and $Re_1'$. The noteworthy feature of these findings, which are needed to pin-point the transition Reynolds number, is that although p has a clear gradient, the other properties vary only negligibly along the FSL edge, as can be seen from the following Table.

TABLE IV. Variation of Edge Properties

| | p (mm) | u (m/sec) | M | $Re_1'$ ($cm^{-1}$) |
|---|---|---|---|---|
| Fast Side (1) | | | | |
| Minimum | 13.1 | 651 | 2.88 | 37,400 |
| Maximum | 16.4 | 657 | 2.93 | 40,000 |
| Max. Deviation | 3.3 | 6 | 0.05 | 2,600 |
| Average | 14.7 | 654 | 2.9 | 38,700 |
| Slow Side (2) | | | | |
| Minimum | -- | 577 | 2.25 | 20,400 |
| Maximum | -- | 589 | 2.32 | 21,700 |
| Max. Deviation | -- | 12 | 0.07 | 1,300 |
| Average | -- | 583 | 2.28 | 21,100 |

According to this Table the maximum streamwise variations in u, M and Re', are 2%, 3% and 7% respectively. Also note that, the $\lambda$ as defined in eq. (5) is

$$\lambda = \frac{u_1 - u_2}{u_1 + u_2} = 0.0584$$

6.3.4 Flow Profiles Across the Shear Layer

Figures 35 and 36 show typical profiles across the FSL. Of these the most noteworthy are the static pressure and total temperature profiles of Figure 35. The former demonstrates the uniformity of pressure across the flow, while the latter shows that the slower stream is about 10° R cooler than the faster stream. This can be attribted to the design of the secondary channel through which small heat losses were possible. Note that, in anyway, this 10/600 = 2% fractional $T_o$ difference has only negligible differences in the transition prediction.

The data of Figure 34 indicate that nine sets of profiles were taken along the FSL in the region $0 < x < 3$" from the T.E. As will be shown below, these were taken while the FSL was still laminar. In the next section, use of these data will be made in fixing the FSL transition Reynolds number based on thickness. The data of Figures 35 and 36 are also useful for future comparison with the laminar FSL theory described in the Appendix. The velocity profiles of Figure 36 are especially useful in confirming that the "wake" component is still present for a distance of 3" (7.5 cm), which corresponds to a distance of about 260 total momentum thicknesses at the T.E. This is an important finding indicating that the flow profile has not yet achieved the shape on which the FSL transition theory is based, so that agreement with the latter is not necessarily expected.

The mean flow field in the shear layer is discussed in greater detail in Reference 18.

### 6.3.5 Transition to Turbulence

The evidence as regards transition, which was provided by the Schlieren system, is shown on Figures 37, 38, and 39. The former two show the FSL as the ratio $P_{O_1}/P_{O_2}$ remains at the "design" level of 425/170 = 2.5 but $P_{O_1}$ itself is varied over the available range $200 < P_{O_1} < 600$ mm Hg. According to the thinking expressed in Secion 2 of this report transition is Reynolds-number-controlled, so that for fixed $\lambda$ the transition zone should move along the FSL as $P_{O_1}$ is varied.

This is the case, according to Figures 37 and 38. The former is a series of Schlieren photos with continuous exposure, while the latter is a a series of spark photos. The onset of transition in continuous exposure appears, as always, as a widening of the FSL and a loss of "black-white contrast" due to the decrease of density gradients. In the spark photos a considerable amount of structure is visible in the turbulent FSL. In both types of photos the transition location is quite clear and it moves downstream as $P_{O_1}$ is decreased.

Figure 39 shows spark and continuous-exposure photos for the specific conditions of the Mode III results discussed in the previous Section, i.e., $P_{O_1}$ = 425 mm Hg and $P_{O_2}$ = 175 mm Hg. For these conditions it appears that transition occurs at a distance of 2.5" ± 0.2" (6.35 ± 0.5 cm) from the trailing edge.

Transition evidence in much more detailed form was also collected with the hot-film anemometer, with results shown on Figures 40 through 42. This study exploits certain tell-tale characteristics of the hot-film output behavior in geometric and Fourier space. In this instance a "map" of the film output in space was first made up by traversing the hot film normal to the FSL at several positions x along a 4-inch (10 cm) length, at regular intervals away from the T.E. During each traverse the output was continuously recorded on seven-track, 1/2-inch analog magnetic tape at 120 i.p.s., with a frequency response of 400 khz. This method allows careful review and analysis by playing back the tape, after the end of the tunnel run, at reduced speed.

Plotted on Figure 40 is the r.m.s. wideband ($f < 400$ khz) hot-film output vs x and lateral distance y, in the range $0 < x < 10$ cm (or $0 < x < 4$"). Considering the electronic noise magnitude shown and the origin ("zero") for each trace, it is seen that a.c. signals are not obtained from the FSL until x = 1.5" from the T.E. Beyond x = 1.5" the wideband signal becomes evident near the FSL center, indicating some sort of oscillating flow. The signal begins decreasing toward x = 4".

A second "pass" over the same data was next made by looking at the output spectrum each time the film found itself at the position giving the maximum intensity wideband output (the "peaks" of Figure 40). Twelve such spectra are shown on Figure 41. Each spectrum shown stretches over the frequency range $0 < f < 320$ khz. Again, no oscillations are observed until x = 1.5", beyond which a strong oscillation centered at 93 khz is seen to develop. The oscillation increases until it reaches a maximum at about 3.25", beyond which it begins decaying.

The 93-khz signal thus represents an instability growing to detectable proportions by x = 1.5" and reaching a maximum at x = 3.25". In fact, careful scrutinizing of the Schlieren pictures (Figures 38 and 39) confirm that such a wave-like phenomemon is present in the FSL. The spectra of Figure 41 provide additional information on the instability. For examp e, if we assume that the waves convect with the stream speed (u ≃ 620 m/sec. according to Table IV) then their length, both absolute and relative to the thickness h (cf. Figure 30) can be computed:

$$\text{wavelength} = \frac{u}{f} = 0.67 \text{ cm} = 1.6 \text{ h}$$

Besides the inherent instability shown on Figure 41, the high-frequency content (f > 100 khz) of the spectra also begins increasing at large x. As already discussed in connection with the Mode I, II results (Section 6.2), this represents the actual turbulence becoming active. To study this growth separately, the traverses shown on Figure 40 were repeated once more, except that now only the signal at f = 175 khz (thought to be representative of the turbulence content) was plotted against y. The results are shown on Figure 42. The increase of these high-frequency signals as x increases is obvious.

Figure 43 compares the downstream history of the wideband oscillations as well as those at 93 and 175 khz. It is seen that for the first 2-2.5 cm beyond the T.E. the FSL is completely quiescent (this represents a length of about 5 - 7 thicknesses). In the range 3 - 8 cm all Fourier components increase in magnitude. The instability peaks at about 8 cm, while the turbulence itself peaks about 1 cm later, at 9 cm. The simultaneous growth of discrete oscillations along with the growth of turbulence, and the decay of the oscillations before the decay of the turbulence itself are common to transition in shear flows.

Clearly, and as fully expected, the transition cannot be thus located at a "point" x. From Figure 44 it seems that the process begins at x = 3 cm and ends at 9 cm, for a factor of 3 "spread" in wetted length x. This

range corresponds to a wetted-length Reynolds number

$$Re_{xT} = \frac{u_1 x}{\nu_1}$$

from 116,000 to 350,000. As will be seen in the next section, however, the thickness h varies so little in $3 < x < 9$ cm (see Figure 30), that a "point" in the $Re_{hT} = u_1 h/\nu_1$ can indeed be obtained.

Finally, a comparison of the Schlieren with the hot film observations shows that the $x_T$ determination by the former ($x_T$ = 2.5" = 6.3 cm) lies in the middle of the transition zone determined with the latter. Partly because it thus acts as an average to the range, the distance $x_T$ = 2.5" will be henceforth considered as the measured transition "point."

## 7. Discussion of the Transition Observations

The Mode III results give the main quantitative indications of transition location, which can be discussed in the context of the asymptotic theories presented in Section 2. To this end, the transition Reynolds number $Re_{hT}$ was formed from the data, using the average fast-side unit Reynolds number $Re_1' = 38{,}700\ cm^{-1}$, and the indicated dimensionless speed ratio $\lambda = 0.0594$ (see Section 6.2.3). The FSL thickness h where transition occurs is obtained from Figure 43. Using $h = 0.415$ cm at $x = 2.5"$, one obtains $Re_{hT} \simeq 15{,}500$ by which the datum on Figure 44 is plotted.

Figure 44 also plots the FSL transition expectation as obtained from eq. (4) and Figure 2, for the average observed $M_1 = 2.9$ (see Table IV). The asymptotic limit ($\lambda = 0$) for a wake-type flow is also plotted, first by computing the requisite $Re_w$:

$$Re_w = 2Re_1' (\theta_1 + \theta_2) = 38{,}700 \times 2 \times 0.0286 = 2200$$

and then finding $Re_{hT} \simeq 22{,}500$ from eq. (4) or Figure 2.

Several critical comments can be made about the results shown on Figure 44. First, it appears that the agreement between data and predictions is very good, especially considering the nature of the theory and the difficulty in defining transition onset. Secondly, it can be said that, if the theoretical curves are taken literally, the 25% difference between the test datum and the prediction represents the expected departure from the theory due to the "hybrid" flow profile which is neither a wake nor a FSL (see profiles at $x \simeq 2"$ and $3"$ in Figure 36).

Third it can be speculated, as already done ealier on Figure 6, that the actual transition Reynolds number curve joins smoothly the $\lambda = 0$ and $\lambda = 1$ limit via the dotted portion shown as "speculative" on Figure 44. If this is true, then the datum obtained bridges an important gap in the understanding of transition as viewed by the present theory of Section 2.

Finally, it must be kept in mind that $h$ grows slowly with $x$, which is true for almost all boundary-layer flows. If a prediction that something will occur at a certain value of $h$ carries along a probable error, this error is greatly magnified in terms of $x$. Thus, even if the present theory is capable of good transition estimates in terms of FSL thickness, it can predict the distance of transition from the T.E. only to the extent to which reliable predictions for $h(x)$ exist.

Quite separate from the transition-location issue is that of the role of instabilities in the shear layer. Although instabilities are a natural precedent of transition in free shear flows, the attention they have recently attracted is more due to their potential as a cause of large-scale mixing. If one was to judge from the evidence at low speeds alone, such "laminar mixing" could be of great importance, say, to laser devices. The present experiments, however, indicate conditions for which unstable vortex or wave structures develop only after some distance downstream of the T.E.; and once they do, their amplitude is still no greater than the laminar FSL thickness itself. It is therefore submitted that for such cases large periodic motions of the FSL do not seriously contend to the mixing process.

## Conclusions

The following was learned from the work performed so far:

1) The threshold-based transition theory for free shear layers was found to need modification when the shear layer is formed by a partition initially separating the two streams. By recognizing the existence of the boundary layers shed from the partition, finite transition Reynolds numbers were obtained for the entire range of speed ratios when such modifications were made.
2) A closed-form analytic solution for the FSL flow from the T.E. onward was constructed, which appears to be as accurate as exact (numerical) solutions, and which is much easier to use than the latter.
3) Shear-layer transition data obtained for $M_1 = 3$, $1.6 < M < 2.2$ and $0.05 < \lambda < 0.15$ were completely consistent with the theory mentioned under (1), above. Specifically,
    (a) When the theory predicted turbulence for a FSL shed off the T.E. while still laminar, the layer became turbulent immediately past the T.E.
    (b) When the theory predicted that the FSL would become turbulent only after some distance past the T.E. elapsed, this was found to be true experimentally. For $\lambda = 0.058$ the observations gave a transition Reynolds number of 16,000 which is within 25% of the prediction.
4) Laminar shear layers were obtained which were free of periodic oscillations. Such oscillations were in that case only present as pre-transitional instabilities, and were of amplitude and duration small enough to make them incapable of laminar-laminar mixing by themselves.

## References


1. Roshko, Anatol: Calif. Inst. of Technology, Private Comm., 1977-1982.

2. Demetriades, A.: "Transition In Free Shear Layers," Aeronutronic Report Report No. U-6573, Newport Beach, CA. December 1979.

3. Demetriades, A., Ortwerth P.J. and Moeny, W.M.: "Laminar-Turbulent Transition In Free Shear Layers," AIAA J. vol. 19, No. 9, Sept. 1981, p. 1091.

4. Demetriades, A.: "Necessary Conditions For Transition In A Free Shear Layer," MSU/SWT Report No. 80-1, Montana State University, Bozeman, MT February 1980.

5. Liepmann, H.W.: "Investigation of Boundary-Layer Transition On Concave Walls," NACA ACR 4J28, Washington, D.C. February 1945.

6. Mack, L.M.: "Linear Stability Theory And the Problem of Supersonic Boundary Layer Transition," AIAA J. vol. 13, No. 3, March 1975 p. 278.

7. Demetriades, A.: "Transition To Turbulence In Two-Dimensional Wakes," AIAA J. vol. 16, No. 6, June 1978, p. 587.

8. Birch, S.F. and Keyes, J.W.: "Transition In Compressible Free Shear Layers," J. of Spacecraft & Rockets, vol. 19, No. 8, Aug. 1972, p. 623.

9. Crawford, D.H.: "Investigation of The Flow Over A Spiked-Nosed Hemisphere-Cylinder at A Mach Number of 6.8," NASA TN D-118, Washington, D.C., 1959.

10. Demetriades, A.: "Transition To Turbulence In Non-Equilibrium Mixing Layers," MSU Proposal No. 80-018, Montana State University, Bozeman, MT March 1980.

11. Drummond, D., Rogers, B. and Demetriades, A.: "Design And Operating Characteristics of the Supersonic Wind-Tunnel," MSU/SWT Report TR 81-01, Montana State University, Bozeman, MT January 1981.

12. Laderman, A.J.: "Effect of Wall Temperature On A Turbulent Supersonic Boundary Layer," AIAA J. vol. 16, No. 7, July 1978, p. 723.

13. Shames, H. and Seashore, F.L.: "Design Data For Graphical Construction of Two-Dimensional Sharp-Edge-Throat Supersonic Nozzles," NACA RM E8J12, Washington, D.C. December 1948.

14. Amatucci, V.A., Dutton, J.C. and Adda, A.L.: "Pressure Recovery In A Constant-Area, Two-Stream Supersonic Diffuser," AIAA J. vol. 20, No. 9, September 1982, p. 1308.

15. Low, G.M.: "Simplified Method For Calculation of Compressible Laminar Boundary Layers With Arbitrary Free-Stream Pressure Gradients," NACA 2531, Washington, D.C. 1951.

16. Roshko, A.: "The Plane Mixing Layer: Flow Visualization Results And Three-Dimensional Effects," Int'l Conf. on Role of Coh. Struct. In Model Turb. and Mix., UAM-IBM Scientific Center, Madrid, Spain, 1980.

17. Demetriades, A.: "Boundary-Layer Transition In A Supersonic Nozzle Throat In the Presence of Cooling and Surface Roughness," MSU SWT TR 82-01, Montana State University, Bozeman, MT August 1981.

18. Brower, T.L.: "Experiments on the Mixing Layer Between Adjacent Supersonic Streams," M.S. thesis, Mechanical Engineering Department, Montana State University, Bozeman, MT 1983.

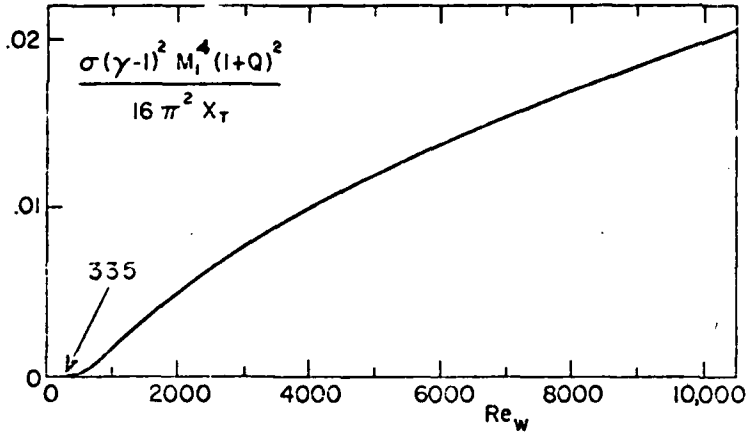


Figure 1. Wake transition distance vs. wake Reynolds number.

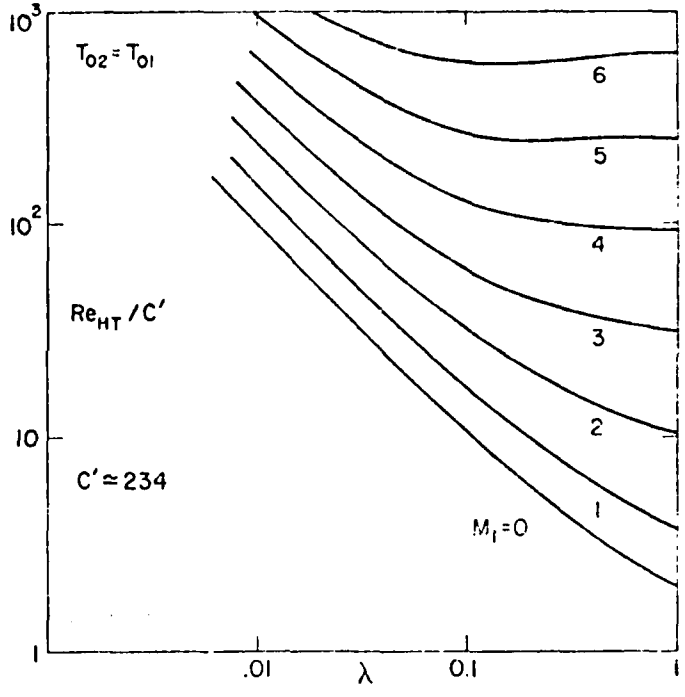


Figure 2. FSL transition Reynolds number based on FSL thickness.

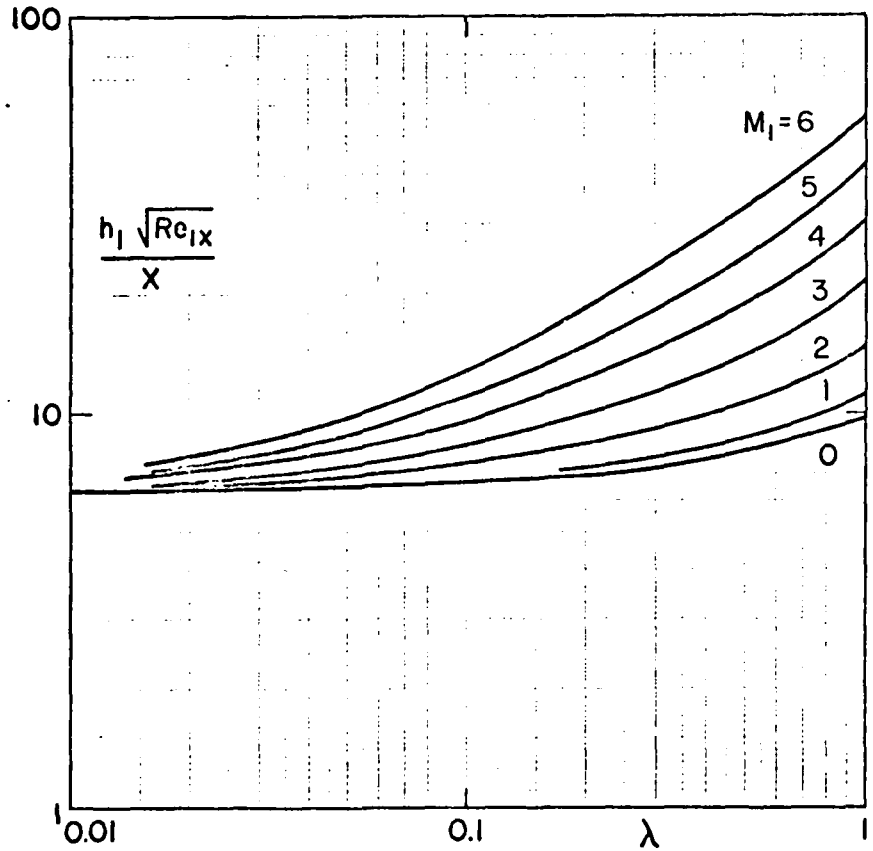


Figure 3. Original conception of FSL width (from Ref. 3).

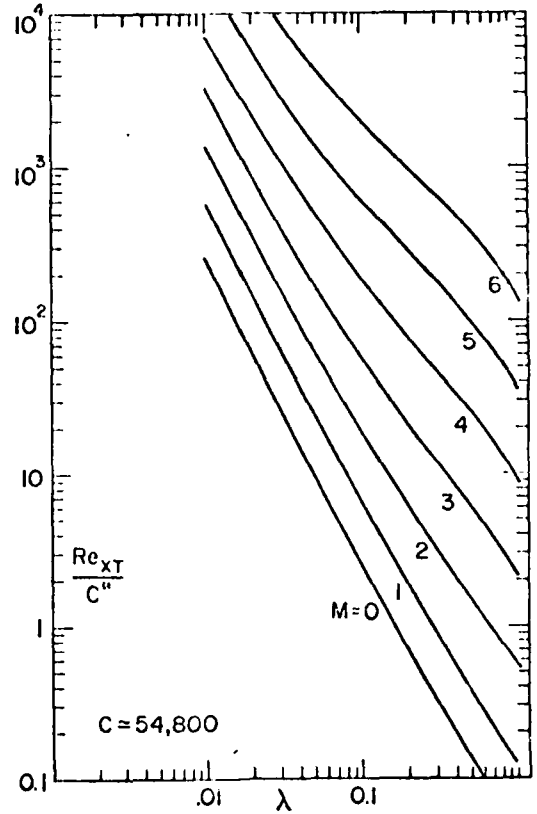


Figure 4. FSH transition Reynolds number based on distance from T.E.

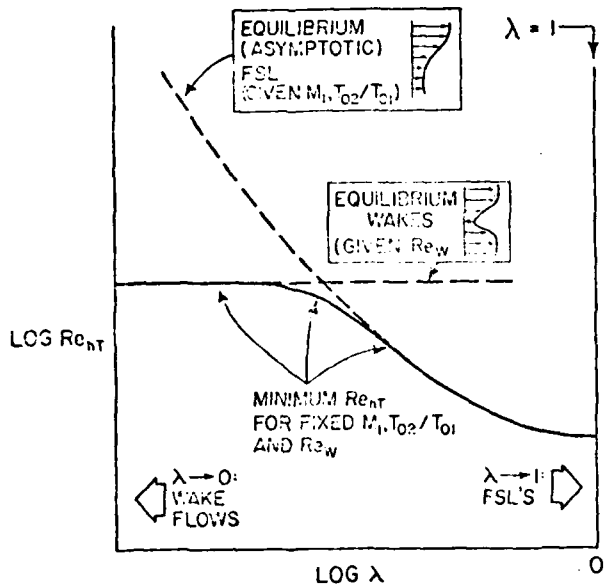


Figure 5. Thickness-based transition Re behavior for FSL's shed by partitions.

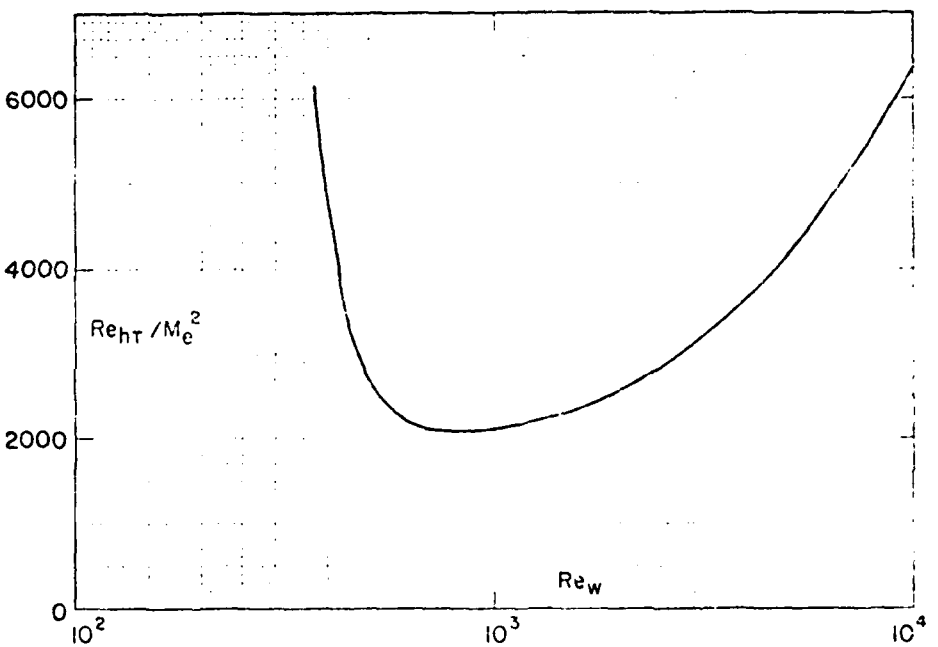


Figure 6. Wake transition Re based on thickness of wake.

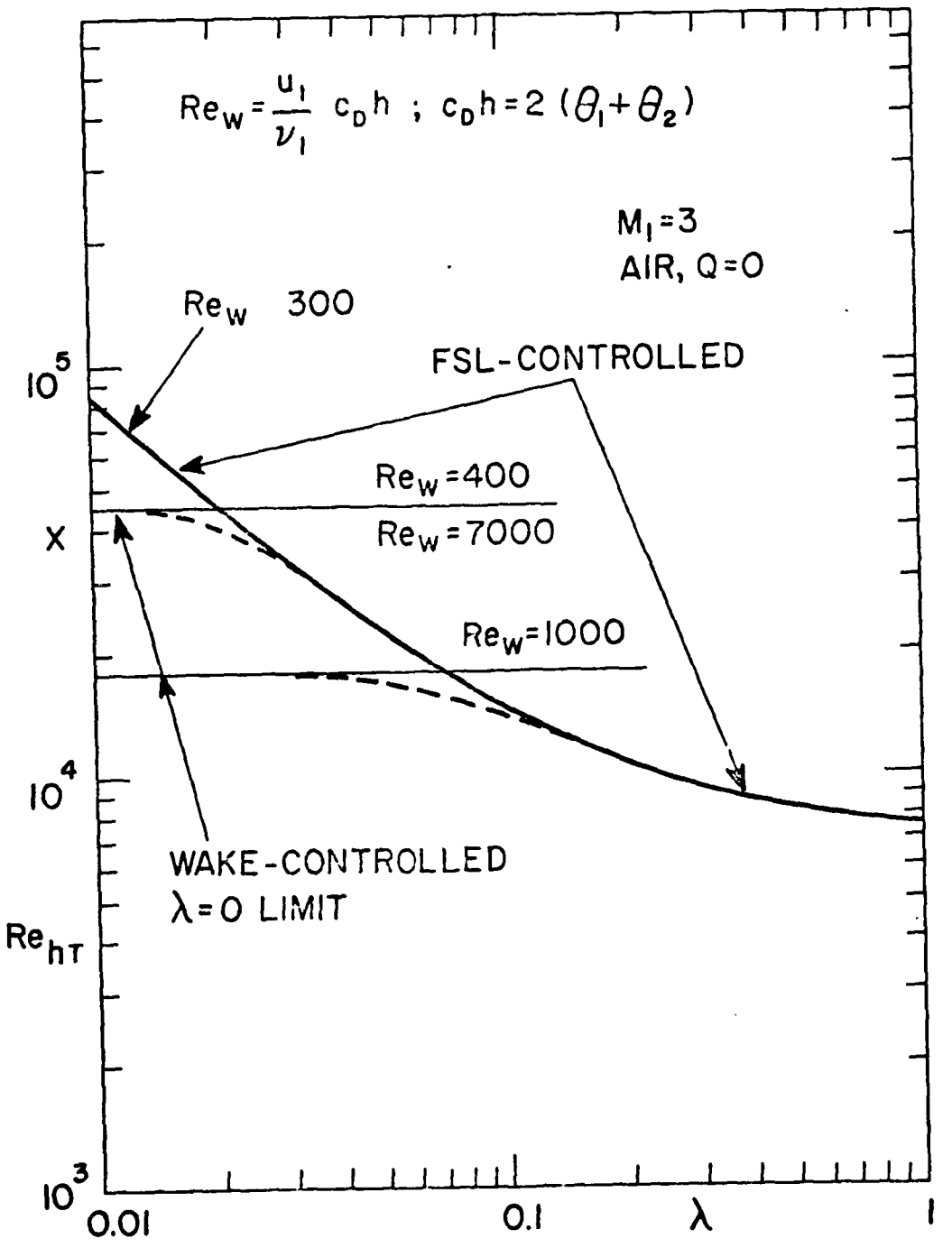


Figure 7. Transition on FSL's shed from partitions at $M_1 = 3$.

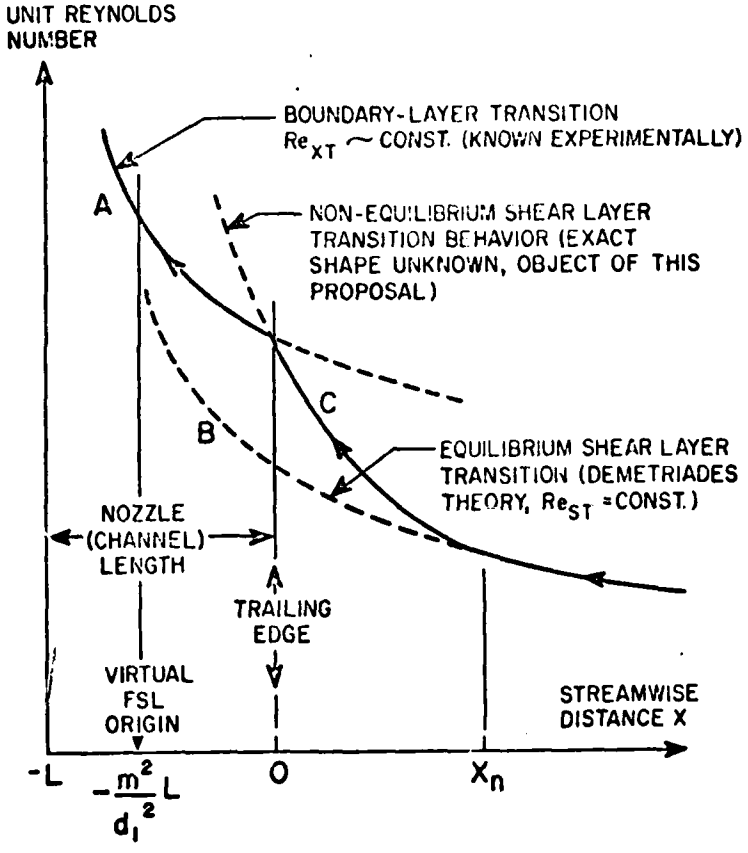


Figure 8. Conceptual statement of present problem.

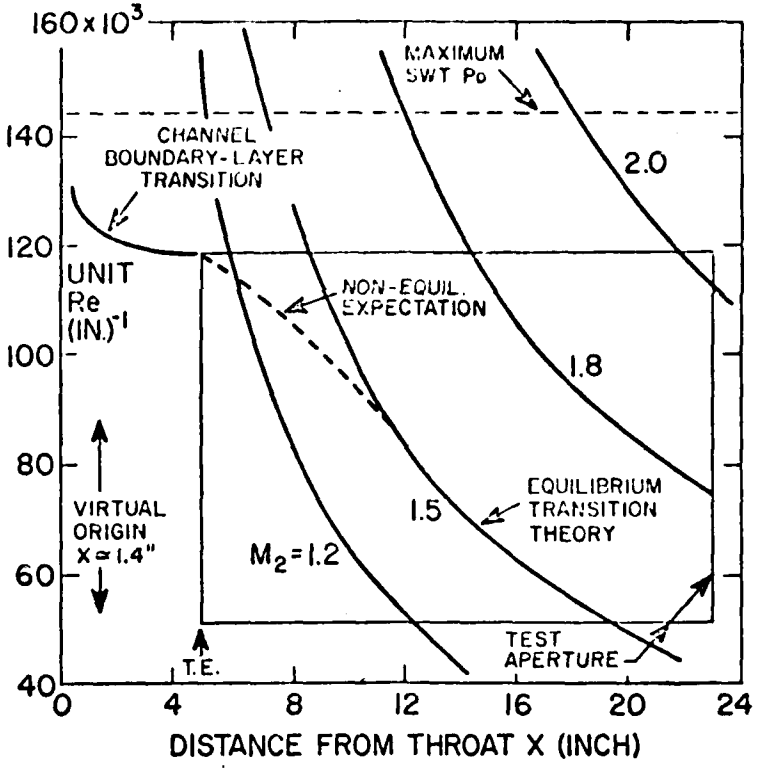


Figure 9. Original experiment design using wetted-length Reynolds numbers.

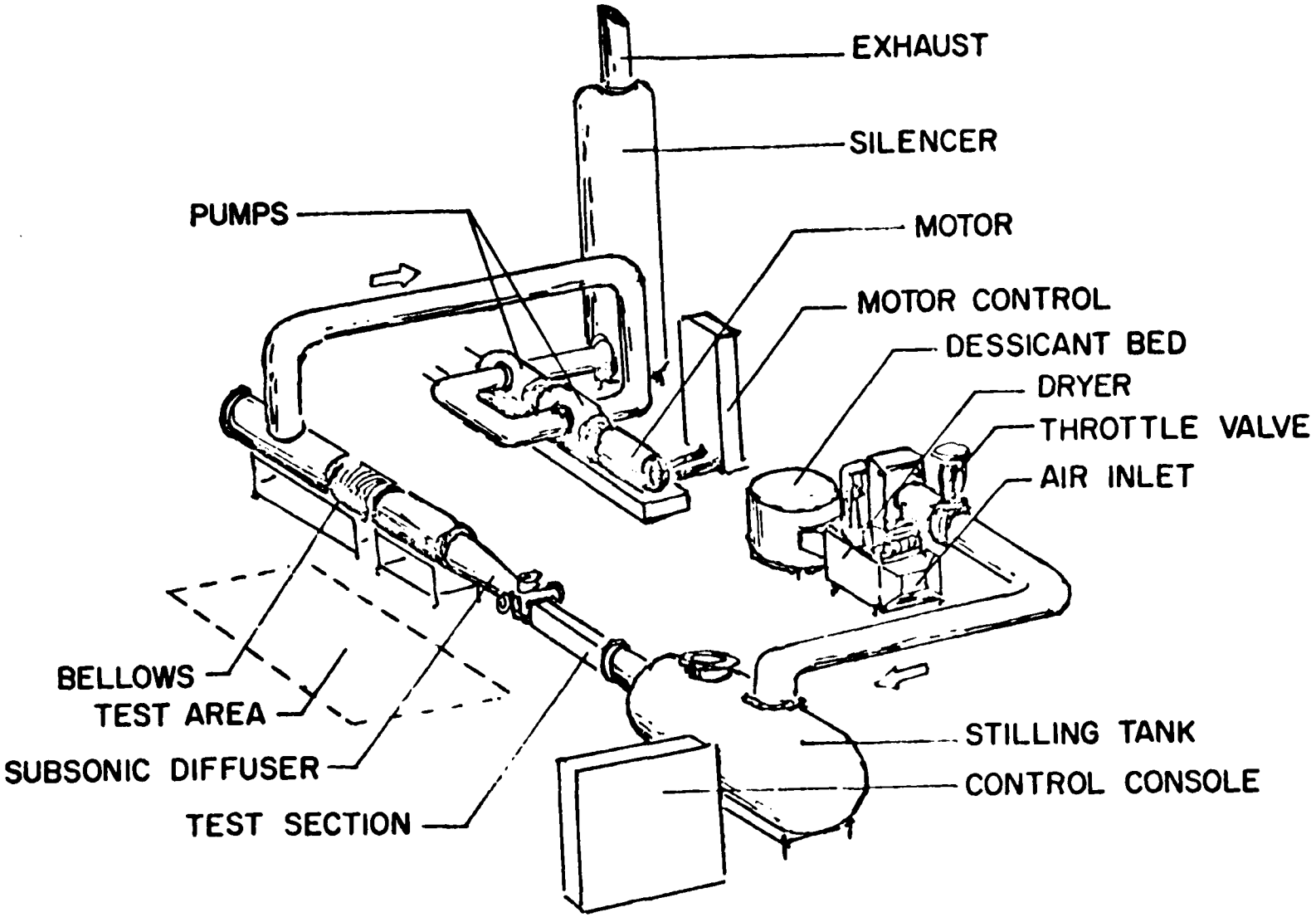


Figure 10. Overall view of the wind-tunnel showing major components.

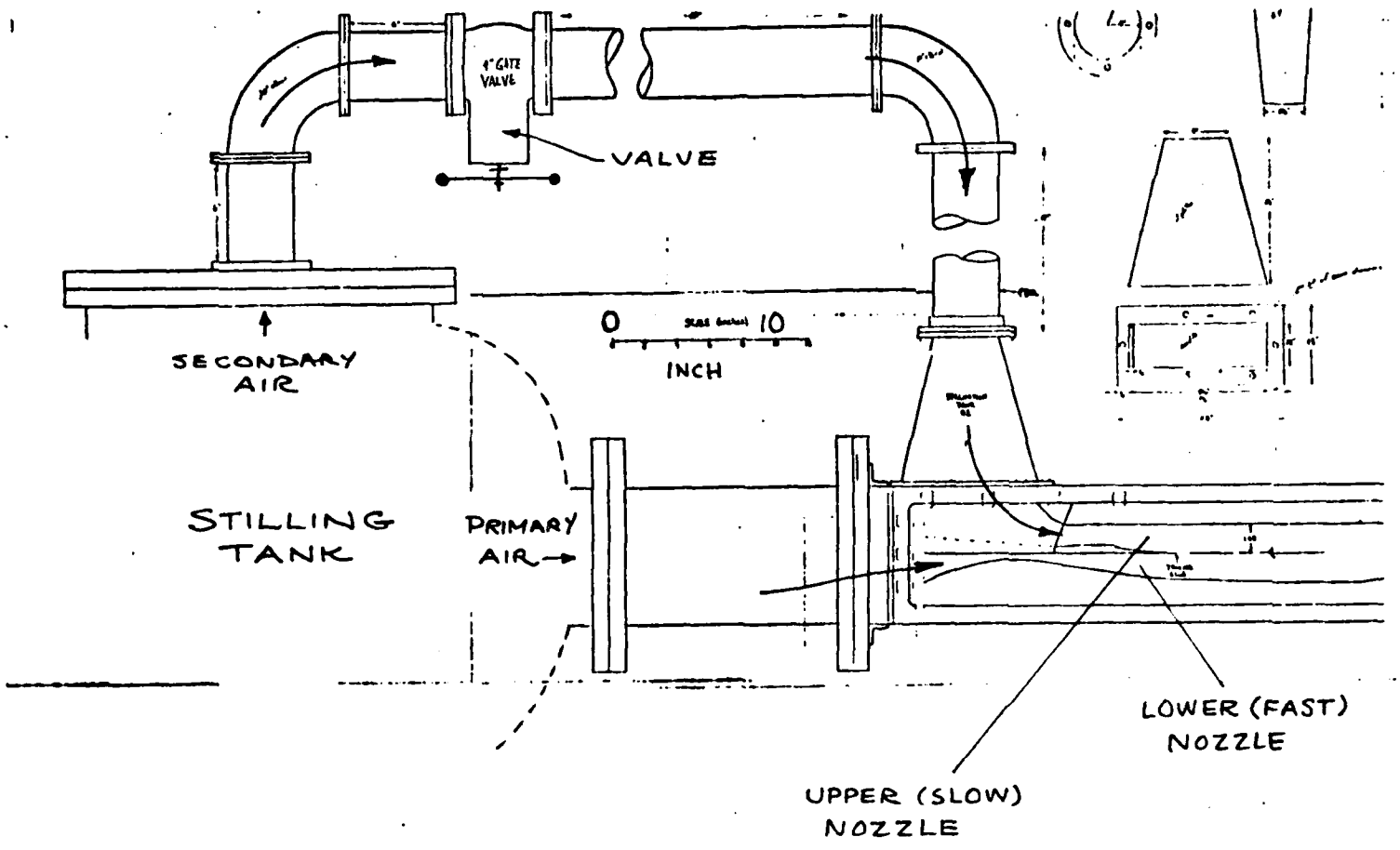


Figure 11. SWT modification for parallel-stream mixing.

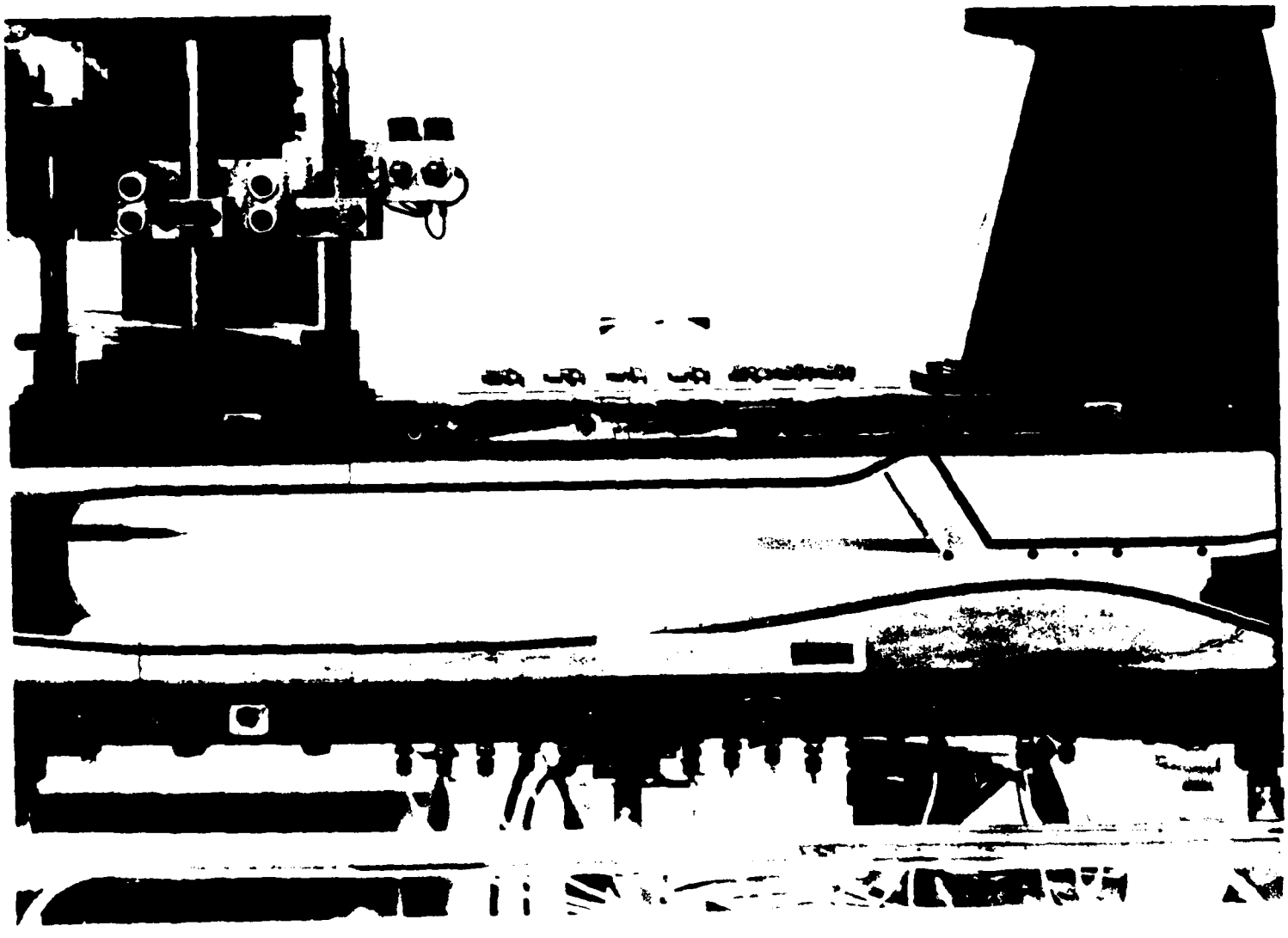

Figure 12. The Mode I configuration.

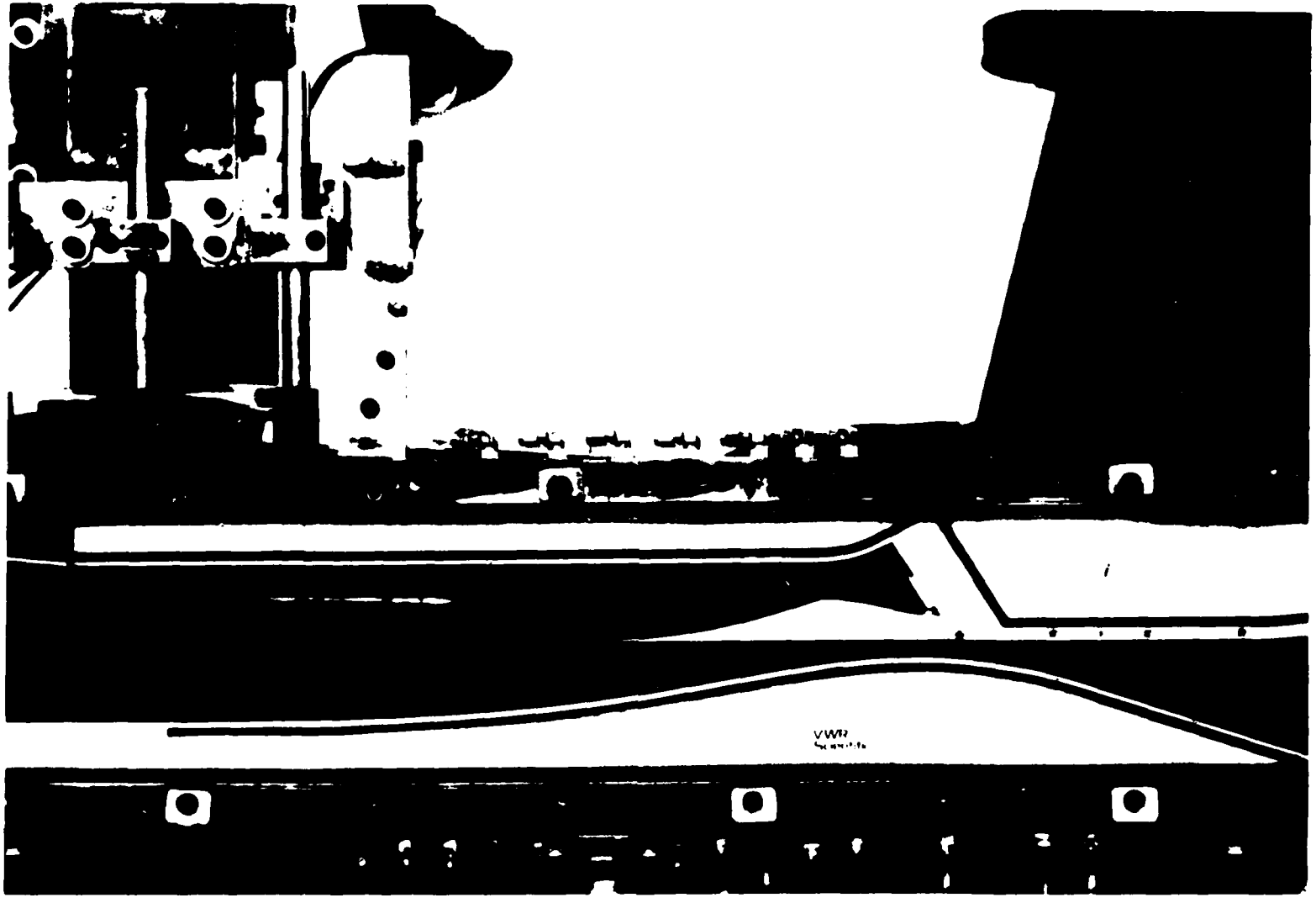

Figure 13. The Mode III configuration. Note probe installation.

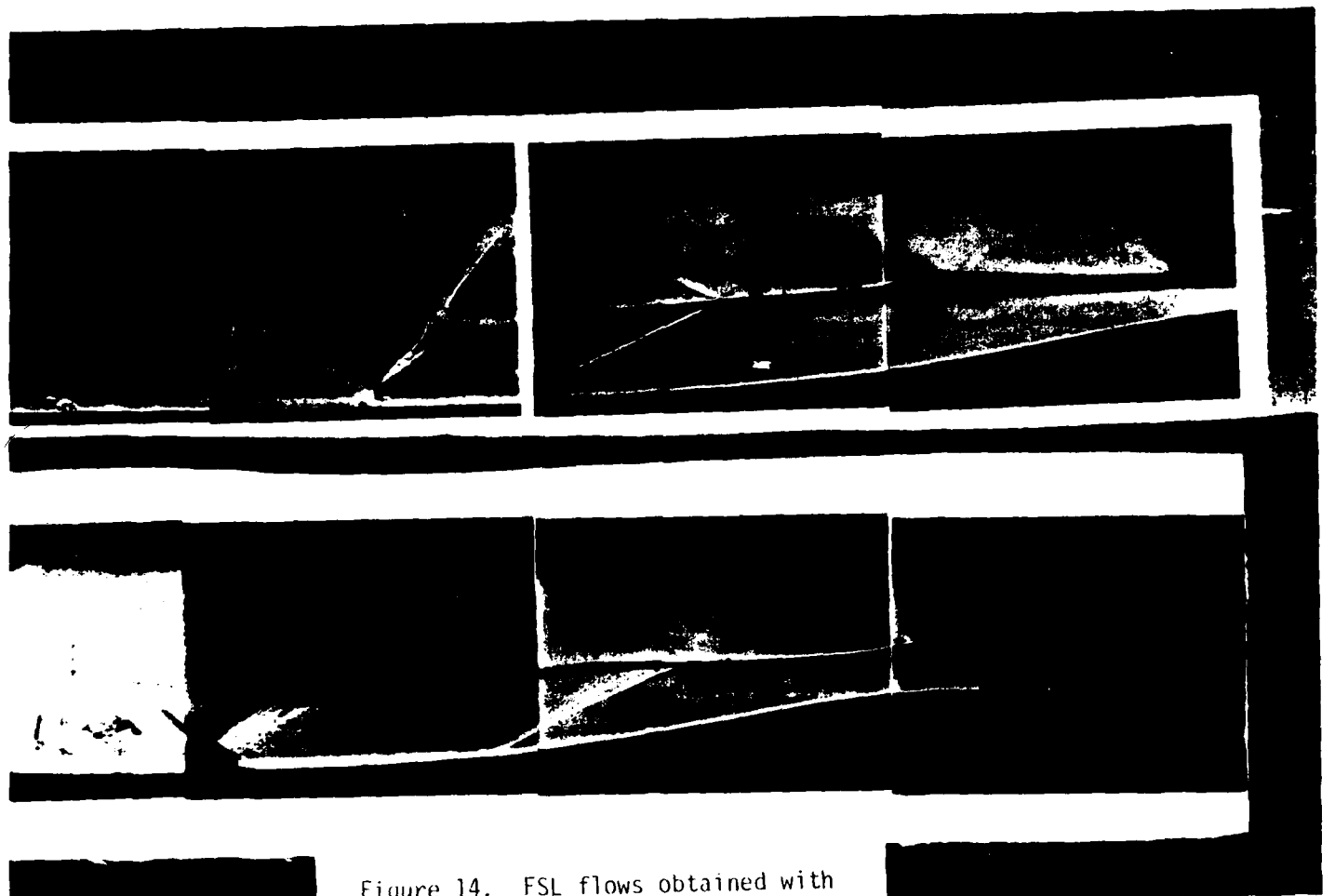

Figure 14. FSL flows obtained with the Mode I, II set-up.

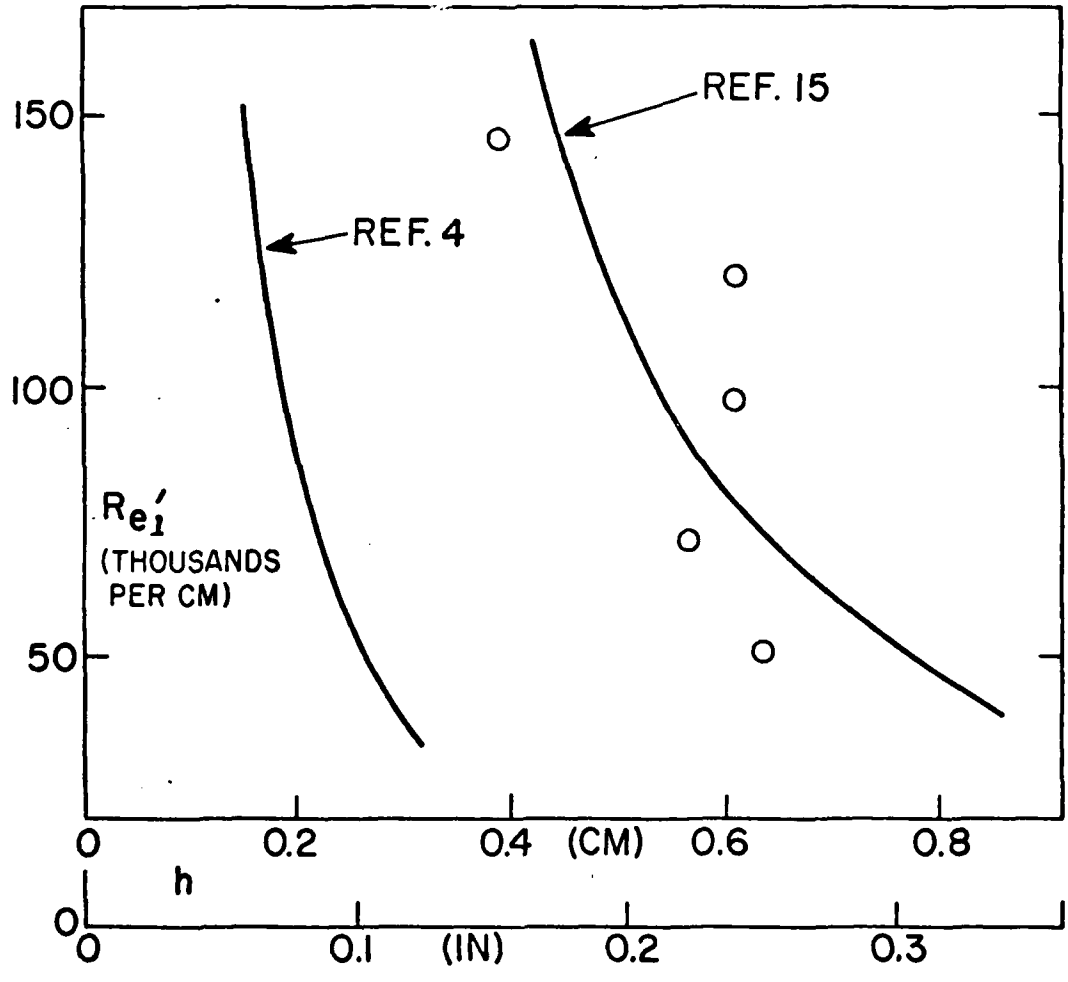


Figure 15. Comparison of preliminary FSL data with expectations.

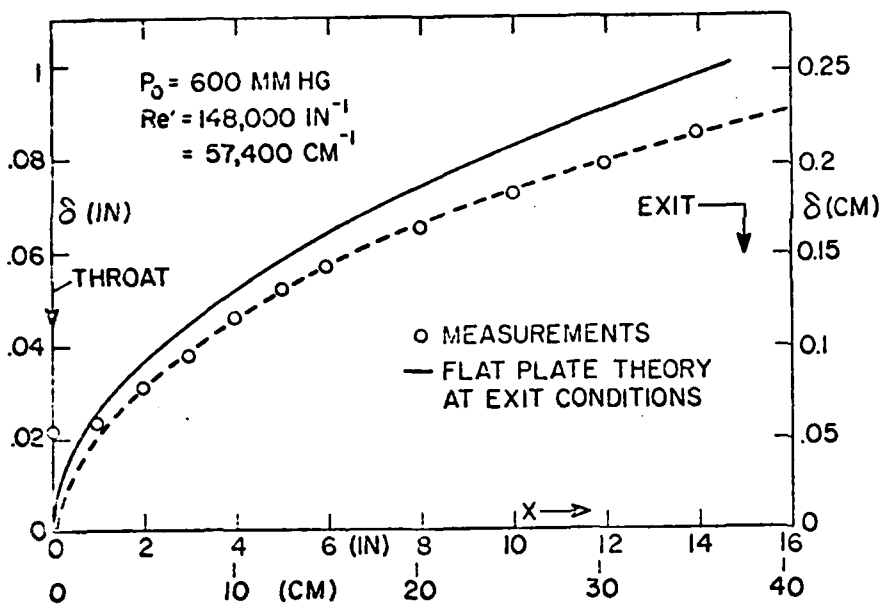


Figure 16. Boundary-layer growth in the SWT Mach 3 nozzle.

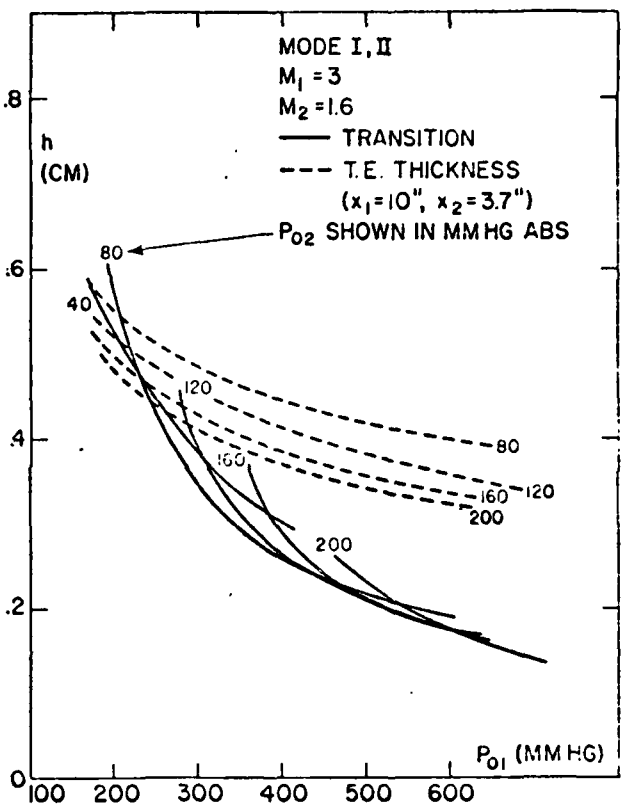


Figure 17. Working diagram for Mode I, II test design.

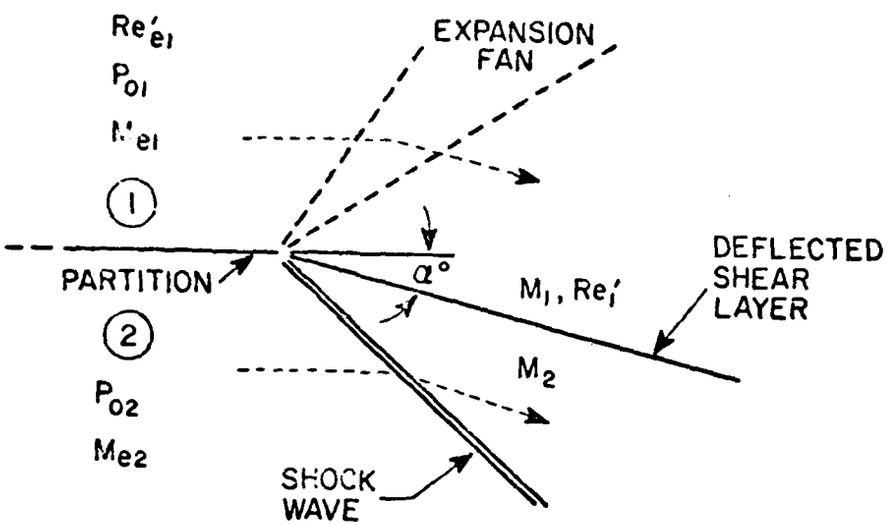


Figure 18. Nomenclature for FSL deflecting due to unmatched $p_0$'s.

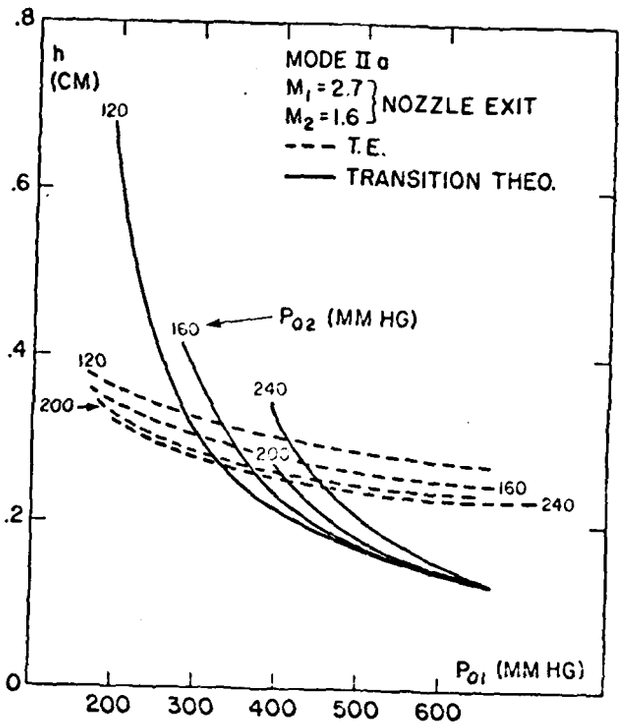


Figure 19. Working diagram for Mode IIa test design.

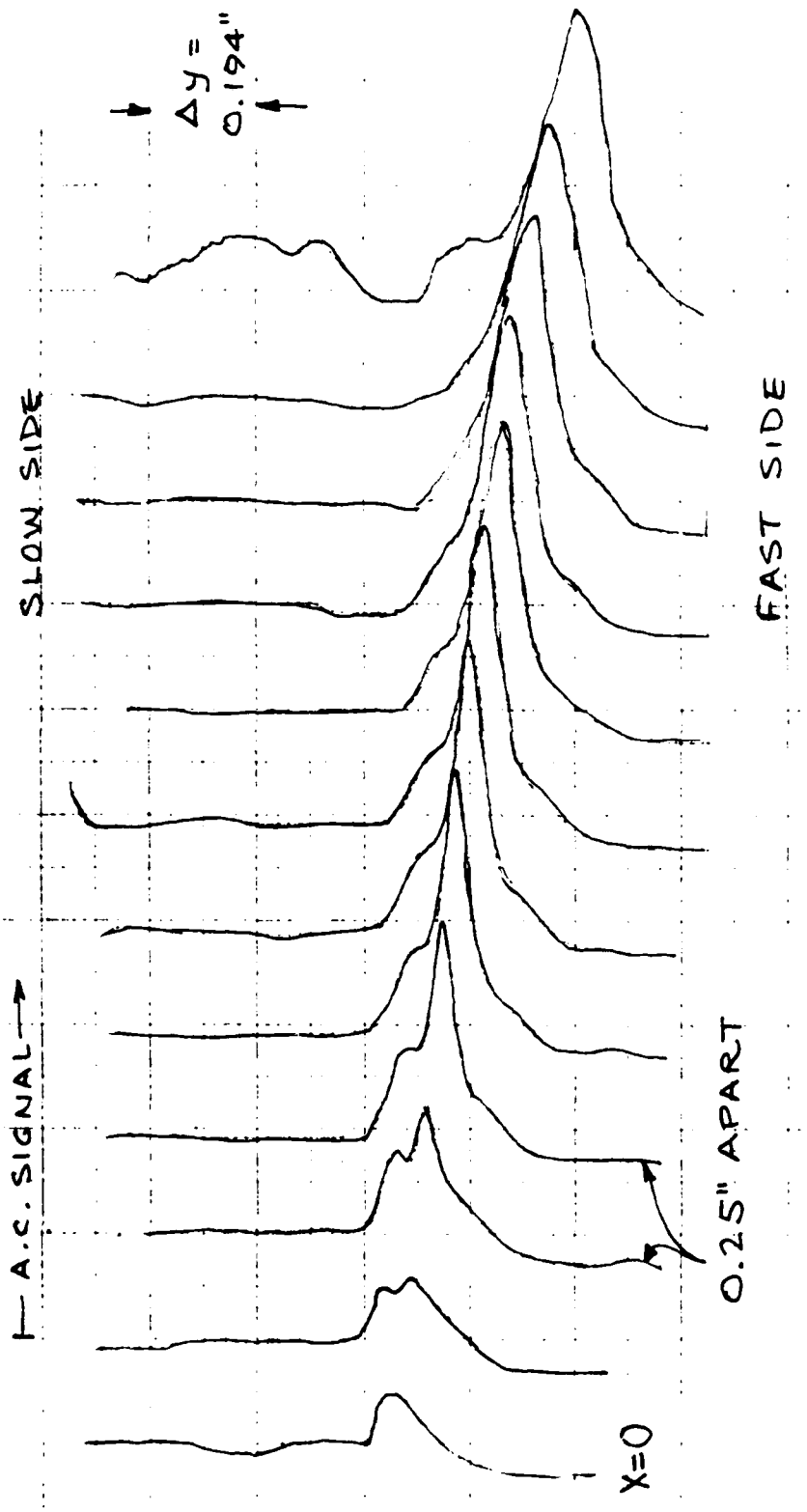


Figure 20. Wideband signals (typical) for Mode I, II FSL.

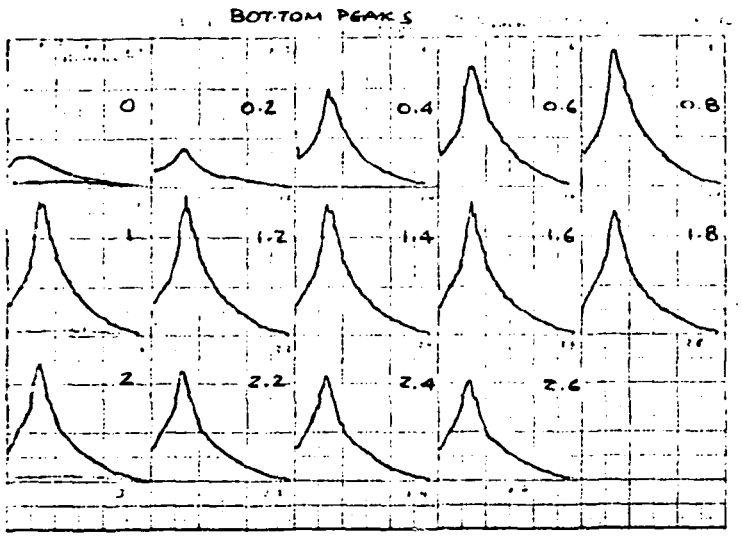


Figure 21. Power spectra on high-speed side of Mode I, II FSL.

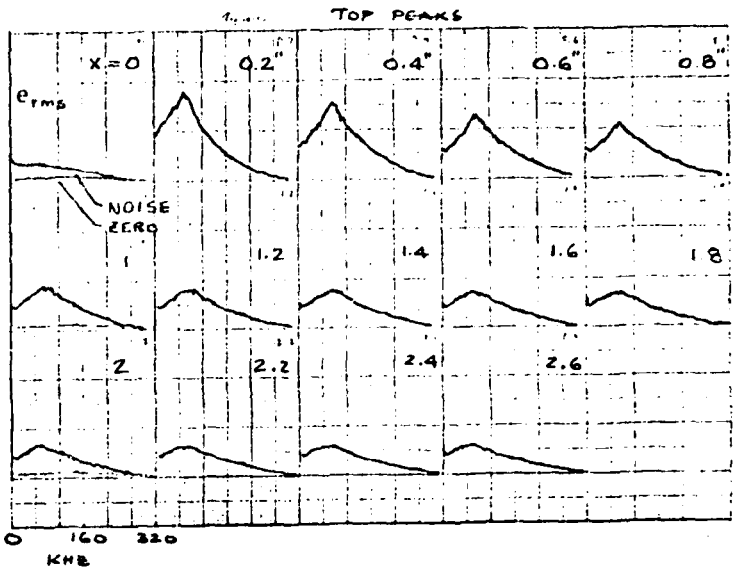


Figure 22. Power spectra on low-speed side of Mode I, II FSL.

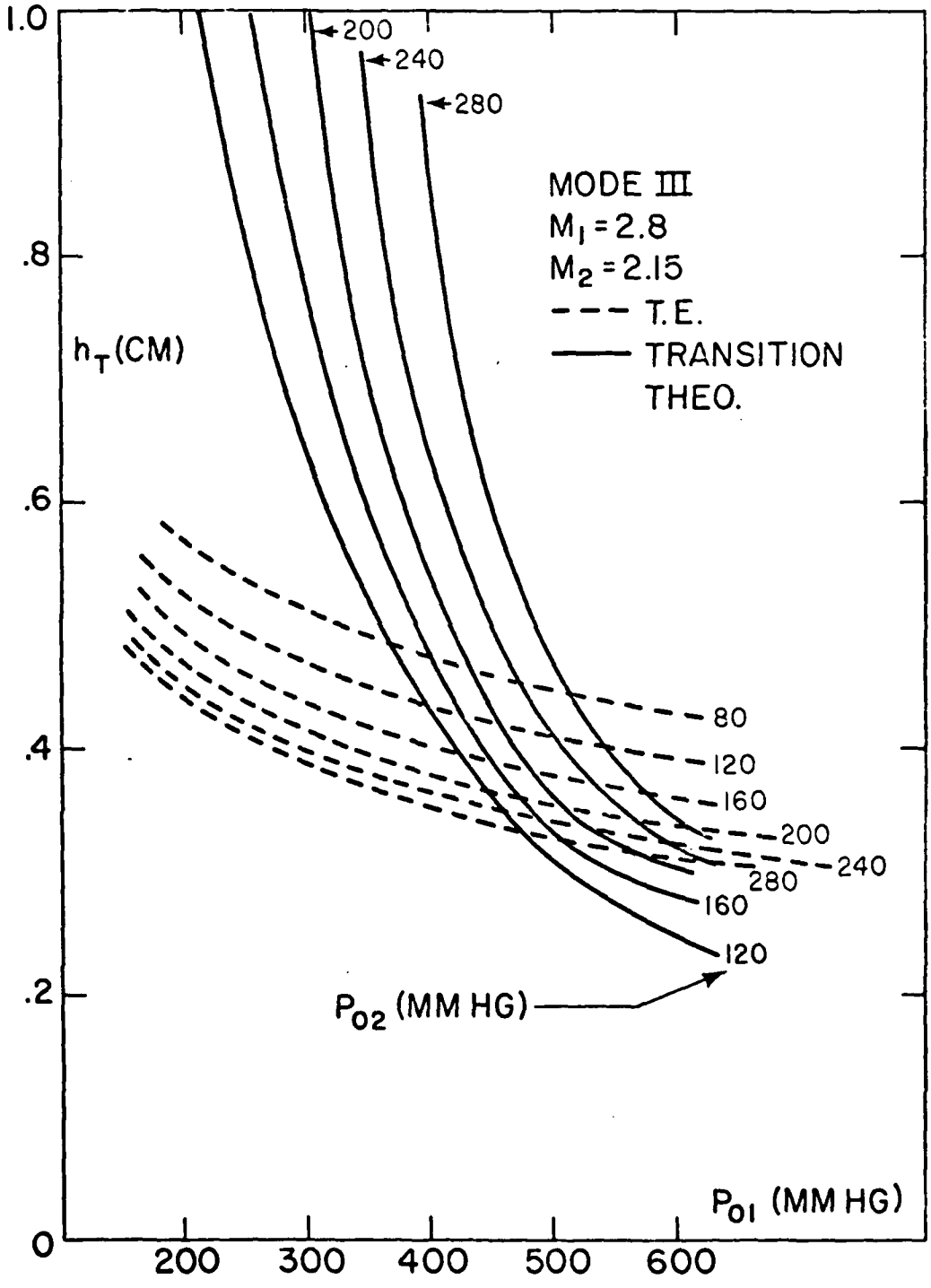


Figure 23. Working diagram for Mode III test design.

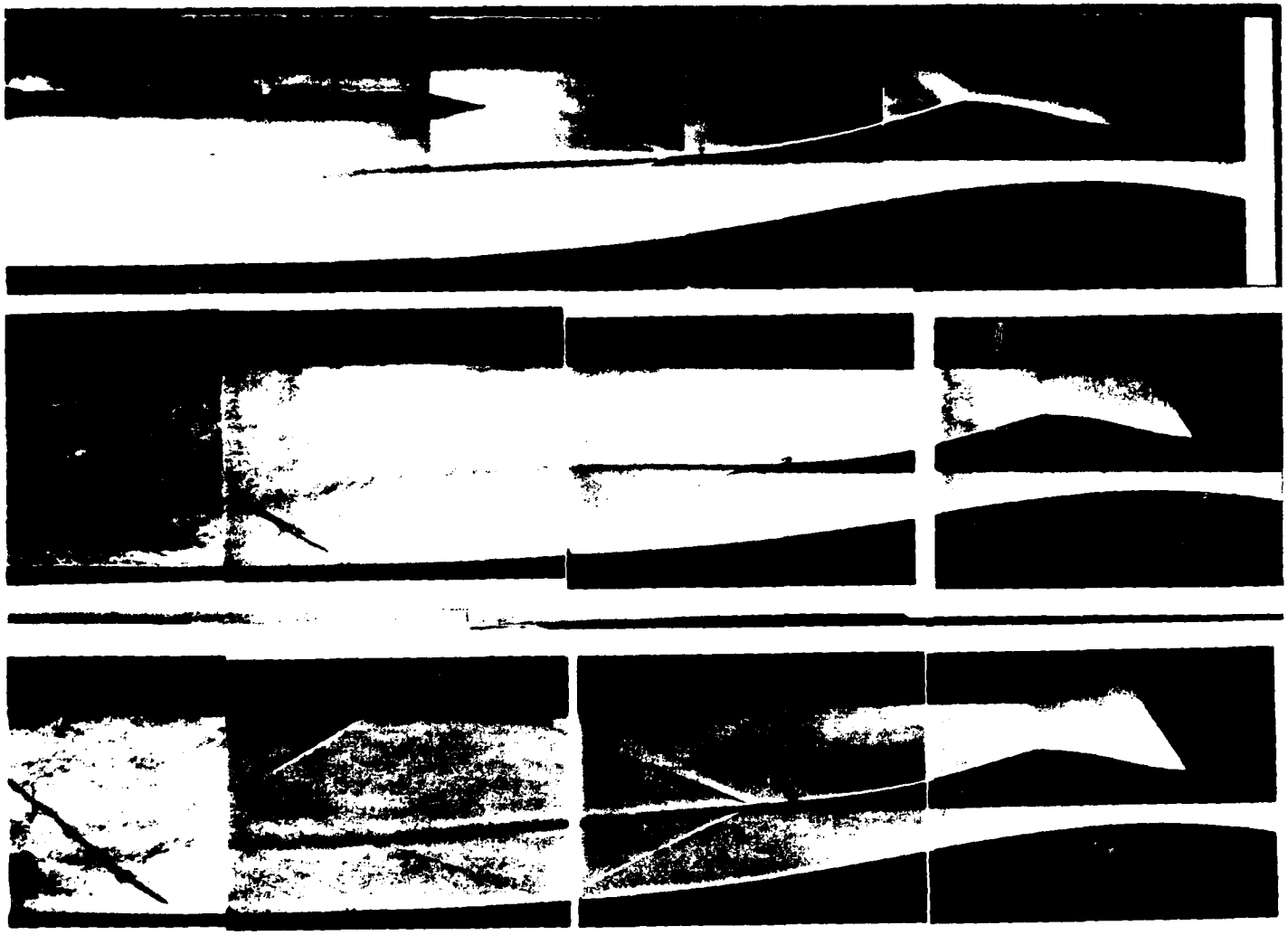

Figure 24. Continuous (top) and spark (middle and bottom) Schlieren photos of the Mode III flow. Spark photo conditions are $T_o$=100 F, $p_{o1}$=600 mm Hg.,and $p_{o2}$=187 (middle) and 286 (bottom) mm Hg.

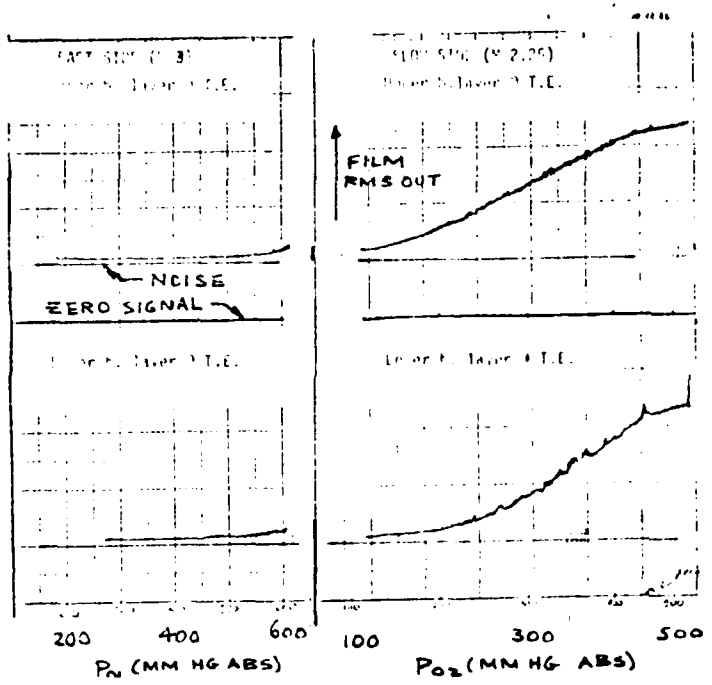


Figure 25. Hot-film anemometer signals at the T.E. of both nozzles.

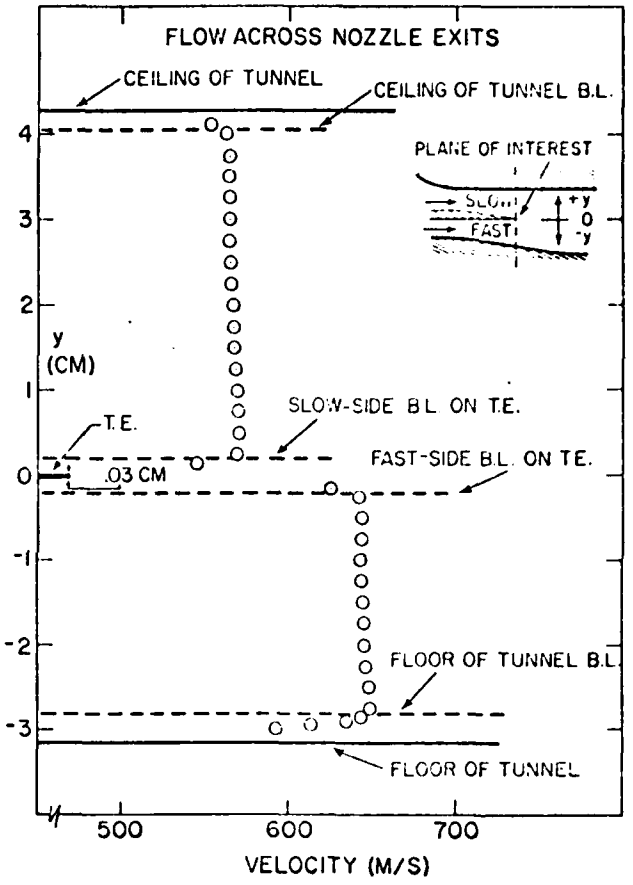


Figure 26. Velocity distribution in the exit plane of both nozzles.

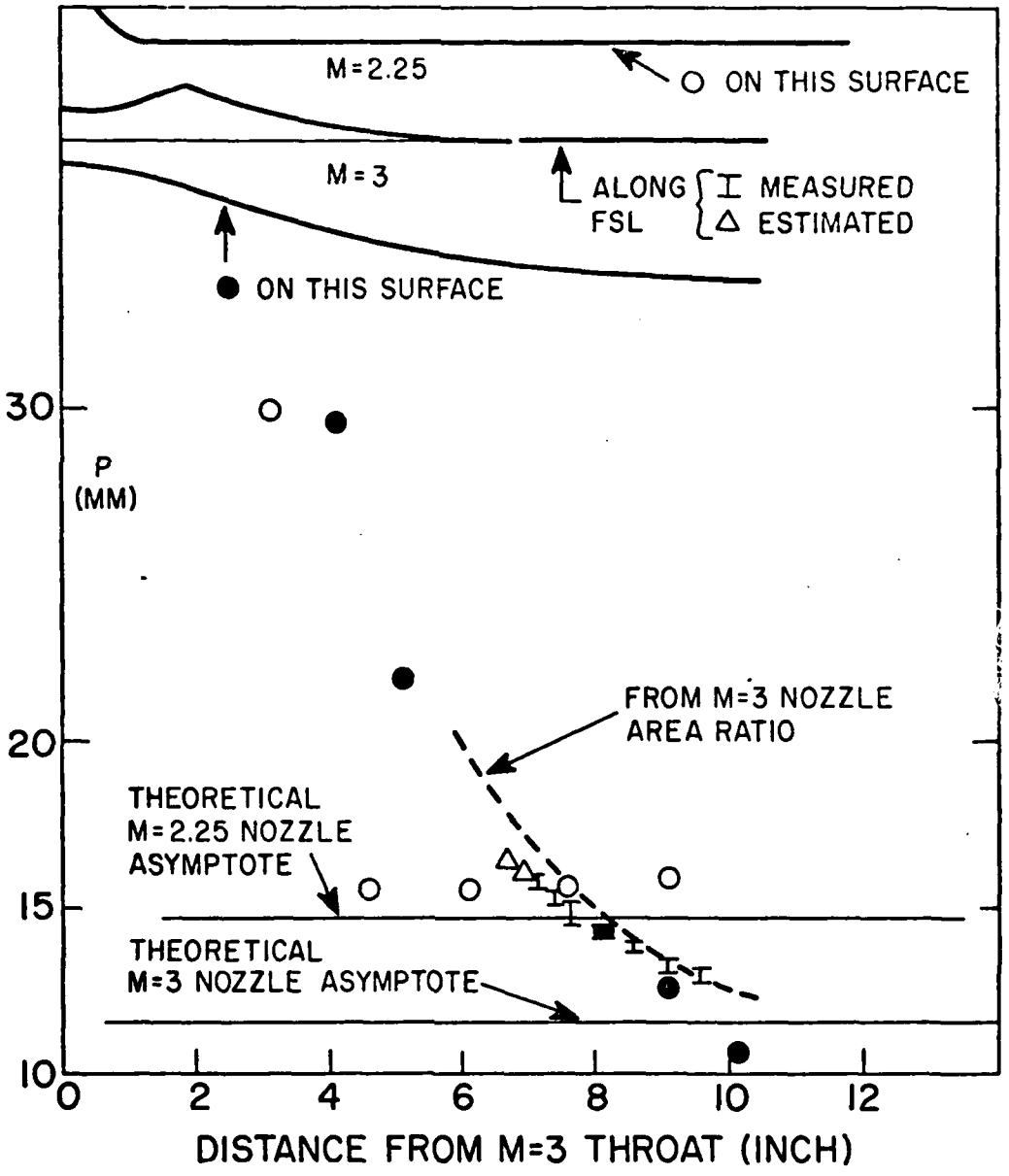


Figure 27. Pressure distribution in the nozzle exit region.

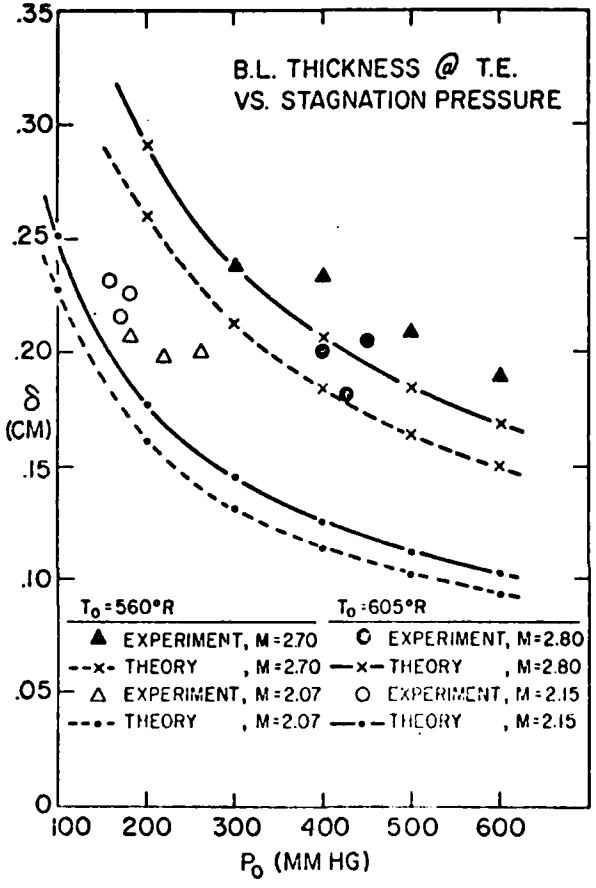


Figure 28. Boundary layer thicknesses on either side of the T.E.

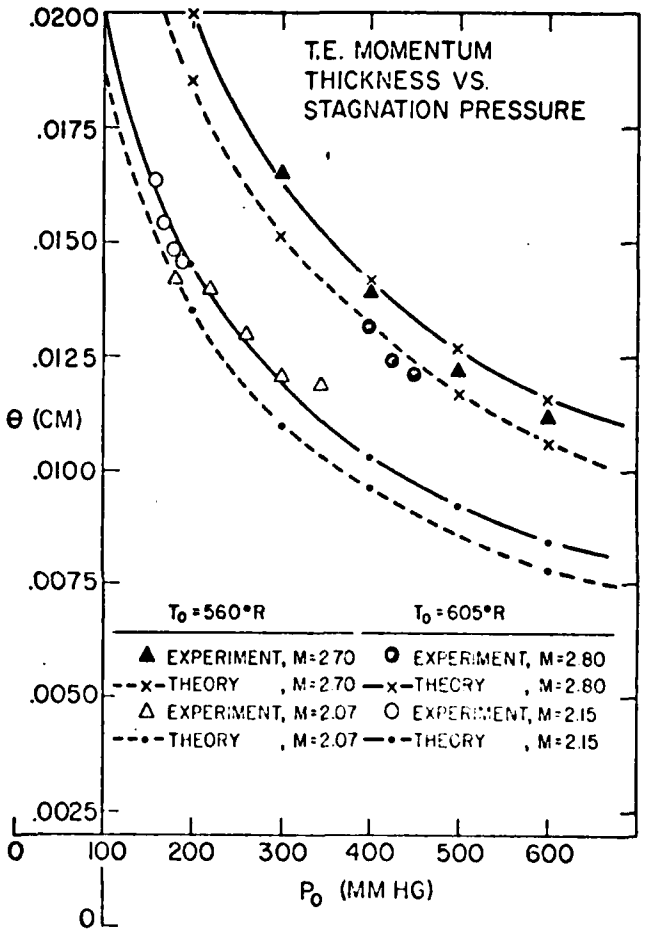


Figure 29. Momentum thicknesses on either side of the T.E.

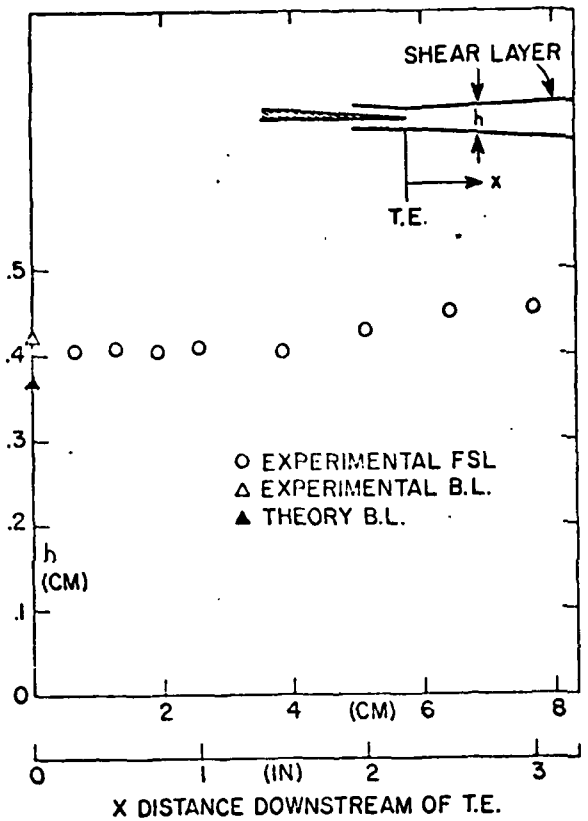


Figure 30. FSL thickness growth for Mode III experiments.

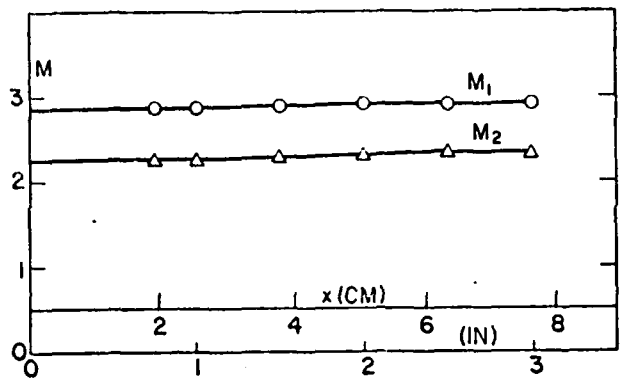


Figure 31. Mach number variations along FSL edges.

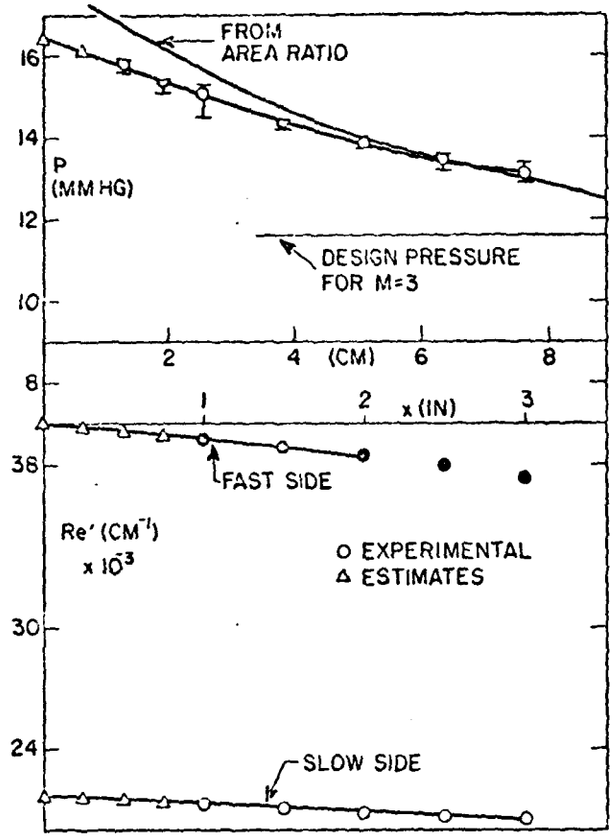


Figure 32. Pressure (top) and unit Reynolds number (bottom) along the FSL.

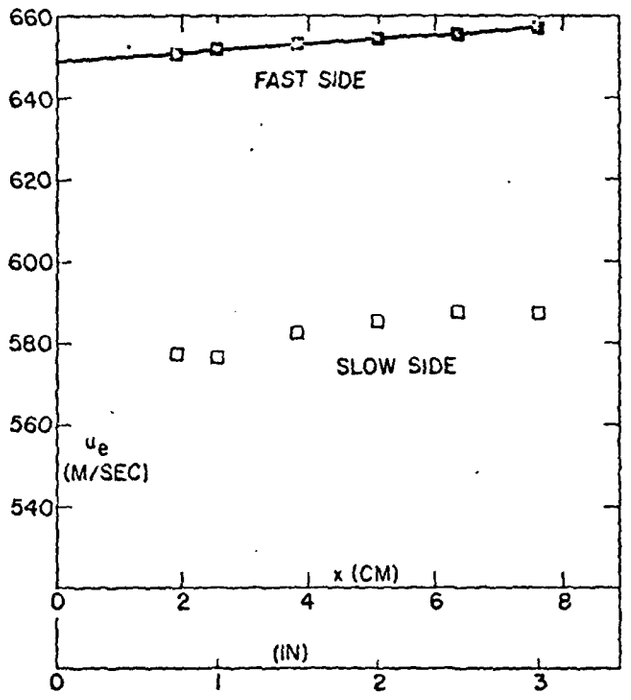


Figure 33. Velocity variation along the edge of the FSL.

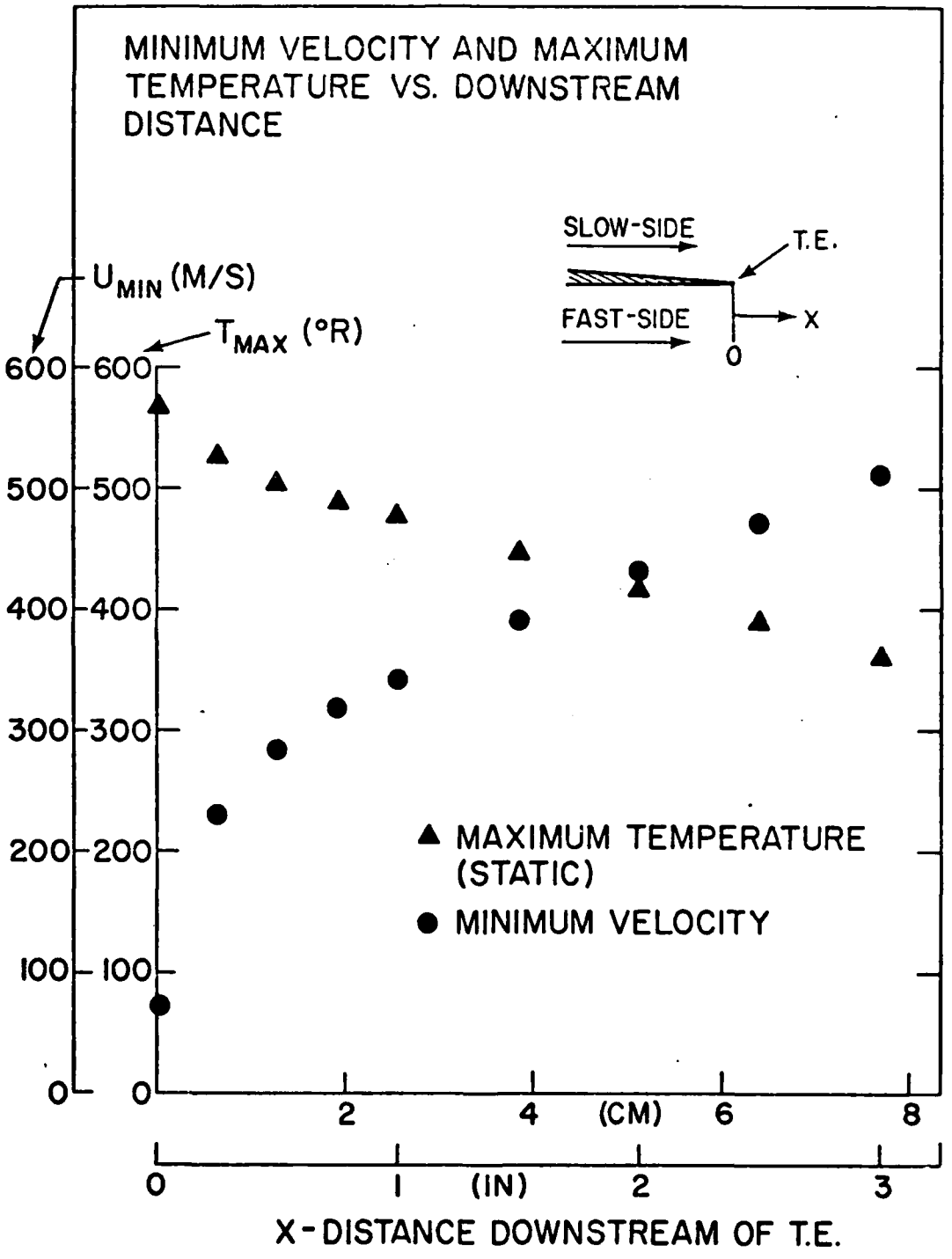


Figure 34. Center-plane velocity and temperature changes, Mode III.

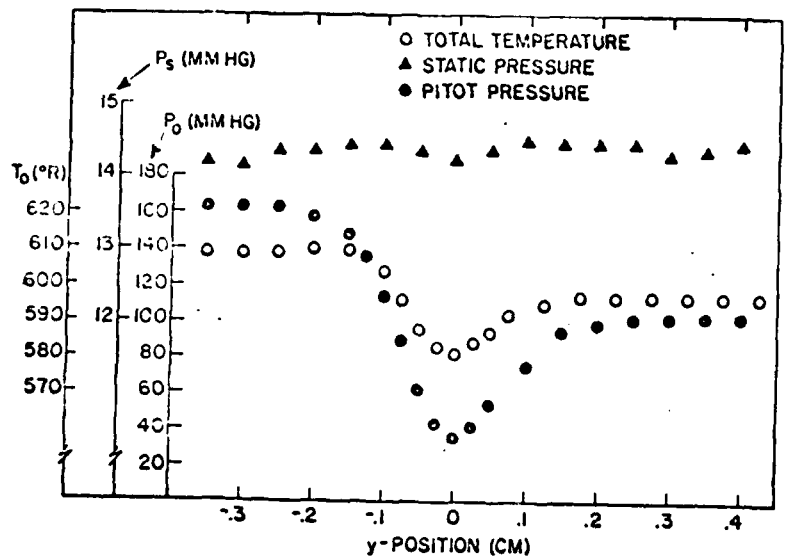


Figure 35. Typical pressure, pitot and $T_0$ profiles across the Mode III FSL.

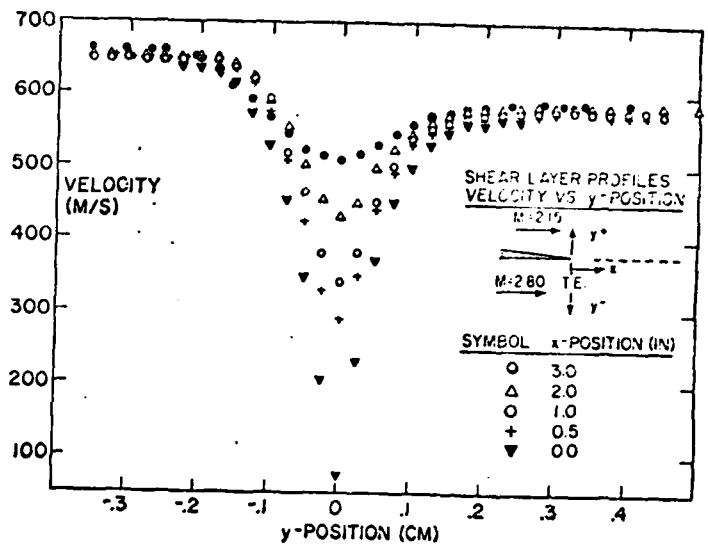


Figure 36. Velocity profiles across the Mode III FSL.

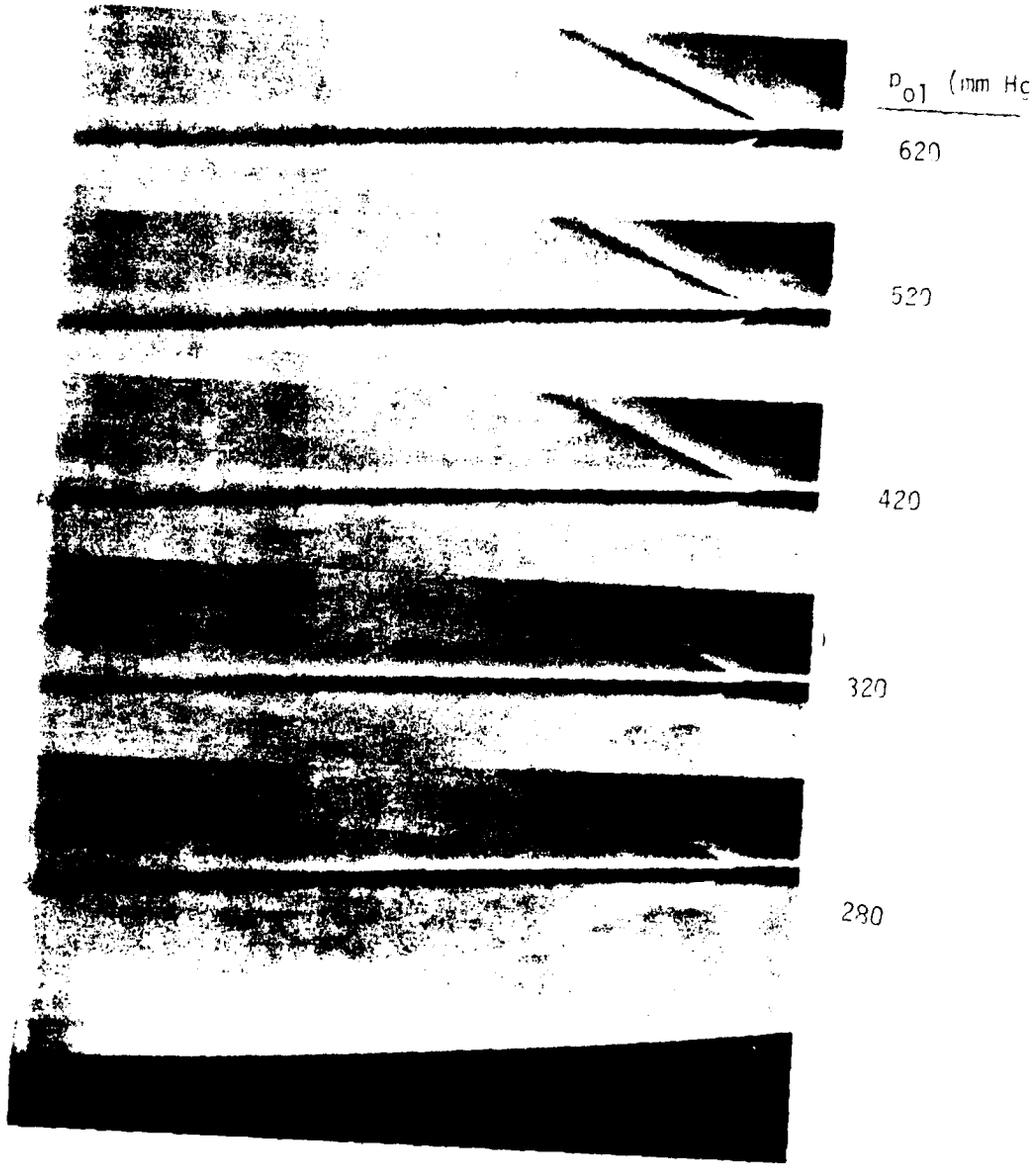


Figure 37. Continuous-exposure Schlieren photos of the FSL.

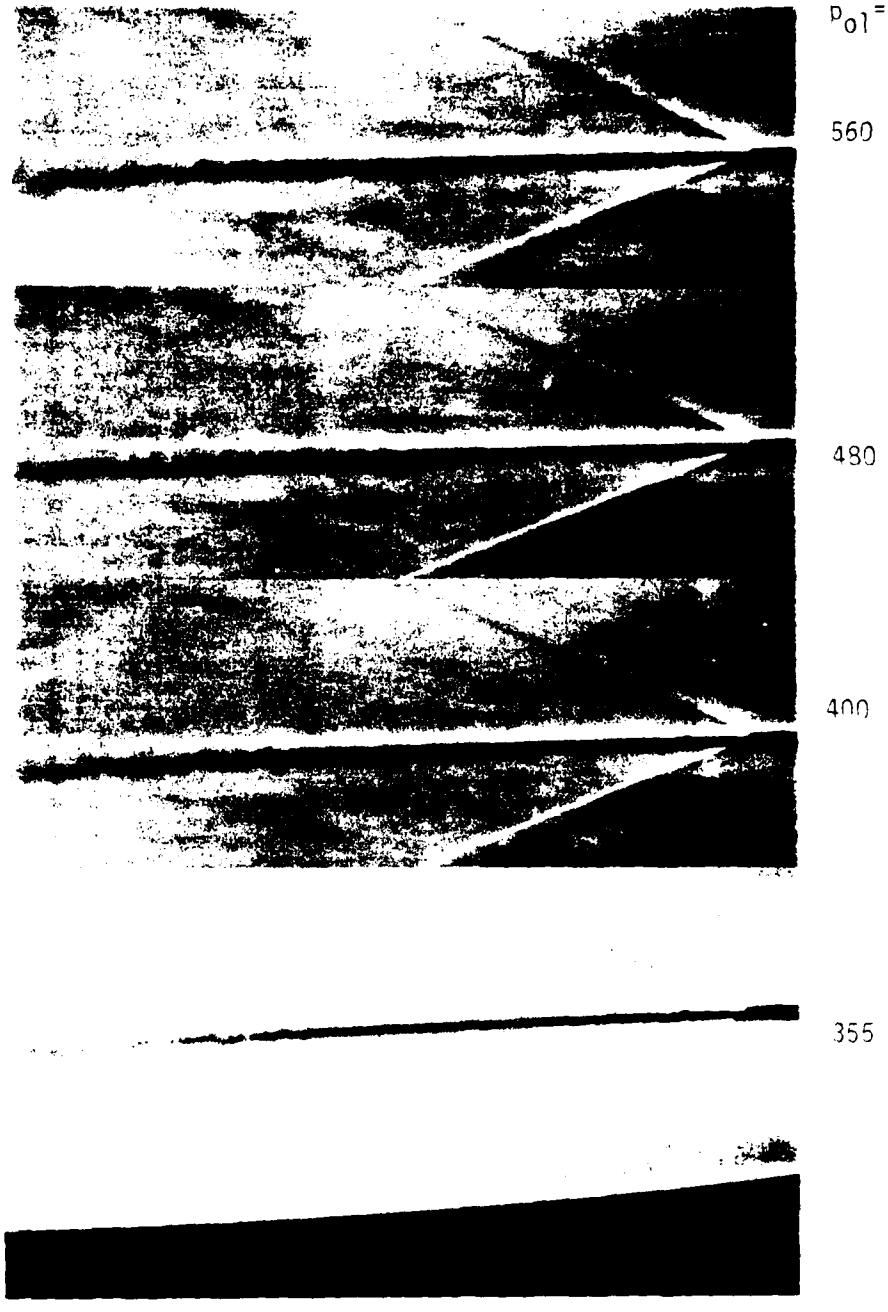


Figure 38. Spark Schlieren photos of the FSL.

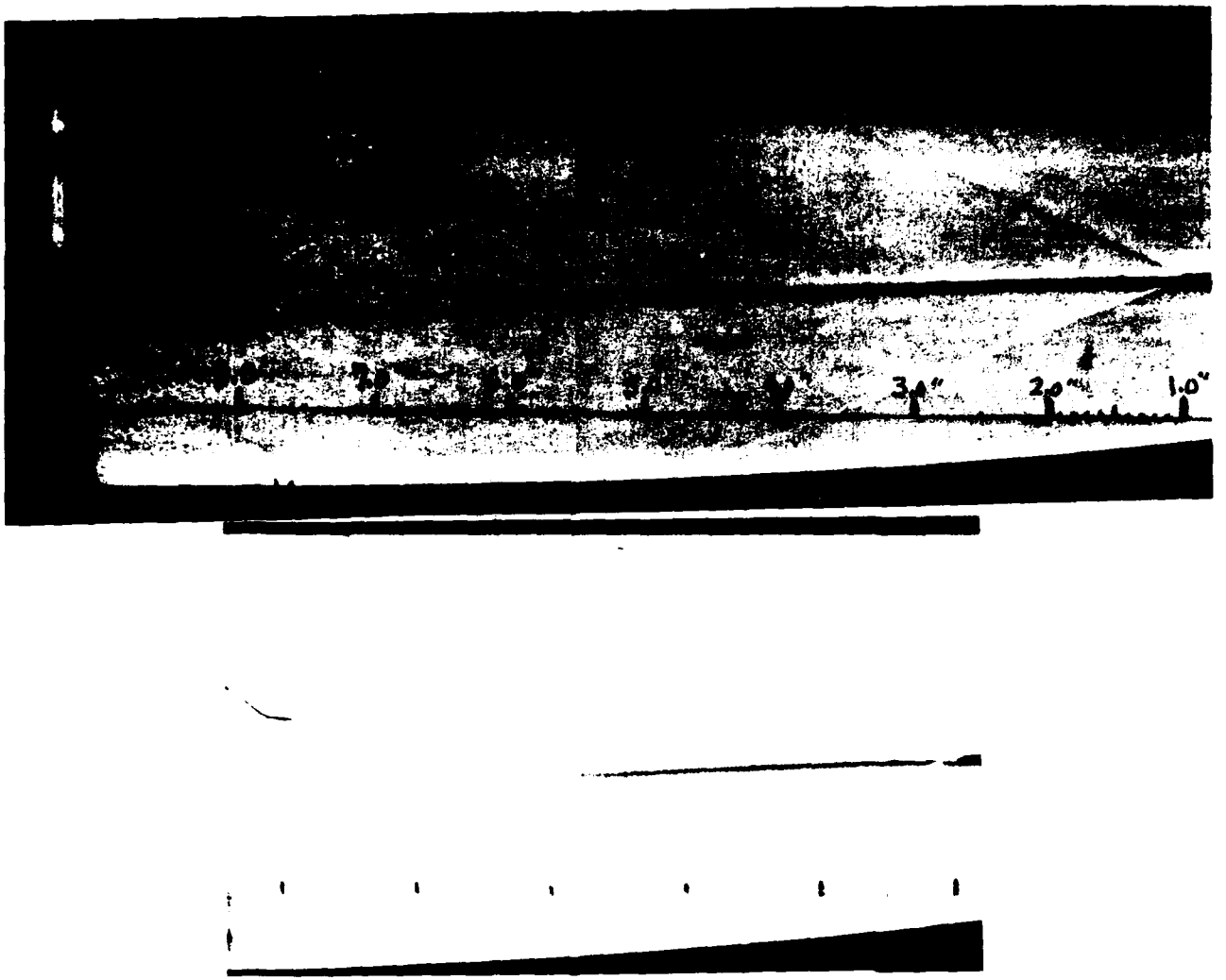


Figure 39. The Mode III FSL under continuous (top) and spark (bottom) Schlieren photography.

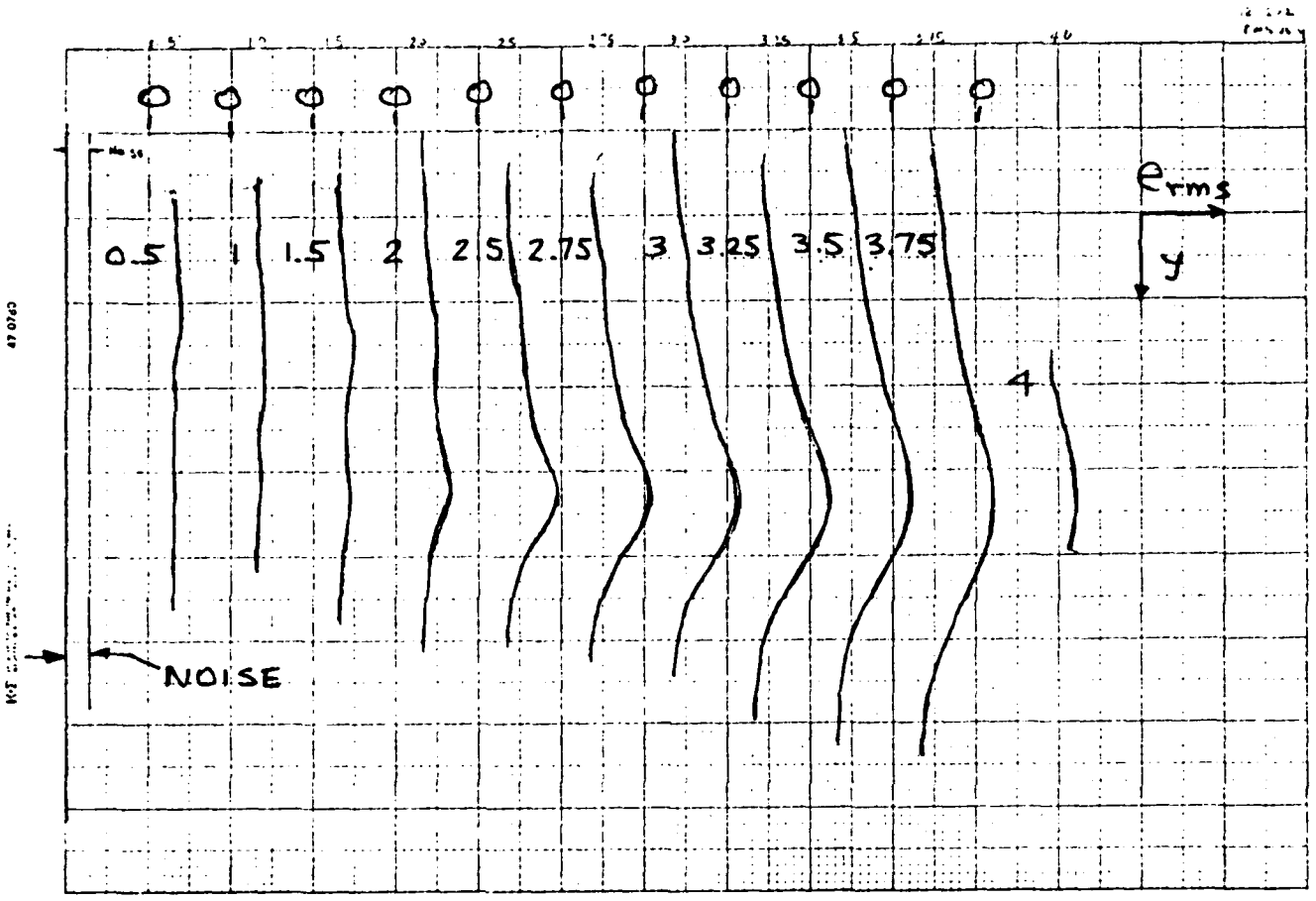


Figure 40. Wideband hot-film output in the Mode III FSL.

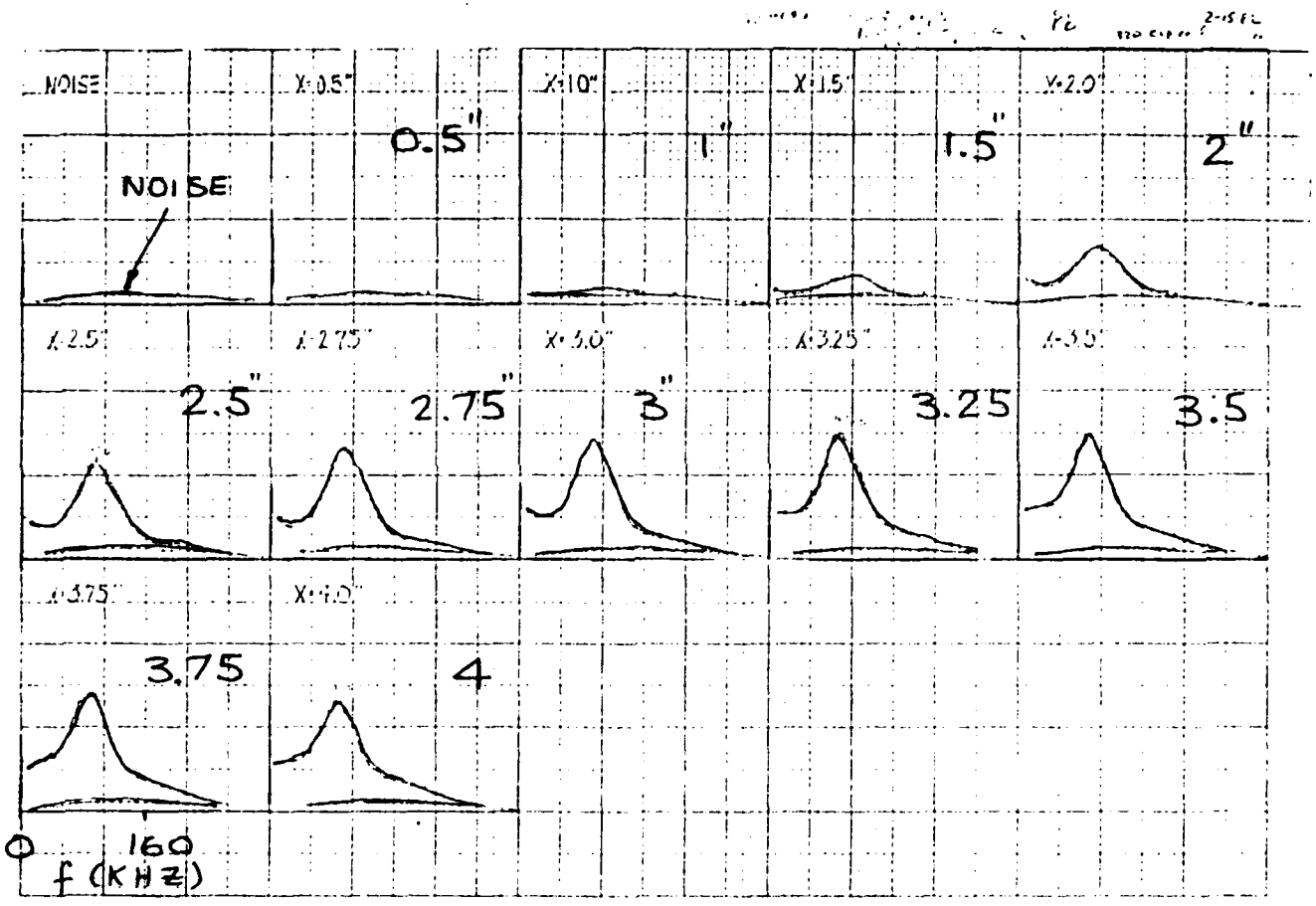


Figure 41. Spectra of the hot-film output in the Mode III FSL.

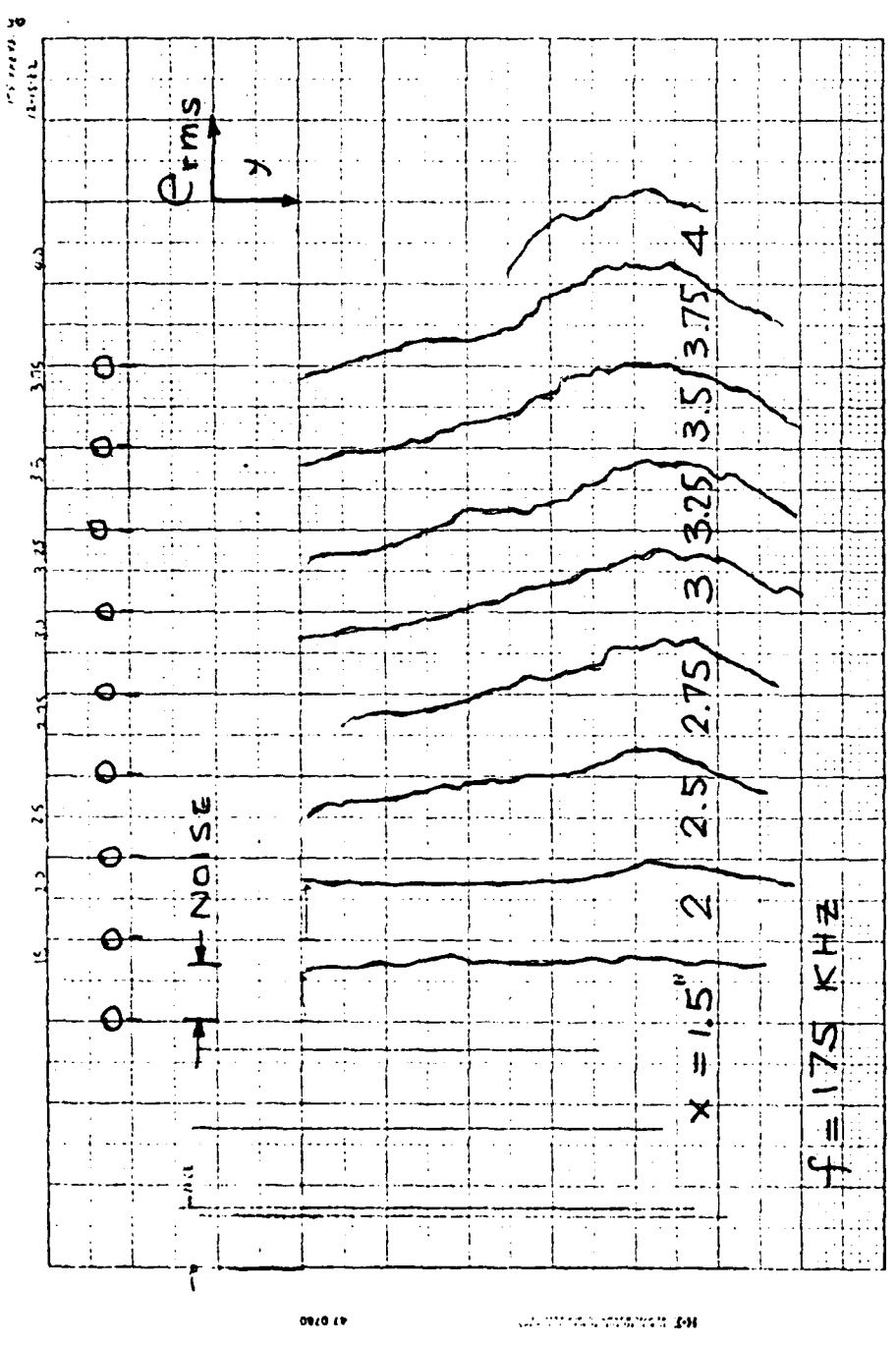


Figure 42. The hot-film output at f = 175 khz across the FSL.

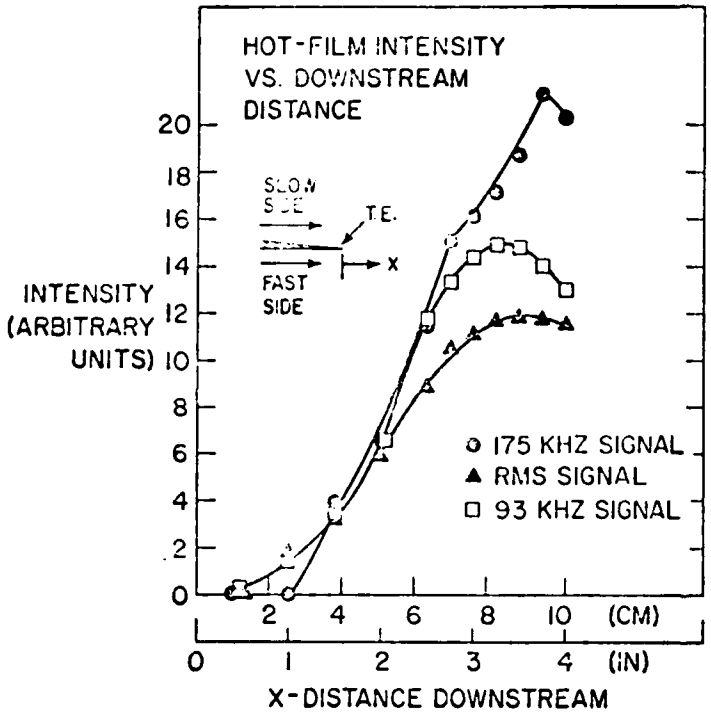


Figure 43. Streamwise variation of the hot-film signals.

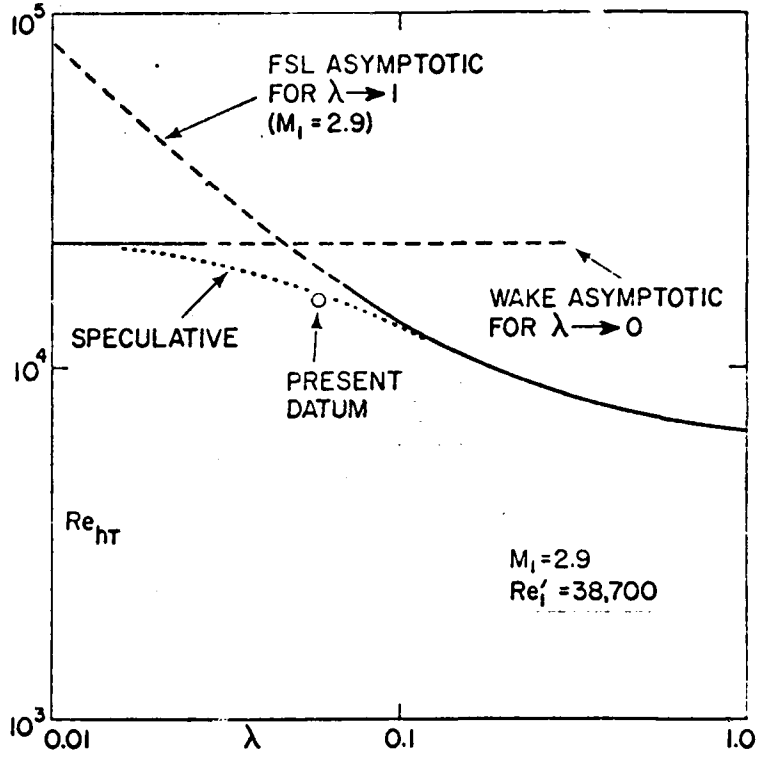


Figure 44. Measured transition point in the Mode III FSL.

# APPENDIX A

# THE LAMINAR SHEAR LAYER STARTING AT THE TRAILING EDGE

## 1. Summary

A theoretical solution is presented of the two-dimensional laminar shear layer beginning at the trailing edge of a partition separating two homogeneous, steady but dissimilar parallel flows. Dissimilarity applies not only to the stream velocities and temperatures but also to the initial boundary layer thicknesses. The validity region of the solution extends from, to infinite distances downstream of, the trailing edge.

## 2. Introduction

The gas-dynamic and chemical laser technology has motivated a fresh look at laminar free shear layers (FSL) shed of the trailing edge (T.E.) of partitions separating parallel flows. As posed, the problem usually addresses supersonic flows, usually in the range $2 < M < 6$. Furthermore, the technology requirements focus on characteristic wetted lengths which are too small for turbulent flows; the surface boundary layers are therefore most likely laminar as is the resulting initial FSL. Figure A.1 sketches the flow profiles one intuitively expects to see downstream of the partition T.E. For simplicity the partition is assumed infinitely thin, and the flows homogeneous (chemically identical and inert), steady and laminar.

Subscripts 1 and 2 on Figure A.1 refer to the fast and slow stream sides ($u_1 > u_2$) respectively. The flow properties u, M, $T_0$ etc. are allowed to differ between the two sides. Differences are also allowed in the initial boundary layer thicknesses $\delta$ and $\theta$. The problem posed is the prediction of the profiles of u, T, $\rho$ etc. as a function of x* and y* (the physical longitudinal and lateral distances) or their non-dimensional counterparts.

The cusp-like initial flow profile at the T.E., predictable from laminar boundary layer theory, will eventually become the familiar FSL profile far from the trailing edge. This asymptotic behavior is due to the inevitable diffusion of the "wake component" caused by the boundary layer flow on the partition. Because of its invariability with x, the final profile is here termed the "equilibrium" profile; the term "non-equilibrium" is used to denote the zone between the T.E. and the equilibrium zone, where the wake component is visible and/or dominant. The laminar non-equilibrium zone is addressed here because of its potential importance to mixing, stability and transition.

While the equilibrium-zone profiles have attracted much successful theoretical study, there is a surprising shortage of analytical attention to the non-equilibrium flow. This is perhaps due to the conviction that solutions can be obtained numerically. Much more useful however would be an analytic solution in closed form, without restrictions on the range of x, and capable of handling the full range of compressibility ($0 < M < \infty$), asymmetry ($\theta_1 \neq \theta_2$, $u_1 \neq u_2$) and heat transfer ($T_{O_1} \neq T_{O_2}$) conditions. Such a solution is presented below.

Method of Analysis

The task involved is to obtain a closed-form, analytic expression for the entire flow field of Figure A.1, complete with compressibility, heat transfer ($T_{O_1} \neq T_{O_2}$) and arbitrary values of

To offset the magnitude of the task, the pressure is assumed everywhere constant. Also, it is clear that the precise shape of the initial boundary layer profile will be insignificant to the downstream flow.

Two earlier approaches to this problem deserve mention, both addressing "base flow" problem (r=0) in vogue in the 1960's. Dennison and Baum (Reference A.1) found a numerical solution, which is presumably exact. Kubota and Dewey (Reference A.2) approached the same problem with the momentum-integral method; the main disadvantage of this method (also used subsequently by Ortwerth and Moeny (Reference A.3) as a solution for cases

with $r \neq 0$) is the existence of discontinuities in the flow profiles. Both the Dennison-Baum and Kubota-Dewey solutions demonstrated agreement with the large-x FSL profile of Chapman (Reference A.4). The Dennison-Baum and Chapman solutions will be of further use here, the latter as a direct input to the present theory, and the former as a gage of its validity.

The present scheme is based on the possibility of superposing linear flow fields, and in broad outline follows this procedure: it is recognized that the flow at hand consists of two separate components, the wake flow generated by the two merging boundary layers on one hand, and the usual FSL profile joining the two parallel streams on the other. The shear-layer component can be visualized as starting at the T.E. and it, of course, dominates the flow at far downstream distances. The wake component is most visible at and shortly downstream of the T.E., but it has little presence far downstream because of lateral diffusion. The analysis then consists of the linear addition of the two flow fields, that is of following the wake component as it develops on a "baseline" contorted to conform to the shear-layer component.

The idea promoting the above method comes, essentially, from experimental observations dealing with wakes growing in non-uniform flows. In low-speed flows Eskinazi (Reference A.5) showed that the turbulent wake of a cylinder growing across a pipe-flow profile was not affected by lateral velocity gradients. Kubota and McCarthy, using the laminar wake of a cylinder in hypersonic flow, actually demonstrated that laminar wake similarity was found when the laterally non-uniform flow-field, generated by the bow shock, was "subtracted out" (Reference A.6). Motivated by this finding, the present author (Reference A.7) showed that when the shear-layer component due to the supersonic inviscid flow generated by a plate at incidence was similarly "subtracted", the resulting wake profile conformed to similarity predictions.

Consider, therefore, two streams labeled 1 and 2 and pictured on Figure A.1 such that the "speed ratio" $r \equiv u_2/u_1$, flowing along $x^*$, where $x^* = 0$ at the T.E. (starred quantities are physical) and use the notation

$y'$ to signify the compressible-transformed coordinate $\tilde{y}$ divided by the total momentum thickness:

$$y' \equiv \frac{\tilde{y}^*}{\Theta} = \frac{\tilde{y}^*}{\theta_1+\theta_2} \qquad \tilde{y}^* \equiv \int_0^{y^*} \frac{\rho}{\rho_e}\, dy^* \tag{A.1}$$

Then the wake component of the velocity:

$$\bar{u} \equiv 1 - \frac{u}{u_e} = \bar{u}(x', y'; P) \tag{A.2}$$

$$P \equiv \frac{\theta_1}{\theta_2}, \quad x' \equiv \frac{x^*}{\Theta Re_\Theta}, \quad Re_\Theta \equiv \frac{u_e \Theta}{\nu_e} \tag{A.3}$$

where "e" is used to signify the "external" or "baseline" stream. Also consider the shear layer between the two streams,

$$u_s \equiv \frac{u}{u_1} = u_s(x', y'; r) \tag{A.4}$$

so that the combined velocity field will contain the characteristic asymmetry parameters r and P of its two individual components:

$$u = u(\bar{u}, u_s) = u(x', y'; P, r) \tag{A.5}$$

The two components will be briefly discussed below.

## 4. The Wake Component

The wake velocity field for arbitrary P has already been provided by this author (References A.8 and A.9). The solution is analytic, straightforward and simple:

$$\bar{u} \equiv 1 - \frac{u}{u_e} = \frac{1}{2}\left[ e^{(P+1)^2 x' + (P+1)y'} \left(1 - Erf\left((P+1)\sqrt{x'} + \frac{y'}{2\sqrt{x'}}\right)\right) + e^{\left(\frac{P+1}{P}\right)^2 x' - \frac{P+1}{P} y'} \left(1 + Erf\left(\frac{y'}{2\sqrt{x'}} - \frac{P+1}{P}\sqrt{x'}\right)\right)\right] \tag{A.6}$$

This solution is based on assumed exponential boundary layer profiles and utilizes an Oseen-type linearization (Reference A.10). However, the solution obeys all the required initial and boundary conditions, and agrees very

well with Goldstein's implicit wake solutions for P = 1 (see Reference A.11). Furthermore, the initial profile should be unimportant past the T.E. so long as the normalizing length is the total boundary-layer thickness (Reference A.8).

## 5. The Shear-Layer Component

### 5.1 Chapman's Solution

To complete the solution, the quantity $u_s$ appearing in eq. (A.4) is needed. One possibility is the solution first given by Chapman (Reference A.4) for r = 0, in the form $u/u_1$ vs the similarity variable

$$\eta' \equiv y^* \left( \frac{Re_1'}{x^*} \right)^{1/2} \tag{A.7}$$

Since $u/u_1(\eta')$ was computed by Chapman by numerical evaluation of certain integrals, it was found convenient here to approximate it by a least-squares curve-fit polynomial:

$$\frac{u}{u_1} = \sum_{n=0}^{6} C_n' \eta'^n \tag{A.8}$$

The variable $\eta'$ is related to the $x'$, $y'$ of the wake solution (eq. (A.6)) by

$$\eta' = y^* \left( \frac{Re_1'}{x^*} \right)^{\frac{1}{2}} = \left( \frac{\tilde{y}^*}{\mathcal{M}} \right) \left( \frac{\mathcal{M}^2 Re_1'}{x^*} \right)^{1/2} = \frac{y'}{\sqrt{x'}} \tag{A.9}$$

where the identity between y* and its compressible-transformed $\tilde{y}^*$ is assumed since eq. (A.8) was obtained from Chapman's incompressible (M=0) result. Furthermore, it was more convenient to replace $\eta'$ by

$$\eta \equiv \frac{y'}{2\sqrt{x'}} = \frac{\eta'}{2} \tag{A.10}$$

so that eq. (A.8) was changed to

$$\frac{u}{u_1} = \sum_{n=0}^{6} C_n \eta^n \tag{A.11}$$

with $C_0 = 0.587$, $C_1 = 0.381292$, $C_2 = 5.7138 \times 10^{-4}$, $C_3 = -5.238816 \times 10^{-2}$, $C_4 = -5.244608 \times 10^{-3}$, $C_5 = 3.465856 \times 10^{-3}$, $C_6 = 6.070848 \times 10^{-4}$. Note that eq. (A.11) is valid only in $-4 < \eta < 2.5$; if $\eta > 2.5$ then $u = u_1$, and if $\eta < -4$ then $u = 0$.

To obtain the $u_s$ quantity from eq. (A.11), for input into eq. (A.4), it was necessary to adapt Chapman's result to the case $u_2 \neq 0$, i.e. for $0 < r < 1$. Since the only relevant FSL motion is the relative one between the two streams, then Chapman's profile of eq. (A.11), originally found for $r = 0$, will give, when $r \neq 0$:

$$u_s \equiv \frac{u}{u_1} = (1-r) \sum_{0}^{6} C_n \eta^n + r \qquad (A.12)$$

which is the desired result for insertion into (A.4). The form of eq. (A.11) appears on Figure A.2.

## 5.2 Mills' Solution

A second possibility for $u_s$ is the well-known error-function formula first given by Goertler (Reference A.12):

$$u_s \equiv \frac{u'}{u_1} = \frac{1+r}{2} + \frac{1-r}{2} \operatorname{Erf} \eta \qquad (A.13)$$

where $\eta$ is the appropriate similarity variable combining the longitudinal and lateral coordinates. This solution has undergone considerable scrutiny since its inception. More recently, a series of papers by Lock (Reference A.12), Ting (Reference A.13), Crane (Reference A.14) and Mills (Reference A.15) has re-examined the problem by seeking the elusive "third boundary condition" to the equations of motion. Mills' paper, being the last in the series chronologically, reviews the issue thoroughly and arrives at a numerical method of computing the laminar shear layer for any r, $M_1$ or $T_{0_2}/T_{0_1}$. The gist of Mills' paper is that although eq. (A.13) is a good approximation to the shape of the profile, the value of $u/u_1$ needs adjustment by some function of r such that the argument of the error function is $\eta + a(r)$, where $a(r)$ is a function he tabulates. His tabulation was used to find the following curve-fit:

$$a(r) = 0.364767 - 0.0168957r - 0.740214r^2 + 0.393747r^3 \qquad (A.14)$$

Mills Furthermore expresses $\eta$ as

$$\eta = \frac{y^*}{2\sqrt{x^*}} (\overline{Re'})^{1/2} \qquad (A.15)$$

$$\overline{Re'} \equiv \frac{1}{2}(Re_1' + Re_2') = \frac{1}{2}\left(\frac{u_1}{\nu_1} + \frac{u_2}{\nu_2}\right) \qquad (A.16)$$

where Re′ is the unit Reynolds number. Equations (A.14), (A.15) and (A.16) comprise the alternative shear-layer velocity profile to be used in (A.4):

$$u_s = \frac{1+r}{2} + \frac{1-r}{2}\,\mathrm{Erf}(\eta + a(r)) \qquad (A.17)$$

Equation (A.17) is compared with Chapman's method on Figure A.2.

6. Combination of the Two Flow Components

In combining the two fields, we assume consistently with the experimental findings quoted above that

(a) The wake component develops independently of the shear component.

Equation (A.6) presents no obstacle to this proposition if the free-stream velocity $u_e$ in the definition of $\bar{u}$ is taken to be the shear velocity $u'$, except that the unit Reynolds number Re′ entering the non-dimensional coordinate x′ has to be determined. As a concession to the difference between $Re'_1$ and $Re'_2$, we further propose that

(b) The unit Reynolds number controlling the diffusion of the wake component of eq. (A.6) is the average between $Re'_1$ and $Re'_2$, as defined in (A.10).

These two propositions enable us to use the wake component as it stands in eq. (A.6) with

$$y' \equiv \frac{\tilde{y}^*}{\Theta} \quad , \quad x' \equiv \frac{x^*}{\Theta \overline{Re}_\Theta} \quad , \quad \overline{Re}_\Theta \equiv \frac{Re'_1 + Re'_2}{2}\Theta \qquad (A.18)$$

For the shear component we assume that the lateral coordinate y is replaced by its compressible-transformed counterpart $\tilde{y}$, which is hardle controversial; then the coordinate $\eta$ in (A.9) immediately becomes

$$\eta = \frac{y'}{2\sqrt{x'}} \qquad (A.19)$$

For the shear component $u_s$ we have a choice between Chapman's form (eq. (A.12)) and Mills' form (eq. (A.17)). Note that in both cases the independent variable $\eta$ is given by eq. (A.9). However, a point arises in

the physical interpretation of $\eta$ when the wake and shear-layer components are combined, as will be done below. Specifically, while proposition (b), above, applies to the wake as well as to Mills' FSL component (eq. (A.17)), it is clearly not applicable to Chapman's case when $Re_2' = 0$. For the moment we will nevertheless also assume that the Reynolds number appearing in (A.12) is the average given by (A.10) if $u_2 \neq 0$; this makes $x'$ uniform throughout.

The addition (superposition) of the two components is then explained with the aid of Figure A.3. The actual flow velocity u is related to the shear-component velocity u' by

$$u = u' - u_w \tag{A.20}$$

In ordinary wakes, the $u_w$ is usually the difference between the edge or external velocity $u_e$ and the actual velocity:

$$u_w = u_e - u = u_e \bar{u} \tag{A.21}$$

where $\bar{u}$ is already defined in eq. (A.6). The key to the present approach *is to set* $u' = u_e$, *i.e. to superpose the wake flow on a "free stream"* which is actually the shear-layer profile. Inserting $u' = u_e$ into the above two formulas,

$$u = u' - u'\bar{u} = u'(1 - \bar{u}) \tag{A.22}$$

or

$$\frac{u}{u_1} = \frac{u'}{u_1}(1 - \bar{u}) = u_s(1 - \bar{u}) \tag{A.23}$$

with $u_s$ supplied by (A.12) or (A.17) and $\bar{u}$ by (A.6). Thus,

$$\frac{u}{u_1} = \frac{u}{u_1}(x', y'; r, P) \tag{A.24}$$

The thermodynamic variables can then be obtained with the aid of the Crocco relation:

$$\frac{T}{T_1} - 1 = \frac{\gamma-1}{2} M_1^2 \left[1 - \left(\frac{u}{u_1}\right)^2\right] + \left[\frac{1 - (T_2/T_1)}{1 - (u_2/u_1)} + \frac{\gamma-1}{2} M_1^2 \left(1 + \frac{u_2}{u_1}\right)\right]\left(\frac{u}{u_1} - 1\right) \tag{A.25}$$

from which the temperature ratio is

$$\frac{T}{T_1} = \frac{T}{T_1}(x', y'; r, P; M_1, T_{02}/T_{01}) \tag{A.26}$$

Once the temperature ratio is known, the remaining thermodynamic parameters can be calculated easily.

## 7. Illustration and Discussion of the Solutions

### 7.1 Computation Method

Three simple BASIC language problems have been written to compute the flow according to eq. (A.23). Program SHEAR4 requires inputs of P, r, $M_1$, $T_{O_2}/T_{O_1}$, and $x'$ and produces profiles of temperature, velocity etc. as a function of $y'$ (the required $y'$ interval is an input). This program uses Mills' shear Layer Model, eq. (A.17). Program SHEAR5 requires the same inputs, and produces only profiles vs. $y'$. These profiles are of the (a) Mills' FSL component from eq. (A.17), (b) the complete flow from eq. (A.23) using Mills' $u_s$, (c) the Chapman FSL component from eq. (A.12), and (d) the complete flow from eq. (A.23) using Chapman's component. Finally, program SHEAR6 computes properties only along the $y' = 0$ plane.

These programs are shown on Tables I, II and III.

8. Results

Computations with equations (A.12), (A.17) and (A.23) have been carried out and are shown on Figures A.4 through A.10. Typical questions answered by these computations are (a) how does the present theories agree with other methods, (b) how do results using Mills' $u_s$ differ from those using Chapman's $u_s$, (c) how is the "regular" FSL profile get distorted, and for how long, by the shed boundary layers?

(a) Comparison with other theories is made difficult by the absence of parallel methods addressing the issue as widely as done here. A good test can, however, be made in the case of r = 0, i.e. the "base flow" problem addressed by Kubota and Dewey and by Dennison and Baum. Figure A.5 shows the quantity $u/u_1$ ($y' = 0$) for this case. The agreement of the present method (using Chapman's $u_s$) with the Dennison-Baum (exact) solution is very good, and certainly better than Kubota and Dewey found by the momentum-integral method. Note that the present theory is much easier to apply than either of these other two methods.

(b) Differences in the results are found, throughout the attached Figures, between results obtained with Mills' $u_s$ and those found by Chapman's $u_s$. In general, the Chapman approach gives lower velocities. The difference tends to disappear when r is close to unity, however (e.g. compare Figure A.8 with Figure A.9).

(c) Whether the flow profile "looks like a shear layer" or a "wake" can be directly seen from eq. (A.23) where the influence of the wake component appears as the factor $(1 - \bar{u})$. For example if we require that the regular FSL profile $u_s$ is not distorted by more than, say, 5%, we find the $x'$ at which $\bar{u}$ has decreased to 0.05 on the axis. It turns out that this distance is very long, of order $x' = 100$. Maximum $x'$ attainable in laser cavities is of order 1-10, and thus it follows the laminar FSL's in such cavities require consideration of the wake component as done herein. Note that the influence of the wake component cannot be always gaged by the presence or absence of the "trough" or "bucket" in the flow center. For

example, Figure A.10 shows that by $x' = 0.1$ the trough has been "smeared out" by the flow and yet the flow velocity is, in places, half of what it would be without the initial boundary layers.

## REFERENCES


A.1 Denison, M.R. and Baum, E.: "Compressible Free Shear Layer With Finite Initial Thickness", AIAA J. vol.1, No. 2, Feb. 1963, p. 342.

A.2 Kubota, T. and Dewey, C.F. Jr.: "Momentum Integral Methods For The Laminar Free Shear Layer", AIAA J. vol.2, No. 4, Apr. 1964, p. 625.

A.3 Moeny, W. and Ortwerth, P.J. Private comm., 1980-82.

A.4 Champan, D.R.: "Laminar Mixing of A Compressible Fluid", NASA TR958, 1950.

A.5 Eskinazi, S.: "Mixing of Wakes In Turbulent Shear Flow", NASA TN-83, 1959.

A.6 Kubota T. and McCarthy, J.F. Jr.: "A Study of Wakes Behind a Circular Cylinder at M = 5.7", AIAA J. vol. 2, No. 4, April 1964, p. 629.

A.7 Demetriades, A.: "Compressible Wake of Two-Deimensional Bodies at Incidence", Aeronutronic Report UG-4870, Newport Beach, Ca., October 1970.

A.8 Demetriades, A.: "The Compressible Laminar Two-Dimensional Wake With Arbitrary Initial Asymmetry", MSU SWT/TR 81-3, Montana State University, Bozeman, Mt., July 1981.

A.9 Demetriades, A.: "The Two-Dimensional Laminar Wake With and Without Initial Asymmetry", accepted for publication in the AIAA J., 1982.

A.10 Gold, H.: "Laminar Wake With Arbitrary Initial Profiles", AIAA J., vol. 2, No. 5, May 1964, p. 948.

A.11 Goldstein, S.: "On the Two-Dimensional Steady Flow of a Viscous Fluid Behind a Solid Body, parts I, II", Proc. of the Royal Society, London, Series A, vol. 142, p. 545,563 (1933).

A.12 Goertler, H.: "Berechnung von Aufgaben der freien turbulenz auf Grund eines neuen Naherungarsatzes", ZAMM vol. 22, 1942, p. 244.

A.13 Lock, R.C.: Quarterly Journal of Mechanics and Applied Mathematics, vol. 4, 1951, p. 42.

A.14 Ting, L.: J. of Mathematical Physics, vol. 38, 1959, p. 153.

A.15 Crane, L.J.: "The Laminar and Turbulent Mixing of Jets of Compressible Fluids", JFM vol. 3, 1957, p. 81.

A.16 Mills, R.D.: "Numerical and Experimental Investigations of the Shear Layer Between Two Parallel Streams", JFM vol. 33, part 3, 1968, p. 591.

# TABLE IA. THE SHEAR4 PROGRAM

```
REM SHEAR4
DIM X(50),Y(50),Z(50),E1(50),F1(50),X2(50),D(50),E2(50)
DIM F2(50),G(50),H(50),G(50),J(50),K(50),C1(50)
DIM A(5),T3(50),T4(50),M(50)
LET A=.2
LET A=.7
LET P=1
LET R=1.7#A
PRINT
PRINT
PRINT
PRINT "SHEAR4"
PRINT "SHEAR LAYER PROPERTIES FOR ARBITRARY P,R,M1 AND T02/T01"
PRINT "WITH REYNOLDS NO. AVERAGED BETWEEN THE TWO STREAMS."
PRINT "(SHEAR LAYER COMPONENT U1 according to MILLS)"
PRINT "------------------------------------------------"
PRINT
INPUT "INPUT PARAMETERS:"
PRINT
INPUT "PRESSURE THICKNESS RATIO P=";P1
PRINT "STAGNATION RATIO U2/U1=";R
PRINT "FREE-STREAM MACH NO. M1=";M
PRINT "TOTAL TEMPERATURE RATIO T02/T01=";T
S1=.26478
S2=-.01284
S3=-.78
S4=.2
S5=.03
A1=.46+S1*A+S2*(A^2)+S4*(A^3)
PRINT
PRINT "                    COMPUTED A=";A
PRINT "                    X=";X
PRINT
LET F=.22591
M1=.54
A2=-.0
A1=1.4
A3=-1.4
A4=.5
PRINT "Y","U/U1","T/T1","RHO/RHO1","M"
PRINT
FOR Y=2 TO 2 STEP .2
LET X1=(P1+1)*SQR(X))+Y/(2*SQR(X))
IF X1<0 GOTO 370
LET Z=(1+P*X)
LET E1=A1*Z+A2*(Z^2)+A3*(Z^3)+A4*(Z^4)+A5*(Z^5))*EXP(-(X1^2))
GOTO 410
LET X1=((P1+1)/P1)*SQR(X)-Y/(2*SQR(X))
LET Z=(1+P*X)
LET E2=A1*Z+A2*(Z^2)+A3*(Z^3)+A4*(Z^4)+A5*(Z^5))*EXP(-(X1^2))
410 LET X2=(Y/(2*SQR(X)))-((P1+1)/P1)*SQR(X)
420 IF X2<0 GOTO 460
470 LET D=1/(1+P*X2)
440 LET F2=D*(A1*D+A2*(D^2)+A3*(D^3)+A4*(D^4)+A5*(D^5))*EXP(-(X2^2))
450 GOTO 490
460 LET X2=((P1+1)/P1)*SQR(X)-(Y/(2*SQR(X)))
470 LET D=1/(1+P*X2)
480 LET F2=D*(A1*D+A2*(D^2)+A3*(D^3)+A4*(D^4)+A5*(D^5))*EXP(-(X2^2))
490 LET F2=F2*((((P1+1)/P1)^2)*X+((P1+1)/P1)*Y)*E2
500 LET G=1/(F1+F2)
510 LET H=Y/(2*SQR(X))
520 LET J=H*G
530 IF J<0 GOTO 570
540 LET J=1/(1+F*J)
550 LET J=1*(A1*J+A2*(J^2)+A3*(J^3)+A4*(J^4)+A5*(J^5))*EXP(-(J^2))
560 GOTO 610
570 LET J=-H*G
580 LET J=1/(1+F*J)
590 LET J=1*(A1*J+A2*(J^2)+A3*(J^3)+A4*(J^4)+A5*(J^5))*EXP(-(J^2))
600 LET U1=((1+R)/2)-((1-R)/2)*J
610 GOTO 670
620 LET U1=((1+R)/2)-((1-R)/2)*J
630 LET T1=1+(.2*M^2)*(1-U1^2)
640 LET T=T1/M^2
650 LET U2=U1*(1-U)
660 LET T2=1+F*(1-(U2^2))
670 LET T3=((1-T1)/(1+F+F*(1+F)))*(U2-1)
680 LET T4=T2+T3
690 LET M=U2*M*SQR(1/T4)
700 PRINT Y,U2,T4,1/T4,M
710 NEXT Y
1000 END
```

TABLE IA. (Continued)

PRINCIPAL SHEAR4 PROGRAM GLOSSARY

| Program Symbol | First Appearing on Line Number | Is the Algebraic | Meaning |
|---|---|---|---|
| X | 20 | $X'$ | $x^*/\Theta\overline{Re_\Theta}$ |
| M | 22 | $M_1$ | -- |
| T | 24 | $T_{O_2}/T_{O_1}$ | -- |
| P1 | 30 | P | $\theta_1/\theta_2$ |
| R | 40 | r | $u_2/u_1$ |
| B1....B4 | 120-150 | - | Coefficients of a(r) |
| A | 170 | a(r) | -- |
| P | 230 | n | Constant in the approximation to Erf |
| A1....A5 | 240-280 | $A_1,...A_5$ | Constants in the approximation to Erf |
| Y | 310 | $y'$ | $\tilde{y}^*/\Theta$ |
| X1 | 320 | $(p+1)\sqrt{x'} + \frac{y'}{2\sqrt{x'}}$ | |
| F1 | 400 | $X1\exp((P+1)^2x' + (P+1)y')$ | |
| X2 | 410 | $\frac{y'}{2\sqrt{x'}} - \frac{P+1}{P}\sqrt{x'}$ | Argument of 2nd Erf appearing in $\bar{u}$ |
| F2 | 490 | | Second term in $\bar{u}$ |
| U | 500 | $\bar{u}$ | Wake component of velocity |
| H | 510 | $\eta$ | $y'/2\sqrt{x'}$ |
| K | 590 | $Erf(\eta+a(r))$ | Erf in $u_s$ |
| U1 | 600 | $u_s$ | FSL component of velocity |
| U2 | 650 | $u/u_1$ | -- |
| T4 | 680 | $T/T_1$ | -- |
| M2 | 690 | M | -- |

TABLE IA. (Continued)

SHEAR4 PROGRAM LANDMARKS

| LINES | OPERATION |
|---|---|
| 120-190 | Computation of a(r), eq. (8.A) |
| 230-290 | Definition of constants in approximate formula for Erf |
| 310 | Loop start (sets y´ intervals for printout) |
| 320-390 | Computation of complementary Erf in the first $\bar{u}$ term |
| 400 | Computation of first $\bar{u}$ term |
| 420-480 | Computation of Erf in second $\bar{u}$ term |
| 500 | Final computation of $\bar{u}$ |
| 530-590 | Computation of the Erf in $u_s$ |
| 600-620 | Final computation of $u_s$ |
| 630-680 | Computation of $T/T_1$ |
| 650 | Computation of $u/u_1$ |
| 690 | Computation of M |

TABLE IA. (Continued)

ACTIVATION COMMANDS FOR

SHEAR4, -5 AND -6

| LINE | COMMAND |
|---|---|
| 20 | Enter $x'$ |
| 22 | Enter $M_1$ |
| 24 | Enter $T_{O_2}/T_{O_1}$ |
| 30 | Enter P |
| 40 | Enter r |
| 310 | Enter $y'$ range and intervals |
| 305* | Enter $x'$ range and intervals by typing in N range and intervals where $x' = 10^N$ |

* SHEAR6 only

# TABLE IIA. THE SHEAR5 PROGRAM

```
10 REM SHEAR5
12 DIM Y(50),X1(50),Z(50),E1(50),F1(50),X2(50),D(50),E2(50)
14 DIM F2(50),U(50),H(50),G(50),J(50),K(50),U1(50)
16 DIM T2(50),T3(50),T4(50),M(50)
17 DIM U3(50),U4(50)
20 LET X=.03
22 LET M=3.5
24 LET T=1
26 LET P1=10
40 LET R=.145
42 PRINT
44 PRINT
46 PRINT
48 PRINT
49 PRINT "SHEAR5"
5  PRINT "SHEAR LAYER PROPERTIES FOR ARBITRARY P,R,M1 AND T02/T01"
55 PRINT "WITH REYNOLDS NO. AVERAGED BETWEEN THE TWO STREAMS."
57 PRINT "(COMPARISON BETWEEN MILLS' AND CHAPMAN'S SHEAR LAYER COMPONENT)"
60 PRINT "-----------------------------------------------------"
70 PRINT
80 PRINT "INPUT PARAMETERS:"
90 PRINT
100 PRINT "MOMENTUM THICKNESS RATIO P=";P1
102 PRINT "SPEED RATIO U2/U1=";R
104 PRINT "FAST-SIDE MACH NO. M1=";M
110 PRINT "TOTAL TEMPERATURE RATIO T02/T01=";T
120 LET B1=.634767
130 LET B2=-.016d957
140 LET B3=-.740214
150 LET B4=.393747
161 LET C0=.587
162 LET C1=.381292
167 LET C2=5.7179E-04
174 LET C3=-.0522892
183 LET C4=-5.24461E-03
186 LET C5=7.46186E-03
187 LET C6=6.07##5E-04
189 IF R<.1 GOTO 190
191 LET A=B1+B2*R+B3*(R^2)+B4*(R^3)
192 GOTO 200
194 LET A=.355
200 PRINT "                    COMPUTED A=";A
210 PRINT "                    X'=";X
220 PRINT
230 LET P=.327591
240 LET A1=.2548295#
250 LET A2=-.2844967#
260 LET A3=1.421413741#
270 LET A4=-1.453152027#
280 LET A5=1.061405429#
290 PRINT "Y","U3(MLS)","U/U1(MLS)","U3(CHP)","U/U1(CHP)"
300 PRINT
310 FOR Y=-2 TO 2 STEP .2
320 LET X1=((P1+1)*SQR(X))+Y/(2*SQR(X))
330 IF X1<0 GOTO 370
340 LET Z=1/(1+P*X1)
350 LET E1=(A1*Z+A2*(Z^2)+A3*(Z^3)+A4*(Z^4)+A5*(Z^5))*EXP(-(X1^2))
360 GOTO 400
370 LET X1=-((P1+1)*SQR(X))-Y/(2*SQR(X))
380 LET Z=1/(1+P*X1)
390 LET E1=2-(A1*Z+A2*(Z^2)+A3*(Z^3)+A4*(Z^4)+A5*(Z^5))*EXP(-(X1^2))
400 LET F1=EXP(((P1+1)^2)*X+(P1+1)*Y)*E1
410 LET X2=((Y/(2*SQR(X)))-((P1+1)/P1))*SQR(X)
420 IF X2<0 GOTO 460
430 LET D=1/(1+P*X2)
440 LET E2=2-(A1*D+A2*(D^2)+A3*(D^3)+A4*(D^4)+A5*(D^5))*EXP(-(X2^2))
450 GOTO 490
460 LET X2=((P1+1)/P1)*SQR(X)-(Y/(2*SQR(X)))
470 LET D=1/(1+P*X2)
480 LET E2=(A1*D+A2*(D^2)+A3*(D^3)+A4*(D^4)+A5*(D^5))*EXP(-(X2^2))
490 LET F2=EXP(((P1+1)/P1)^2)*((P1+1)/P1)*Y)*E2
500 LET U=.5*(F1+F2)
510 LET H=(Y/(2*SQR(X)))
520 LET G=H+A
530 IF G<0 GOTO 570
540 LET J=1/(1+P*G)
550 LET K=1-(A1*J+A2*(J^2)+A3*(J^3)+A4*(J^4)+A5*(J^5))*EXP(-(G^2))
560 GOTO 620
570 LET G=H-A
580 LET J=1/(1+P*G)
590 LET K=1-(A1*J+A2*(J^2)+A3*(J^3)+A4*(J^4)+A5*(J^5))*EXP(-(G^2))
600 LET U1=((1+R)/2)-((1-R)/2)*K
610 GOTO 630
620 LET U1=((1+R)/2)+((1-R)/2)*K
630 LET T1=(1+.2*(M^2))*T-.2*(M^2)*(M^2)
631 IF M<2.5 GOTO 635
632 IF M<=4 GOTO 637
633 LET U3=C0+C1*M+C2*(M^2)+C3*(M^3)+C4*(M^4)+C5*(M^5)+C6*(M^6)
634 GOTO 640
635 LET U3=1
636 GOTO 640
637 LET U3=0
638 GOTO 640
640 LET F=.2*(M^2)
650 LET U2=U1*(1-U)
655 LET U4=(U3*(1-R)+R)*(1-U)
660 LET T2=1+F*(1-(U2^2))
670 LET T3=((1-T1)/(1-R)+F*(1+R))*(U2-1)
680 LET T4=T2+T3
690 LET M2=U2*M*SQR(1/T4)
700 PRINT Y,U1,U2,R+U3*(1-R),U4
710 NEXT Y
1000 END
Ok
```

```
10 REM SHEAR6
12 DIM Y(50),X1(50),Z(50),E1(50),F1(50),X2(50),D(50),E2(50)
14 DIM F2(50),U(50),M(50),G(50),J(50),K(50),U1(50)
16 DIM T2(50),T3(50),T4(50),M(50)
17 DIM U3(50),U4(50)
20 LET Y=0
22 LET M=2.7
24 LET T=1
26 LET P1=1
40 LET R=0
42 PRINT
44 PRINT
46 PRINT
48 PRINT
49 PRINT "S-SHEAR6"
50 PRINT "SHEAR LAYER PROPERTIES FOR ARBITRARY P,R,M1 AND T02/T01"
55 PRINT "WITH REYNOLDS NO. AVERAGED BETWEEN THE TWO STREAMS."
57 PRINT "(COMPARISON BETWEEN FILLS' AND CHAPMAN'S SHEAR LAYER COMPONENT)"
58 PRINT "This program computes properties only at y'=0"
60 PRINT "------------------------------------------------------"
70 PRINT
72 PRINT "INPUT PARAMETERS:"
80 PRINT
90 PRINT "PRESSURE THICKNESS RATIO P=";P1
100 PRINT "YIELD RATIO U2/U1=";R
104 PRINT "FREE-SIDE MACH NO, M1=";M
110 PRINT "TOTAL TEMPERATURE RATIO T02/T01=";T
120 LET A1=.284787
130 LET A2=-.0152957
140 LET A3=-.730214
150 LET A4=.729747
160 LET A5=-.537
170 LET B1=.731292
180 LET B2=5.71E-04
190 LET B3=-.0527302
195 LET B4=-5.24461E-03
196 LET B5=".465866E-03
197 LET B6=8.7[illegible]5E-04
198 IF M=1 GOTO 199
200 LET A=B1+B2*R+B3*(R^2)+B4*(R^3)
210 GOTO 200
[illegible]
[illegible]
220 PRINT "                    COMPUTED A=";A
230 PRINT "                    Y'=0"
[illegible]
250 LET P=.327591
260 LET P1=.254829592#
270 LET A2=-.284496736000001#
280 LET A3=1.421413741#
290 LET A4=-1.453152027#
300 LET A5=1.061405429#
310 PRINT "X","US(MLS)","U/U1(MLS)","US(CHP)","U/U1(CHP)"
320 PRINT
325 FOR N=0 TO 1 STEP .5
```

```
310 LET X=10 N
320 LET X1=((P1+1)*SQR(X))+Y/(2*SQR(X))
330 IF X1<0 GOTO 370
340 LET Z=1/(1+P*X1)
350 LET E1=(A1*Z+A2*(Z^2)+A3*(Z^3)+A4*(Z^4)+A5*(Z^5))*EXP(-(X1^2))
360 GOTO 400
370 LET X1=-((P1+1)*SQR(X))-Y/(2*SQR(X))
380 LET Z=1/(1+P*X1)
390 LET E1=2-(A1*Z+A2*(Z^2)+A3*(Z^3)+A4*(Z^4)+A5*(Z^5))*EXP(-(X1^2))
400 LET F1=EXP(((P1+1)^2)*X+(P1+1)*Y)*E1
410 LET X2=(Y/(2*SQR(X)))-((P1+1)/P1)*SQR(X)
420 IF X2<0 GOTO 460
430 LET D=1/(1+P*X2)
440 LET E2=2-(A1*D+A2*(D^2)+A3*(D^3)+A4*(D^4)+A5*(D^5))*EXP(-(X2^2))
450 GOTO 490
460 LET X2=((P1+1)/P1)*SQR(X)-(Y/(2*SQR(X)))
470 LET D=1/(1+P*X2)
480 LET E2=(A1*D+A2*(D^2)+A3*(D^3)+A4*(D^4)+A5*(D^5))*EXP(-(X2^2))
490 LET F2=EXP(((P1+1)/P1)^2)*X-((P1+1)/P1)*Y)*E2
500 LET U=.5*(F1+F2)
510 LET H=(Y/(2*SQR(X)))
520 LET G=U+A
530 IF G<0 GOTO 570
540 LET J=1/(1+P*G)
550 LET K=1-(A1*J+A2*(J^2)+A3*(J^3)+A4*(J^4)+A5*(J^5))*EXP(-(G^2))
560 GOTO 620
570 LET G=-H+A
580 LET J=1/(1+P*G)
590 LET F=1-(A1*J+A2*(J^2)+A3*(J^3)+A4*(J^4)+A5*(J^5))*EXP(-(G^2))
600 LET U1=((1+R)/2)-((1-R)/2)*K
610 GOTO 630
620 LET U1=((1+R)/2)+((1-R)/2)*K
630 LET T1=(1+.2*(M^2))*T-.2*(R^2)*(M^2)
631 IF H<5 GOTO 635
632 IF H<8 GOTO 637
633 LET U3=C0+C1*H+C2*(H^2)+C3*(H^3)+C4*(H^4)+C5*(H^5)+C6*(H^6)
634 GOTO 640
635 LET U3=1
636 GOTO 640
637 LET U3=0
638 GOTO 640
641 LET P=.2*(M^2)
650 LET U2=U1*(1-U)
655 LET U4=(U3*(1-R)+R)*(1-U)
660 LET T2=1+F*(1-(U2^2))
670 LET T3=((1-T1)/(1-R)+F*(1+R))*(U2-1)
680 LET T4=T2+T3
690 LET M2=U2*M*SQR(1/T4)
700 PRINT X,U1,U2,R+U3*(1-R),U4
710 NEXT N
1000 END
Ok
```

TABLE IIA. THE SHEAR6 PROGRAM

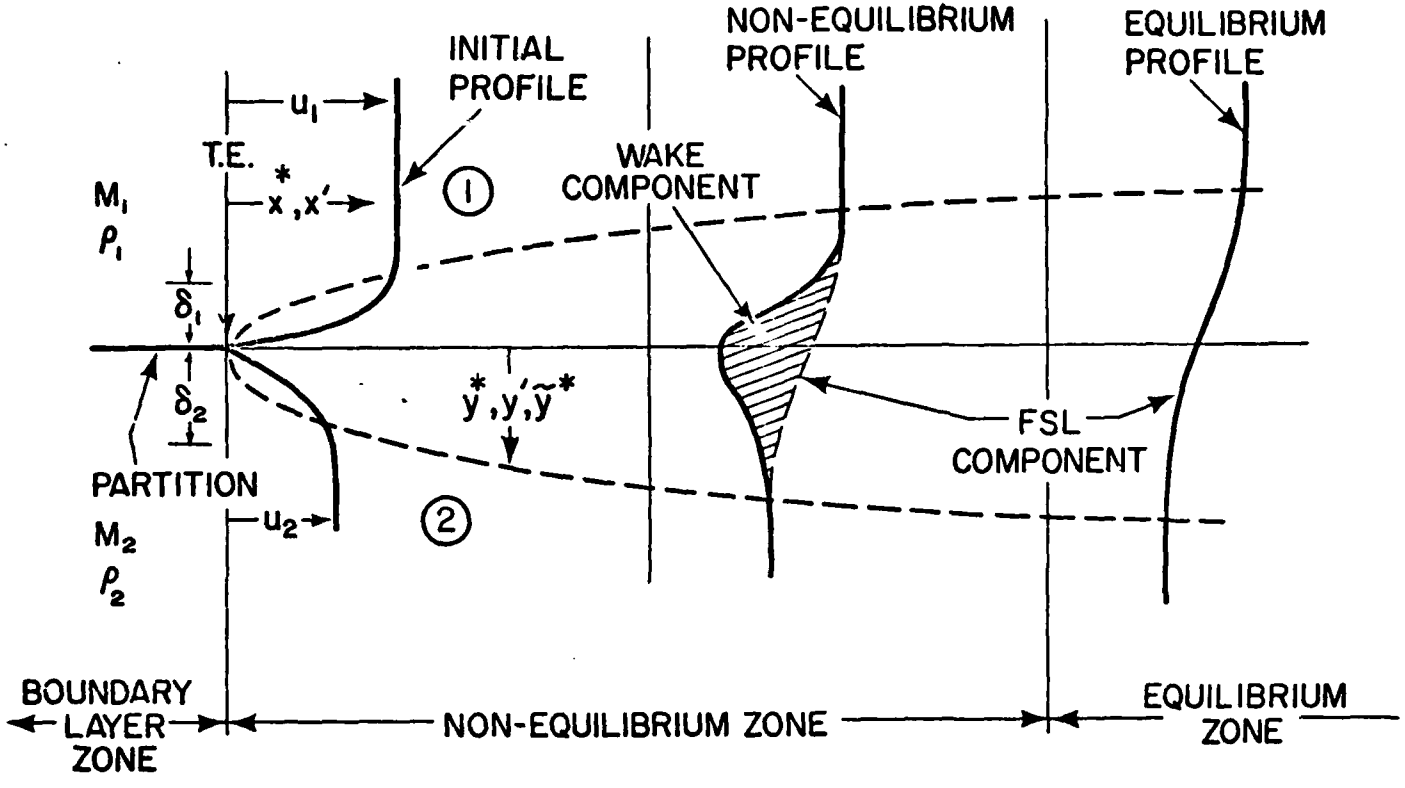


Figure 1. Nomenclature and Definitions of the FSL Problem

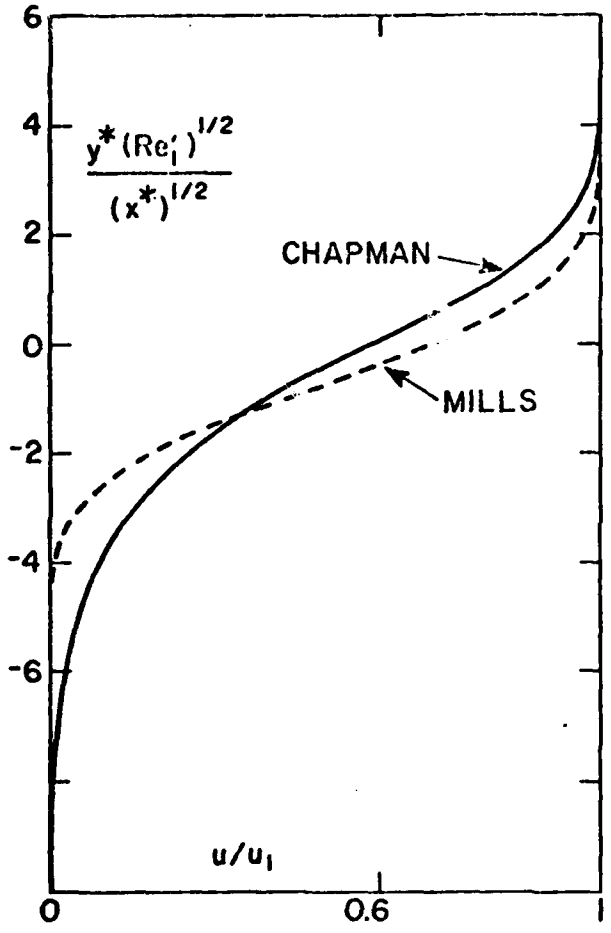


Figure 2. Shear-layer components

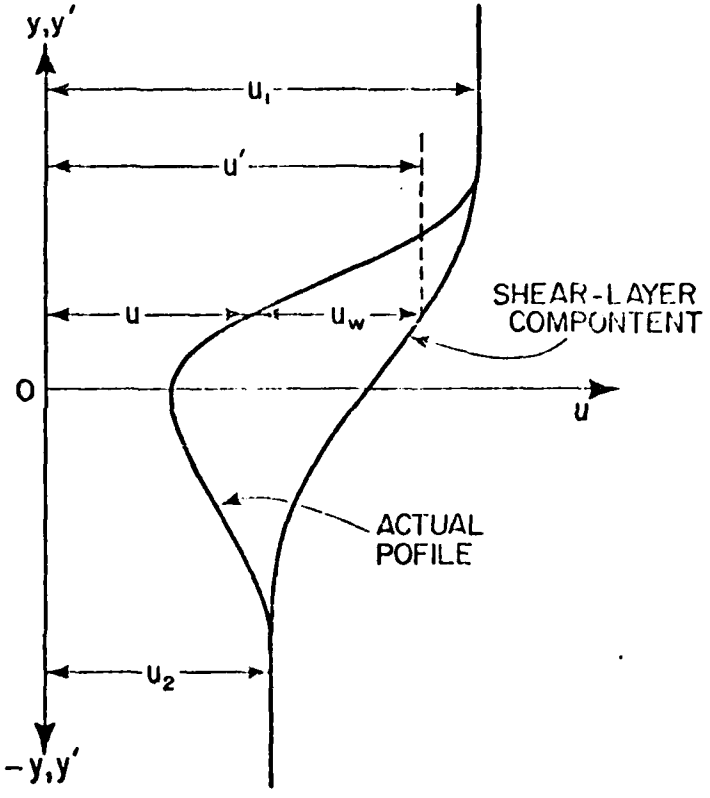


Figure 3. Methods of combining wake and FSL components

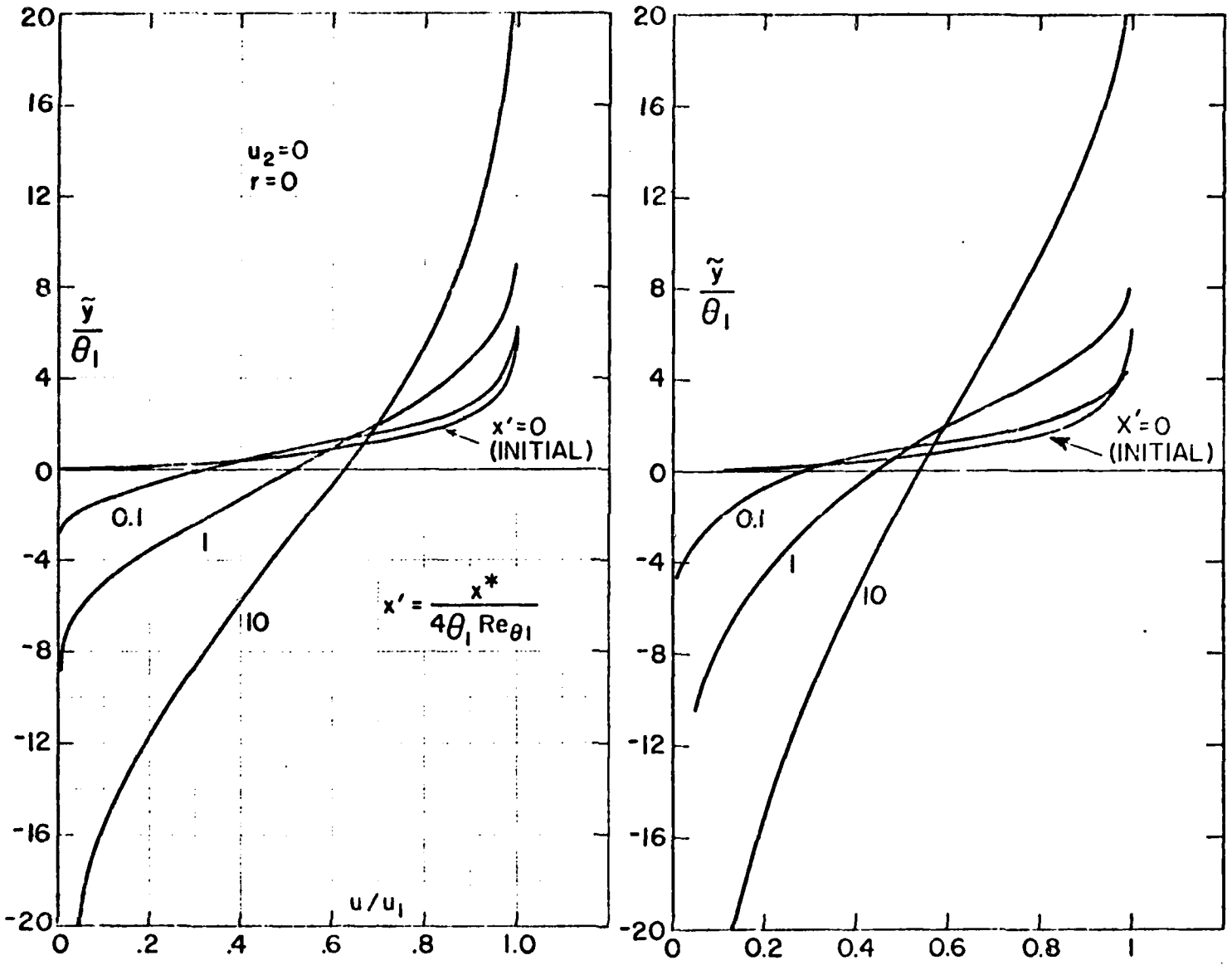


Figure 4. FSL for r = 0 for Mills (left) and Chapman (right) models.

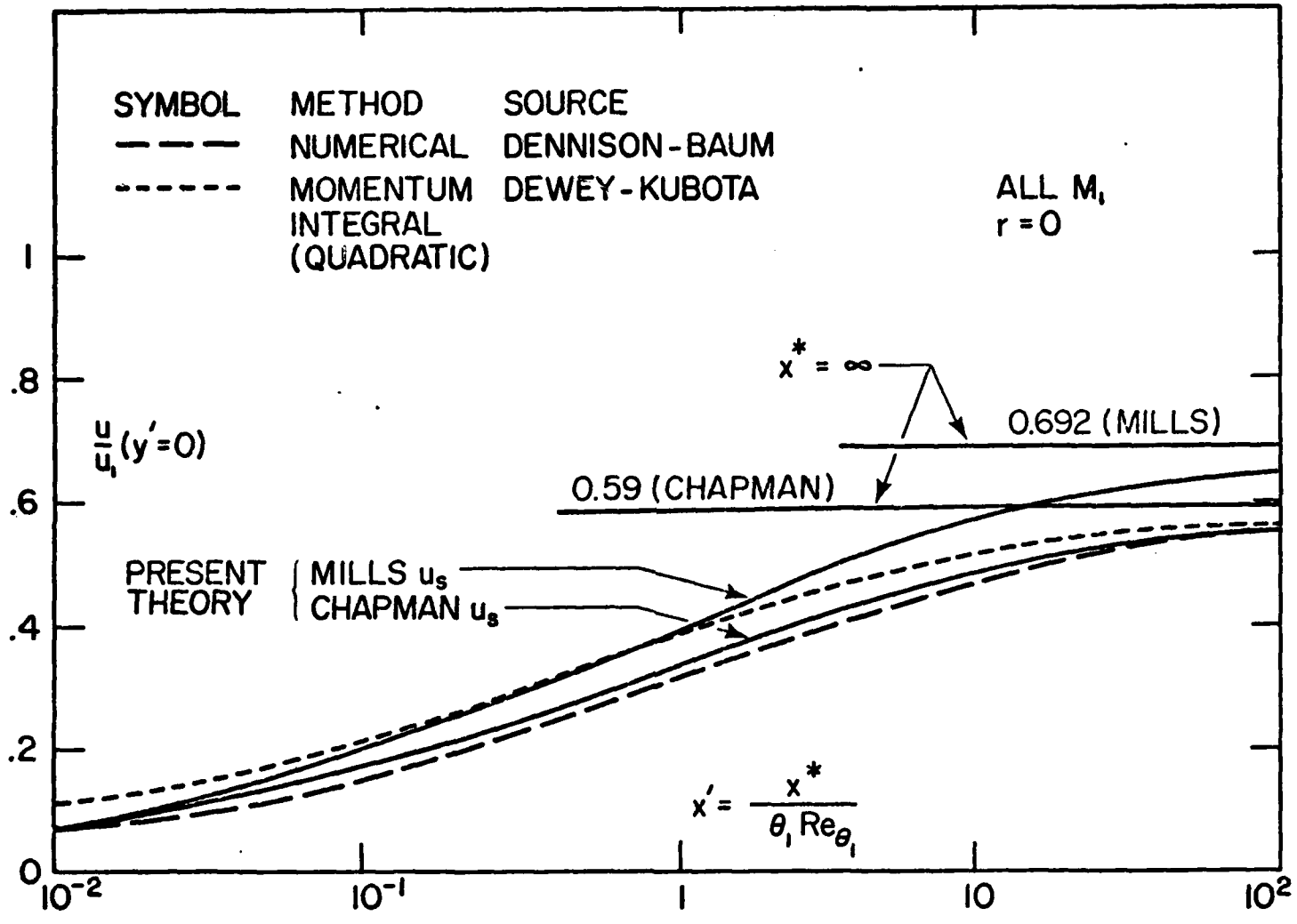


Figure 5. FSL development at y' = 0, for r = 0.

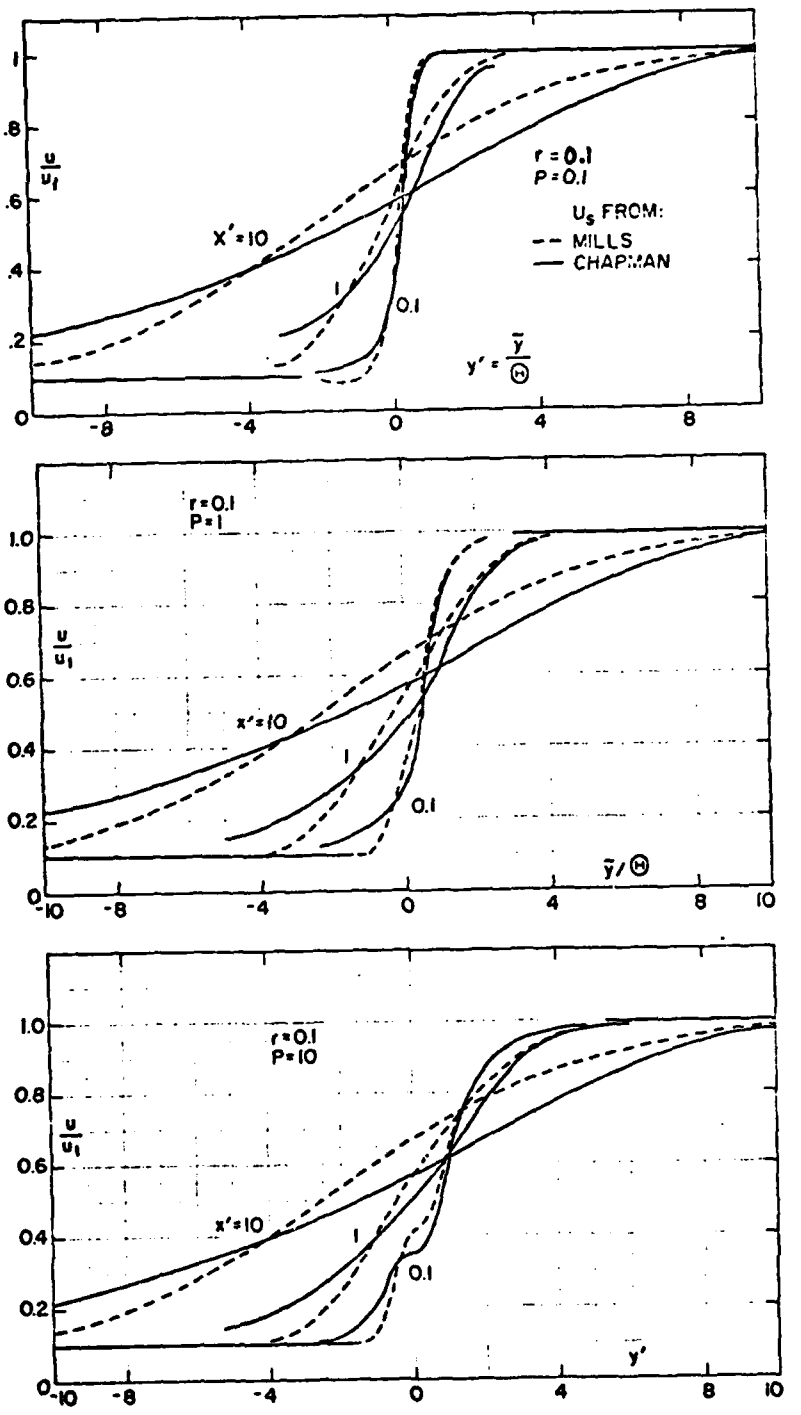


Figure 6. Typical FSL velocity profiles (r = 0.1)

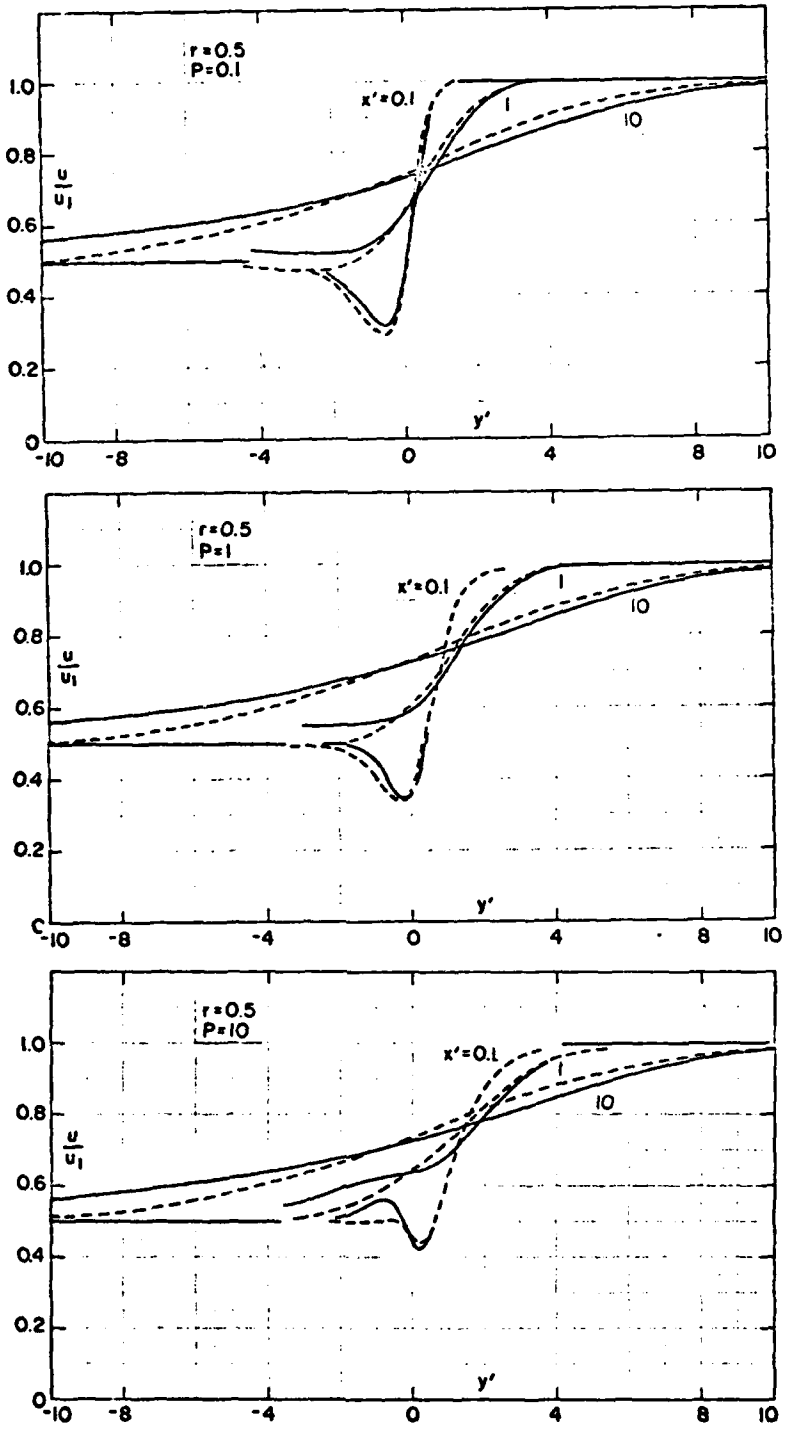


Figure 7. Typical FSL velocity profiles (r = 0.5)

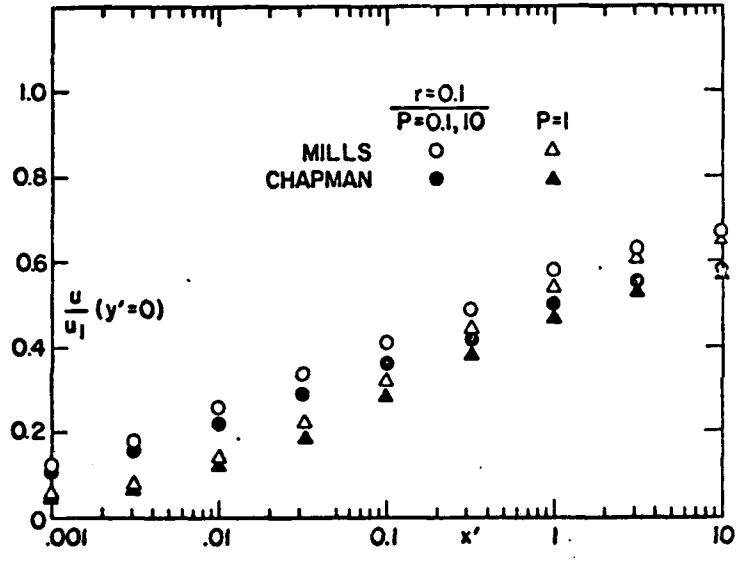


Figure 8. Centerplane velocities, r = 0.1

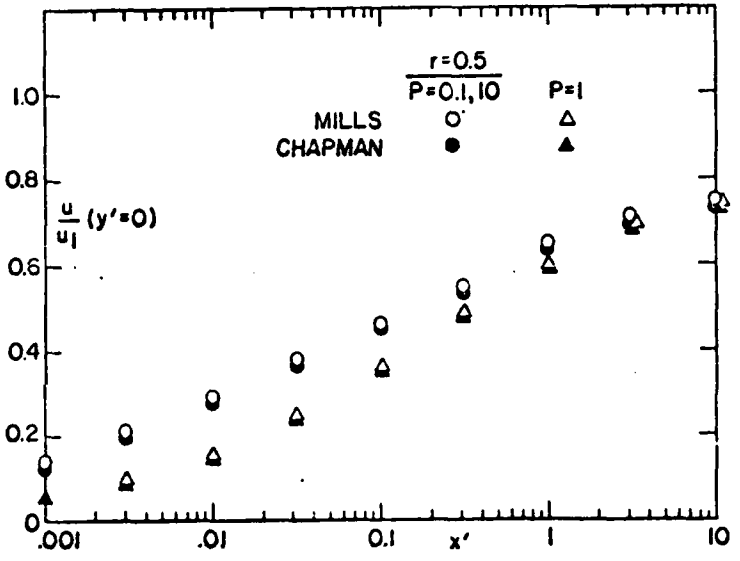


Figure 9. Centerplane velocities, r = 0.5

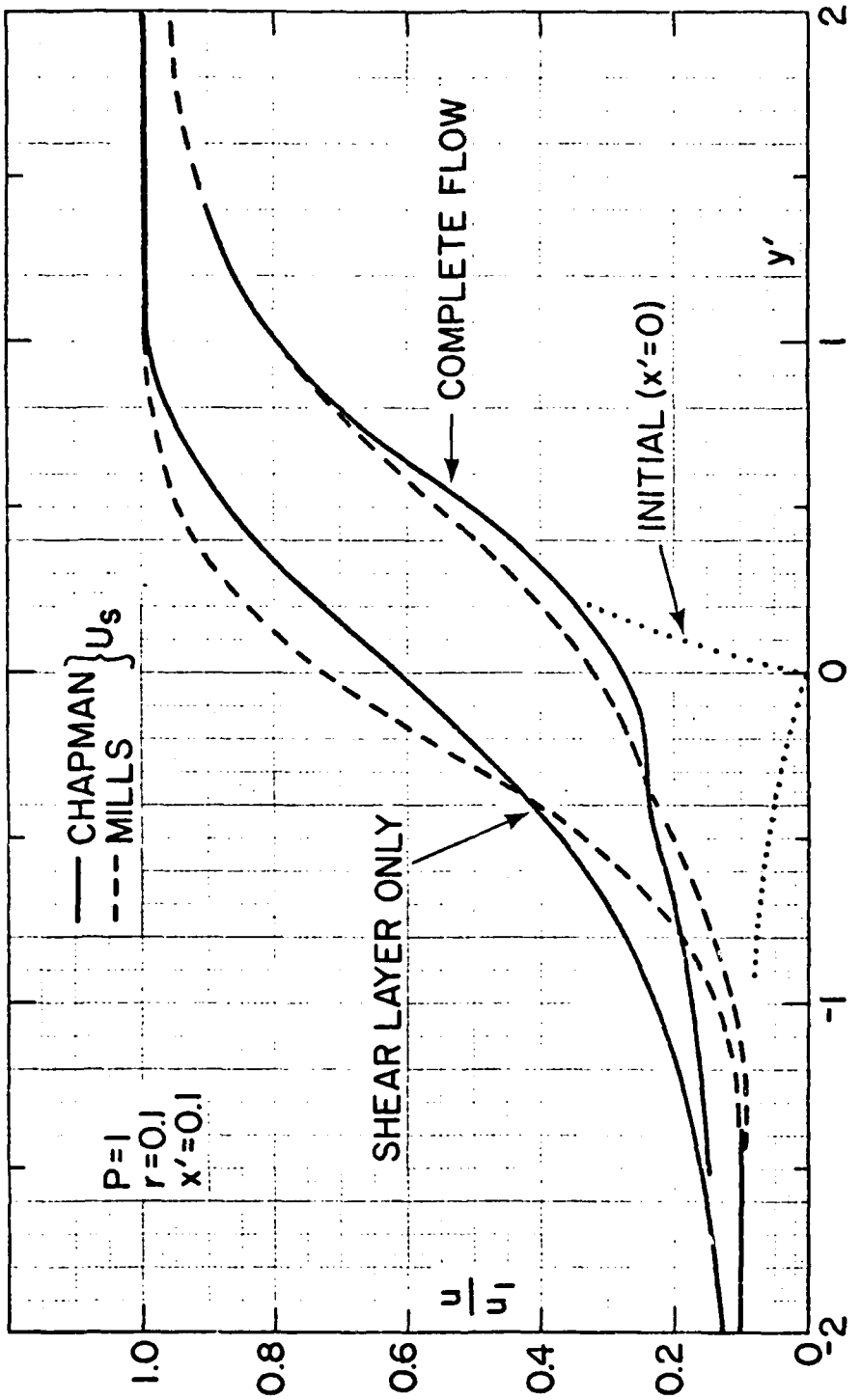


Figure 10. Effect of wake component on FSL flow (typical).